Dissertation

Submitted to the
Combined Faculty of Natural Sciences and Mathematics
Heidelberg University, Germany
for the degree of
Doctor of Natural Sciences (Dr. rer. nat.)

Presented by
Elham Sharifikolouei
born in Tehran, Iran

Oral examination date:
24. January 2018

Fabrication of metal microfibers by melt-spinning

Referees:
Prof. Joachim P. Spatz
Prof. Reiner Dahint

To the greatest discovery during my PhD
Me, falling in love with you, Francesco

Contents

1. Abstract 1

2. Zusammenfassung 3

3. Aim of the project 5
  3.1. Introduction to the thesis 5

I. Melt Spinning 7

4. Introduction to Melt Spinning 9
  4.1. Amorphous metallic alloys 9
  4.2. Mechanical properties of amorphous alloys 13
  4.3. Common rapid quenching techniques 15
    4.3.1. Planar flow melt-spinning 15

5. Materials and Methods 19
  5.1. Melt spinning device and its modification 19
  5.2. Standard experimental procedure 24

6. Experimental Results 25
  6.1. Wheel structure 25
  6.2. Slit size 29
  6.3. Wheel material 33
  6.4. Wheel speed 34
  6.5. Applied pressure 36
  6.6. Ejection temperature 39
  6.7. Slit distance to the wheel 41
  6.8. Chamber pressure 44
  6.9. All parameters 46
  6.10. Fibers reproducibility 48
  6.11. Other materials 49
  6.12. Fiber formation 52

7. Discussion 55
  7.1. Experimental parameters effect 55

7.2. Reproducibility and capability of melt spinning in fiber formation . 64
7.3. High speed camera movie 65
7.4. Possible fiber formation mechanism 66

II. Stainless Steel Microfibers 67

8. Introduction to Stainless Steel 69
8.1. Steel: Fe-C phase diagram 69
8.2. Hardening mechanisms of steels 69
8.2.1. Strain hardening 69
8.2.2. Grain size hardening 70
8.2.3. Precipitation hardening 71
8.3. Steel TTT diagram 71
8.4. Stainless steel 72
8.4.1. Austenitic stainless steel 74

9. Materials and Methods 75
9.1. Fabricating micro-fibers 75
9.2. Heat treatment 76
9.3. XRD and DTA measurements 76
9.4. TEM measurements 76
9.5. Nanoindentation measurements 77

10. Experimental Results 79

11. Discussion 89

III. Vitrovac Microfibers 95

12. Introduction to Vitrovac 97

13. Materials and Methods 99
13.1. Fabricating vitrovac fibers 99
13.2. SQUID and ULF measurements 99

14. Experimental Results 101

15. Discussion 107

16. Final Summary 109

17. Conclusion and Remarks **111**

18. List of Publications **113**

19. Future Work **115**

20. Supplementary Materials **117**
- 20.1. Melt-spinning parameters of all experiments 117
- 20.2. Stainless steel alloy compositions 122
- 20.3. Stainless steel fibers XRD 122
- 20.4. Mechanical properties of different fibers 124
- 20.5. Bulk metallic glasses mechanical properties 125

21. Acknowledgment **127**

22. Declaration **131**

Acronyms

AR	Aspect Ratio
BMG	Bulk Metallic Glass
CBMS	Chill Block Melt Spinning
CCT	Continuous Cooling Transformation
DSC	Differential Scanning Colorimetry
DTA	Differential Thermal Analysis
FIB	Focused Ion Beam
GFA	Glass Forming Ability
GIS	Gas Injection System
ICP-OES	Inductively Coupled Plasma Optical Emission Spectrometry
MFA	Mass Flow per Area
OM	Optical Microscope
PFMS	Planar Flow Melt Spinning
SEM	Scanning Electron Microscopy
SQUID	Superconducting Quantum Interference Device
SS	Stainless Steel
STZ	Shear Transformation Zone
TEM	Transmission Electron Microscopy
TTT	Time Temperature Transformation
ULF	Ultra Low Field
XRD	X-Ray Diffraction

1. Abstract

Metal microfibers have a wide range of industrial applications, e.g. as filters, fiber reinforced composites, electrodes, catalysts, sensors, or magnetic shielding materials. In this project, we modified melt-spinning device and its experimental parameters to fabricate metal microfibers. It was shown for the first time that metal microfibers down to 5 μm could be fabricated using melt spinning device. The size and circularity of formed fibers could be controlled by experimental parameters.e.g. slit distance to the wheel, chamber pressure, slit size, wheel speed. The mechanism of fiber formation relies on two main steps; i)thin film formation on the rotating wheel ii)spontaneous breaking of the film to smaller widths, dewetting the wheel. It was shown that this process is reproducible and could be used for different classes of materials. e.g. intermetallic alloys, conventional alloys, metal elements and amorphous alloys.

The modification of melt spinning device lead to higher quenching rates up to 10^8°C/s. The high quenching rate made it possible to make fully amorphous stainless steel fibers for the very first time. Heat-treatment of amorphous stainless steel lead to dual phase microstructure (nanocrystals embedded together with a glassy phase) which was responsible for its ultra high hardness value, 14GPa. This value is 7 times higher than the original stainless steel hardness. Thus, the technique opens new possibilities for working with conventional and amorphous alloys e.g. mechanically improved conventional alloy microfibers/ribbons, introducing new alloy microstructures.

2. Zusammenfassung

Metallmikrofasern haben ein großes Anwendungsspektrum in der Industrie, sie können zum Beispiel als Filter, faserverstärkte Verbundstoffe, Elektroden, Katalysatoren, Sensoren oder als Material für magnetische Isolierungen eingesetzt werden. In diesem Projekt haben wir eine schmelz-spinn Einheit und ihre experimentellen Parameter zur Herstellung von Metallmikrofasern modifiziert. Es konnte zum ersten Mal gezeigt werden, dass durch die schmelz-spinn Einheit Metallmikrofasern bis hin zu einem Durchmesser von 5μm hergestellt werden konnten. Die Größe und Kreisform der produzierten Fasern konnte durch experimentelle Parameter wie dem Schlitzabstand zum Rad, dem Kammerdruck, der Schlitzgröße oder der Radgeschwindigkeit kontrolliert werden. Der Mechanismus zur Faserherstellung beruht auf zwei Hauptschritten: i) Die Formation von dünnen Filmen auf dem rotierenden Rad ii) Das spontane aufbrechen des Films zu kleineren Querschnitten, welche das Rad entnetzt. Es konnte gezeigt werden, dass dieser Prozess reproduzierbar ist und für verschiedenen Materialarten wie intermetallische Legierungen, konventionelle Legierungen, Metallelemente und amorphe Legierungen verwendet werden kann.

Die Modifizierung der schmelz-spinn Einheit führte zu einer höheren Abschreckrate von bis zu 10^8°C/s. Die hohe Abschreckrate machte es zum ersten Mal möglich völlig amorphe nichtrostende Stahlfasern zu produzieren. Die Wärmebehandlung von amorphem nichtrostenden Stahl führte zu einer zweiphasigen Mikrostruktur (Nanokristalle zusammen eingeschlossen mit einer amorphen Phase) welche verantwortlich für die extrem großen Härtegrade von bis zu 14GPa verantwortlich sind. Dieser Wert ist sieben Mal höher als der Wert von originalem nichtrostenden Stahls. Daher eröffnet diese Technik neue Möglichkeiten um mit konventionellen und amorphen Legierungen zu arbeiten z. B. lassen sich dadurch mechanisch verbesserte, konventionelle Legierungsmikrofasern/-bänder herstellen oder neue Legierungsmikrostrukturen einführen.

3. Aim of the project

Metal microfibers have a wide range of industrial applications, e.g. as filters, fiber reinforced composites, electrodes, catalysts, sensors, or magnetic shielding materials. Until now the formation of metal microfibers with a width of less than 10μm from different metal alloys and in large quantity was a challenge or simply not possible. In this project, we examined the possibility of fabricating metal microfibers based on modified melt-spinning device. Besides, melt-spinning is a rapid quenching method that if succeed to fabricate fibers, it is a very fast and robust method and can later lower the time and cost of fiber fabrication significantly in industry. In this project we try to modify the device for fiber formation, and evaluate the possibility using different classes of materials.

3.1. Introduction to the thesis

In this thesis, the first chapter is allocated to the main purpose of the project which is the evaluation of possibility for forming microfibers based on melt-spinning. The mechanical drawing of parts which were modified is presented. Other experimental parameters and their effect on final fiber formation, size and shape are presented and discussed. On the second part of the same chapter, the reproducibility of forming fibers under constant experimental parameters is discussed. Then, the same principle of fiber formation is repeated for different classes of materials to evaluate the capability of the process for different materials. At the very end of this chapter, high-speed camera movies of ejection process are discussed for further understanding of possible fiber formation mechanism by melt-spinning.

The second chapter is specifically allocated to the materials characterization of 316-Ti stainless steel fibers fabricated by melt-spinning. The reason one chapter is completely allocated to stainless steel fibers is their phenomenal mechanical properties after quenching and subsequent heat-treatment. It is also because this grade of stainless steel, for the first time, could form a complete amorphous structure without any addition of refractory materials. Its microstructure and properties are investigated by SEM,XRD,DTA and TEM. Its mechanical properties is evaluated using nanoindentation.

Last chapter is a small project allocated on characterization of Vitrovac 6025X, a type of soft ferromagnetic amorphous alloy purchased from vacuumschmeltz GmbH in forms of ribbon and later casted in forms of fiber by melt-spinning. Its hysteresis was measured using SQUID and ULF. Its mechanical properties such as hardness and elastic modulus was measured using nanoindentation. The purpose of this chapter is to show some properties of amorphous alloy microfibers fabricated by melt-spinning which can have later applications in industry.

Part I.

Melt Spinning

4. Introduction to Melt Spinning

4.1. Amorphous metallic alloys

Amorphous metallic alloys are metal or alloys with no long-range atomic order. They are also known as glassy metals. Similar to glasses, they undergo very rapid solidifications, which prohibit them from forming any long-range order or the so called crystalline structures. However, there are clear short-range orders seen in their structure indicating their properties with their nearest neighbors[1]. In fact, the glass structure can be considered as an approximation to an assembly of dense randomly packed spheres of two or more different diameters. Thus, in this densely packed structure, one would expect to have significant degree of short-range ordering[2]. There are some main categories of amorphous alloys which includes: the transition metals and metalloid (TM-M), the rare-earth transition metals and transition metals (RE-TM), and transition metals with Hf or Zr (TM-Hf, TM-Zr). Studying characteristic of each group is beyond the scope of this thesis, however.

A non-crystalline solid phase represents the ultimate solid metastable phase and it can be formed by different approaches including solidification from liquid or vapor phases, chemical solution deposition, or high energy particles such as neutron (or ion) bombardment of crystalline material. To be able to prevent crystalline phase formation, the liquid must be cooled fast enough to suppress crystallization. Glass formation occurs easily in some materials such as silica and organic polymers. They can be cooled at cooling rates as slow as 10^2 °C/s and still form glasses. However, based on the nature of metallic bond and their non-directionality, metallic melts can rapidly obtain their atomic rearrangements and hence, a minimum critical cooling rate of 10^5 °C/s is necessary to prevent crystal formation.

Besides of rate of cooling, there is another essential factor, which is the degree of undercooling they must go through[3]. This undercooling degree itself depends on the number of other parameters including initial viscosity of liquid, temperature dependency of viscosity (how fast it changes based on temperature reduction), the free energy difference between the undercooled liquid and the crystalline phase (the larger this energy, the larger the driving force for crystallization), the interfacial energy between liquid and crystal phase (which is against nucleation), the volume density and several other factors. The growth rate of crystals is very fast in metals and hence, the nucleation must be prevented in the first stage[4]. Normally, the free energy difference between undercooled liquid metal and its equilibrium solid form is big, so thermodynamically, there is a large driving force for nucleation formation and the larger the undercooling, the bigger this driving force. However, in undercooling conditions, the mobility of atoms is decreased and thus the nucleation rate decreases; so basically it is thermodynamically prone to nucleation and kinetically suppressed. This will eventually makes the liquid to get frozen at “glass transition temperature” T_g. This structural freezing to the glass state is, by convention, considered to occur when viscosity is about 10^{13} poise. However, this glass transition temperature as well as the glass structure itself, in practice, depends also on the cooling rate. This is why the structural relaxation during annealing of glasses depends on cooling rate. At T_g, the temperature dependence of the volume and of the enthalpy decrease discontinuously, the sudden decrease of specific heat C_p comes from its fewer degrees of freedom in the frozen structure. On the free volume model of atomic transport, the glass transition corresponds to the elimination of most of the free volume[5, 6, 7].

Based on kinetic studies, any metallic alloy containing a solute even at some atomic percent can form glassy structure if cooled at sufficiently high quenching rates to prohibit spontaneous crystallization. However, the situation for pure metals is less clear. Several studies have been made of thin films produced by condensation from the vapor phase at very low temperatures. This method has much higher effective quench rate 10^{13} K/s than other techniques since deposition occurs atom by atom and the heat of condensation is rapidly removed through the thin film. This is how some amorphous thin film of transition metals were produced based on vapor deposition [8, 9]. By adding solute atoms to pure metals, specially if they have different size and chemical properties from the host atoms, the diffusive rearrangement which melt has to undergo for crystallization becomes harder. Thus, they stabilize glass formation. As the solute concentration increases, T_g increases. On the other hand, during alloying, the liquidus temperature often decreases. Consequently, the interval between liquidus temperature (T_l) and glass transition temperature decreases. In this situation, the Glass Forming ability (GFA) increases. Subsequently, alloys with the highest GFA are those which have deep eutectics or a steep decrease of T_l by increasing solute percentage or when this T_l is small comparing to T_m of the host metal. The ratio of T_g/T_l (T_{rg})is referred as reduced glass temperature and has strong correlation with GFA[10, 11]. Some however use T_g/T_m as reduced glass temperature; Z.P.Lu et al showed that it is T_g/T_l that affects GFA and not T_g/T_m [12]. The highest known T_{rg} are in the range of 0.66 to 0.69 [13, 14, 15]

The critical thickness which material can form the glass is normally between 10μm to 20μm. The smaller is this critical thickness, the wider the GFA. For the critical thickness of this range, usually the cooling rate of 10^6-10^7 °C/s is required for

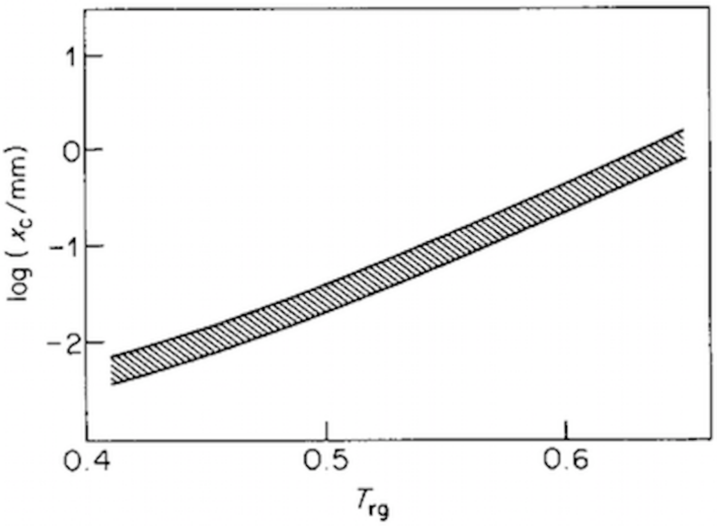

Figure 4.1.: Estimated range of maximum section thickness of glass phase as a function of T_{rg}[15].

most common melt-quenching techniques. T_{rg} in this case will be about 0.45[16]. Figure 4.1 shows the relation between this critical thickness and T_{rg}.

As it has been mentioned, GFA has close correlation with T_{rg}; Experiments show that T_g does not vary much by composition. However, it affects T_l and thus, GFA is dominated mainly by T_l. Several methods have been applied to find the correlation between GFA and T_l.

It was already mentioned that to form a glass the cooling rate must be high enough to suppress crystallization. The minimum quenching rate to form glass can be calculated from the alloy TTT diagram using equation 4.1. Figure 4.2 shows the schematic TTT diagram of an alloy, and the T_n and t_n in it.

$$\dot{T}_c \approx \frac{T_l - T_n}{t_n} \tag{4.1}$$

Where T_n and t_n are the temperature and the time of the nose respectively.

Going back to the correlation between the critical cooling rate and T_{rg}, Figure 4.3 shows the experimentally obtained values for T_{rg} and the critical cooling rate of several amorphous alloys. It can be seen that the higher this T_{rg} is, the lower the critical cooling rate has to be.

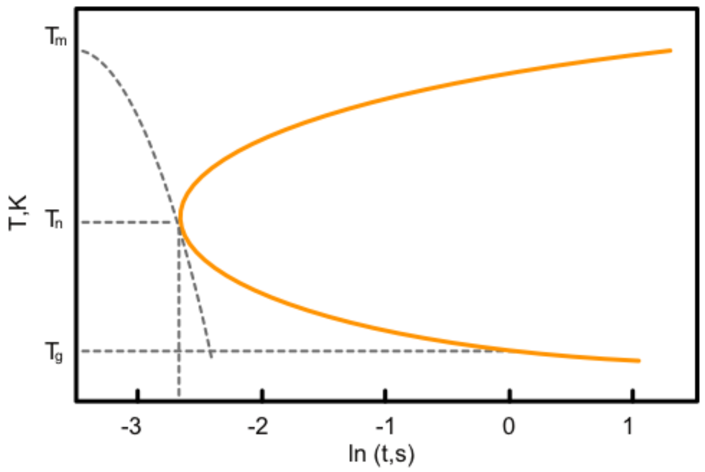

Figure 4.2.: Schematic time-temperature transformation (TTT) diagram of an alloy.

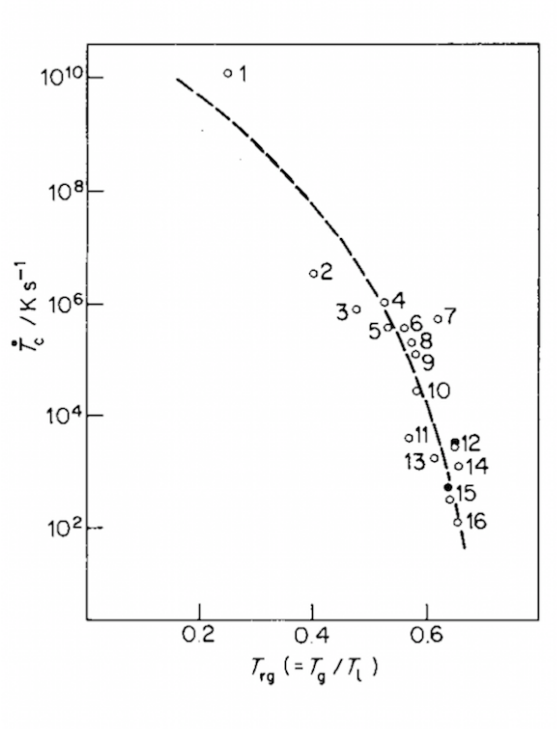

Figure 4.3.: Predicted (empty circle) and experimentally measured (filled circle) critical cooling rate for glass formation $\dot{T}_c$ (based on CCT curves for the formation of a fraction crystal of 10^{-6}) plotted against reduced glass temperature for a representative range of elements and alloys.[15]

4.2. Mechanical properties of amorphous alloys

One of the main attractions of amorphous alloys is their mechanical properties. They show fundamentally different mechanical behavior comparing to conventional alloys. For instance, amorphous alloys often exhibit elastic modulus in the same order of conventional crystalline alloys; however, their room temperature strength is significantly higher than polycrystals with comparable chemical composition[17, 18, 19, 20, 21].

The bonding in amorphous alloys is primarily metallic. Thus, during strain, bonds can readily break and reform in atomic neighborhood without substantial concern, e.g. the charge balance in ionic bonds or rigidity of covalent bond angles. However, amorphous alloys do not have long-range order. In crystalline solids, changes in atomic neighborhood is possible at low energies and stresses because of dislocations. Here, however, any rearrangement in local neighborhood is a high energy or high stress process.

The exact deformation mechanism in amorphous alloys is not very well understood. However, there are some main models describing such deformations. the ones we will shortly describe here are: "bubble raft" model and the classic "free volume" model.

"Bubble raft" model was originally proposed by Argon and Kuo[22]. Figure 4.4 shows the "flow defect" and more commonly called the "shear transformation zone" (STZ)[23]. STZ is a local cluster of atoms undergoing an inelastic shear distortion from one relatively low energy to another such configuration. To go through the second configuration, they need to overcome a high energy and volume activated configuration[22]. It is important to note that STZ is not a structural defect in amorphous metals. It is an event defined in a local volume. Activation of STZ in different local environment (energetically) of course differs from each other and it does depend on the local structure [24, 25]. The energy for STZ is usually in the order of 20-120 $K_B T_g$ [26].

Another popular model for plastic deformation in amorphous alloys is "free volume" model developed by Turnbull et al[27, 28, 29].In this model, deformation is a series of discrete atomic jumps in the glass. These jumps are favorable when they are in the regions of high free volume. The jump has diffusion-like character, so its activation energy is in the same energy order of diffusion: 15-25$K_B T_g$. This activation energy is not far from the lower end of STZ activation energy[27, 30, 31].

What is important regardless of the model describing deformation in amorphous metals whether it is STZ or free volume model, is their comparison with conventional crystalline alloys. In polycrystals, there are different distinct deformation

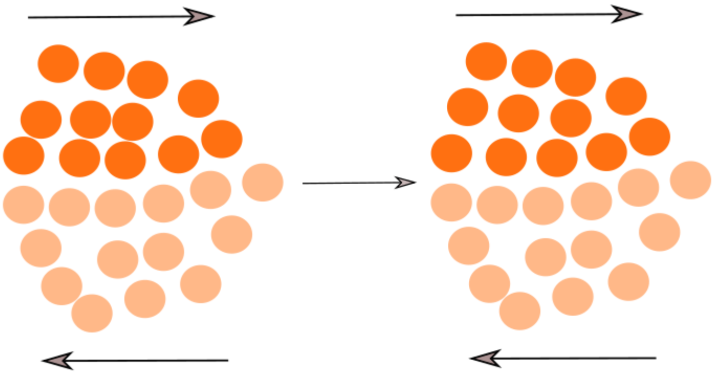

Figure 4.4.: Schematic representation of flow defect or more commonly known as "shear transformation zone" (STZ).

mechanisms with their characteristic energy, size and atomic scale. Consequently, depending on temperature, strain rate, microstructure, etc, one or more of these mechanisms are dominant. In fact the deformation is the competition between different mechanisms. However, in amorphous alloys, STZ and free volume model both describe their deformation with a single mechanism in any condition under complete range of temperatures[32].

Plastic deformation in BMG can be discussed and understood toward their fracture behavior[33, 34, 35, 36]. We previously discussed that the mechanism responsible for deformation in BMG could be understood through STZ or free volume model. However, this does not mean their behavior is constant at different temperatures. At high temperatures (close to T_g), they deform homogeneously with each volume element of the sample. We can consider the deformation similar to viscous flow with low flow resistivity in this situation. The flow itself can be Newtonian, non-Newtonian or even a thermoplastic process[26, 37, 33]. If the temperature is low ($< 0.8T_g$), BMGs show high strength and low plastic elongation. The plastic deformation in this case is inhomogeneous containing localized plastic strains often refereed to as "shear band"[26]. The shear band is often a very narrow region in the scale of 10-20nm. When the shear band forms, it propagates fast and it leads to catastrophic fracture in BMGs[38]. Thus, one needs to understand the formation of shear band and its role in BMGs fracture to be able to control BMGs plastic deformation[33, 34, 35, 36, 39].

4.3. Common rapid quenching techniques

The most frequently used methods for production of thin amorphous metallic alloys are chill block melt-spinning (CBMS)[40, 41, 42], splat quenching[43, 44], and planar flow melt-spinning (PFMS). Here we discus only planar flow melt-spinning.

4.3.1. Planar flow melt-spinning

One of the common techniques for casting amorphous alloys in the shape of thin ribbons is planar flow melt spinning (PFMS). In principle, the metal/alloy is melted by induction and because the distance between the wheel and the slit is small, upon ejection, the melt forms a puddle between the slit and the rotating wheel due to melt high surface tension. The wheel which is often made of a material with high heat conductivity, removes the heat sink from the melt puddle, leading to continuous formation of alloy ribbons. Depending on experimental methods, the shape of this melt-puddle and its size differs and many studies have been done on its modeling[45, 46, 47, 48, 49, 50, 51]. For a fixed slit nozzle geometry, the thickness of the final ribbon depends on several experimental parameters including the wheel speed, the distance between the wheel and slit nozzle, and the applied ejection pressure. In general, one can write for PFMS: $\Delta P/\rho V^2 \approx T/G^2$ [52, 53]. A schematic representation of planar flow melt spinning is shown in Figure 4.5 [54].

The main difference between PFMS and CBMS which was mentioned before is the shape of their orifice and the distance between their orifice (in our work we refer to it as slit nozzle) and the rotating disk (wheel). The shape of the slit nozzle cross-section in this method is rectangular and the distance between wheel and the slit nozzle (G) is in the range of 200 to 400 μm. When slit nozzle is very close to the wheel, the width of casted ribbon will be constant and equal to the length of slit nozzle (S). The thickness of fabricated ribbon can be estimated then, using experimental parameters:

$$t = \frac{1}{S}\frac{Q_f}{V_s} \tag{4.2}$$

Where Q_f is the volumetric melt flow rate and V_s is the wheel velocity. Usually Q_f can be estimated by Bernoulli equation:

$$Q_f = dS\sqrt{\frac{2\Delta P}{\rho_l}} \tag{4.3}$$

Where ρ_l is the liquid density and ΔP is the ejection pressure. Now if we put equation 4.3 in equation 4.2, we will have:

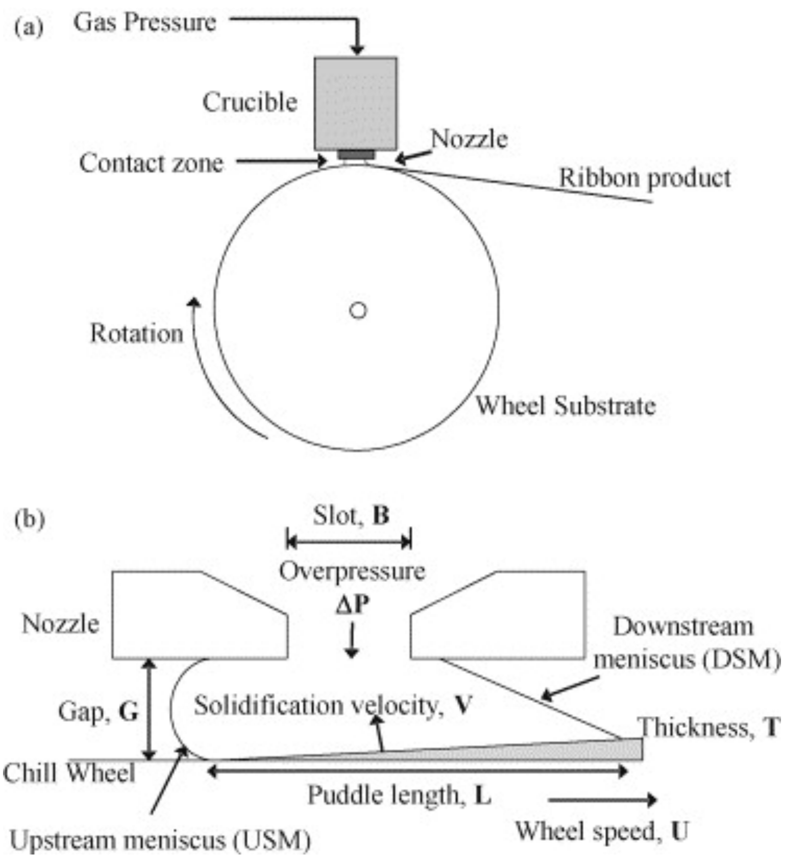
(a)
Gas Pressure
Crucible
Nozzle
Contact zone
Ribbon product
Rotation
Wheel Substrate
(b)
Slot, **B**
Overpressure
ΔP
Nozzle
Downstream
meniscus (DSM)
Gap, **G**
Solidification velocity, **V**
Thickness, **T**
Chill Wheel
Puddle length, **L**
Wheel speed, **U**
Upstream meniscus (USM)

Figure 4.5.: (a) Schematic of melt spinning apparatus and (b) enlarged schematic of the puddle region (not to scale)[54].

$$t = \frac{1}{V_s S} dS \sqrt{\frac{2\Delta P}{\rho_l}} \tag{4.4}$$

However, this equation does not match real experimental data and is often corrected with a correction constant α. In fact, it can show better how experimental parameters and the final thickness of the ribbon are correlated. For a constant material the higher the applied pressure, and the lower the wheel speed, the higher the ribbon thickness[55].

Tkatch et al[56], showed the correlation between the cooling rate and ribbon thickness to be :cooling rate $\propto d^{-3.1}$. Of course, one way to increase the cooling rate is to increase th wheel speed, and this way ribbon thickness can be correlated with the wheel speed. He also showed that both the thickness of melt-spun ribbons and the cooling rates increase with applied ejection pressure at fixed wheel speed and melt temperature.

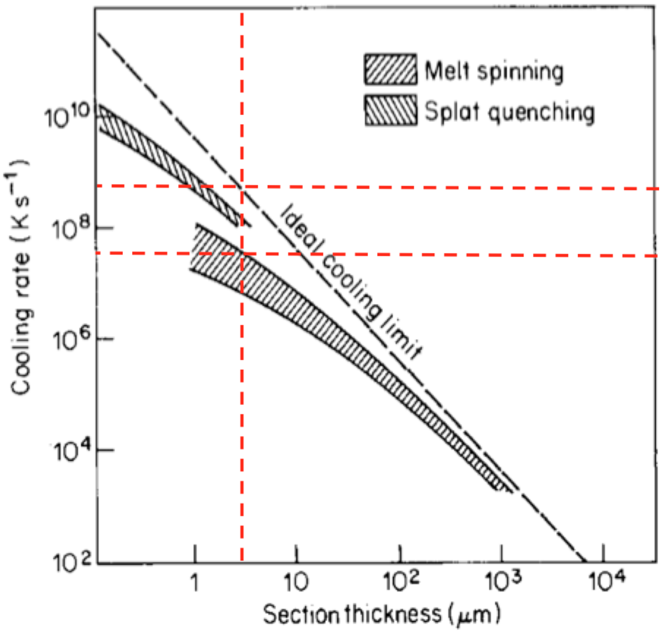

Figure 4.6.: Cooling rate as a function of section thickness for the glass forming alloy $Fe_{40}Ni_{40}P_{14}B_6$ based on experimentally derived values of heat transfer coefficient and ideal cooling for splat quenching and for chill block melt spinning. Unidirectional cooling of a rectangular plate section to one heat sink is assumed in all cases[57].

Figure 4.6 shows the relation between ribbon (section) thickness and the cooling rate for two methods of splat quenching and chill block melt-spinning (which slightly differs from planar flow melt-spinning as mentioned before) computed for the glass forming alloy $Fe_{40}Ni_{40}P_{14}B_6$. Of course, the real cooling rate in these methods slightly differs from an ideal line[57]. This Figure, helps us to make a practical relation between critical cooling rate we need to achieve by melt-spinning for each alloy, based on their glass forming ability (T_{rg}).

5. Materials and Methods

5.1. Melt spinning device and its modification

The Melt Spinner SC purchased from Edmund Buehler GmbH, as it is shown in Figure 5.1 was used for all the experiments in this project. Further development of melt-spinning parts and adjustments were done together with Edmund Buehler GmbH and Max Planck for Intelligent Systems mechanical shop and materials preparation department.

The schematic representation of melt-spinning main parts is shown in Figure 5.2. The main parts include: closed chamber, crucible, slit nozzle, wheel, and induction coil. Of course, each of these parts can introduce certain experimental parameters

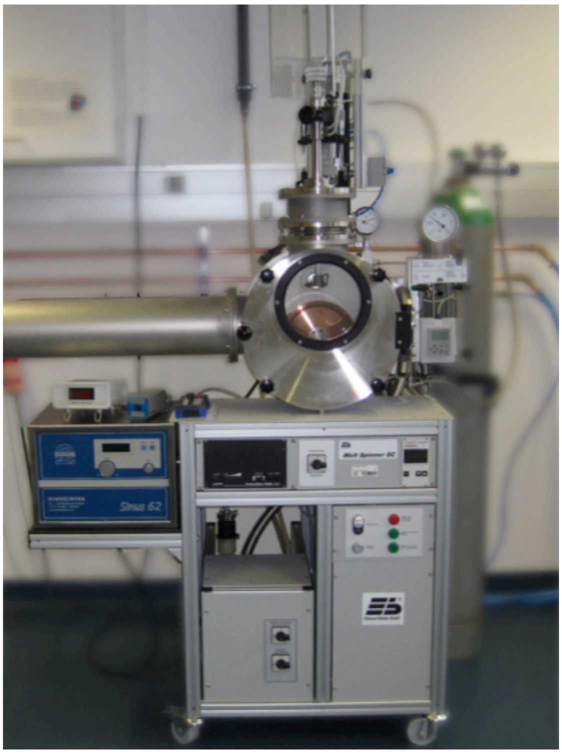

Figure 5.1.: Edmund Buehler (lab-scale) Melt-Spinner SC which was used and further developed in this project.

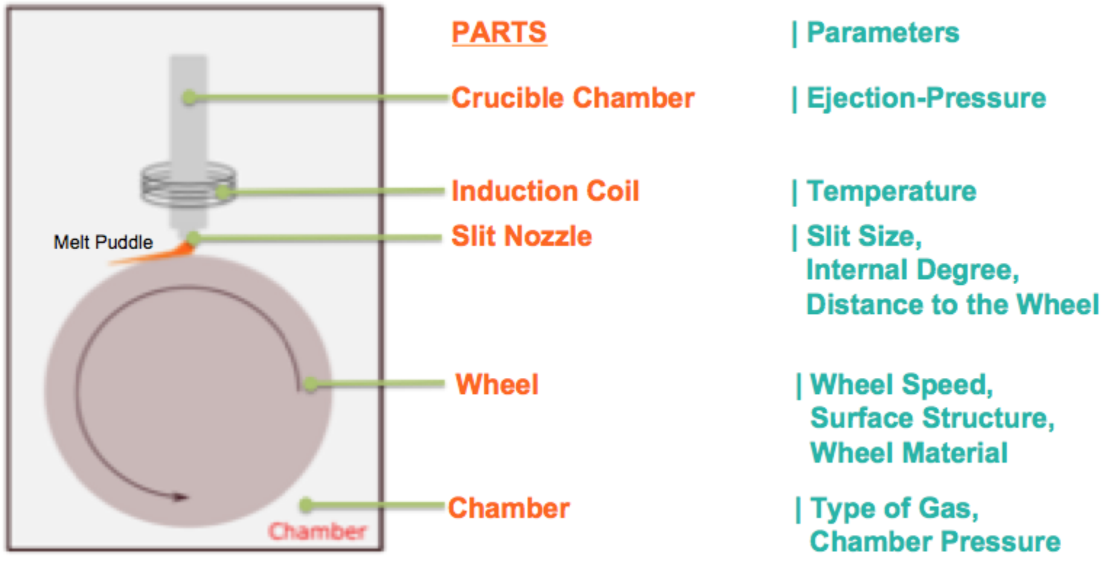
PARTS
| Parameters
Crucible Chamber
| Ejection-Pressure
Induction Coil
| Temperature
Melt Puddle
Slit Nozzle
| Slit Size, Internal Degree, Distance to the Wheel
Wheel
| Wheel Speed, Surface Structure, Wheel Material
Chamber
| Type of Gas, Chamber Pressure
Chamber

Figure 5.2.: Schematic representation of melt-spinner design and its main parts. Each part introduces several experimental parameters that can be changed and modified. Each experimental parameter is state in front corresponding part.

to the system which can be changed and modified each and are introduced in the same Figure 5.2.

Starting from slit nozzle, the slit is made of Boron-Nitride (BN) and is a separate piece from the crucible that can be changed before each experiment. Figure 5.1 shows the 3 main slit designs used during this project. However, the main standard design used in most experiments is shown in Figure 5.3b.

The crucible was also made of BN and thus could be heated safely up to 1500°C. However, in some experiments it was heated up to 1600°C for a short time.

The chamber was always securely closed before each experiment and in standard conditions, it was filled by 400 mbar Argon gas. The type of filling gas was optional and could be changed to any other cooling gas e.g. Helium. Chamber pressure is clearly one parameter that can be changed depending on the purpose of experiment. Before filling the chamber by Ar gas, rotary vacuum pump was used to reach $P < 10^{-5}$mbar. If the sample was sensitive to oxygen, turbo pump was used after rotary pump to reach higher vacuum.

The induction coil was made of copper and its original design and position is shown in Figure 5.4a. Upon developing the device, due to high thermal fluctuations during melt-ejection, its position was changed, and placed closer to the wheel surface; where the sample could be heated while ejecting the melt. In the new

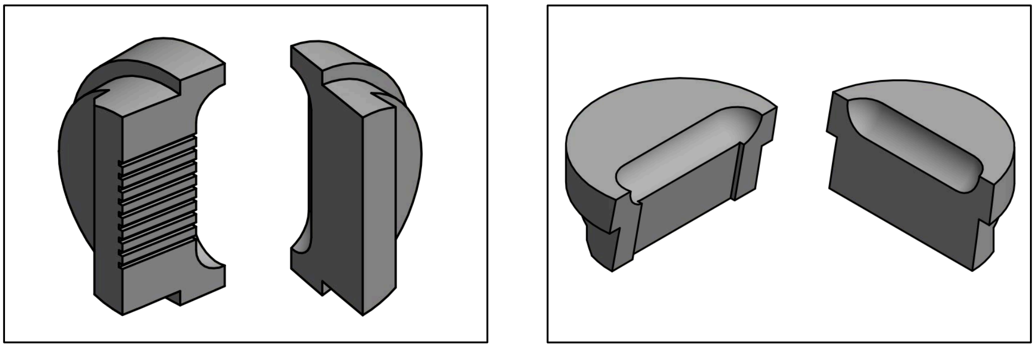

(a) micro-channel slit design

(b) rectangular slit design

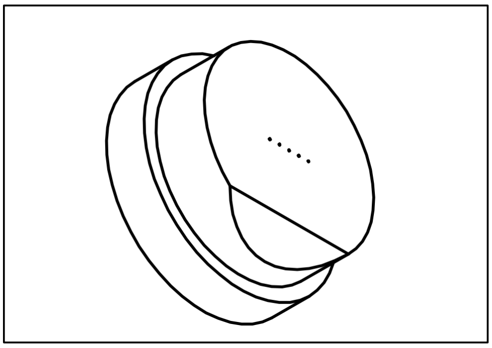

(c) micro-holes slit design

Figure 5.3.: Three main slit nozzle designs used at this work. a)microchannel design. each channel is rectangular b)rectangualr slit design. This is the design used in all standard experiments, otherwise stated. c) micro-holes slit design.

design, the coil was further coated by Alumina to make its surface non-conductive. Flying fabricated fibers upon dewetting the wheel could attach to the coil surface and cause short-circuit. Short circuit was prohibited by the Alumina coating in the new design. Figure 5.4b shows the new position of coated copper coil.

Figure 5.5 shows the difference between temperature stability during melt-ejection at these two coil configurations. At old coil configuration, temperature drops fast during melt-ejection, stopping the whole process while the time of ejection is prolonged at new coil configuration.

The wheel was made of copper, or 0.8%Cr,0.08%Zr,99,12%Cu , or stainless steel. Most experiments were done using copper or 0.8%Cr,0.08%Zr,99,12%Cu flat wheels, otherwise stated. Four different surface structures made of copper wheel was also designed and machined. Mechanical drawing of these structured wheels is shown in Figure 5.6.

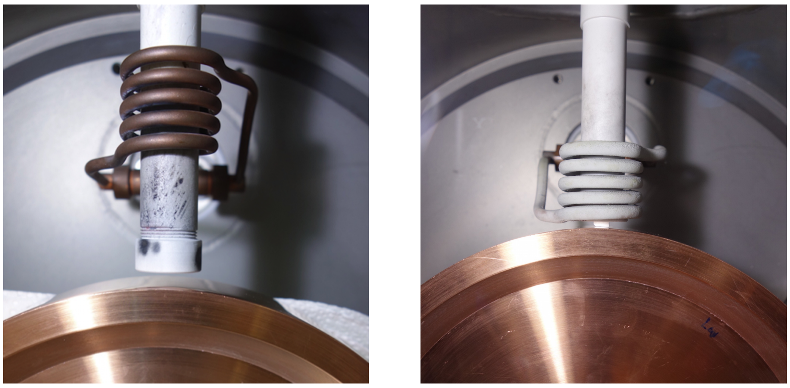

(a) previous coil configuration **(b)** new coil configuration

Figure 5.4.: New vs. previous configuration of copper induction coil.

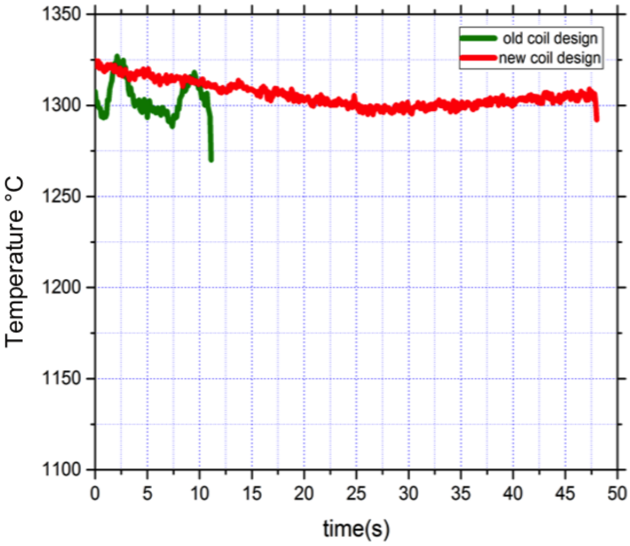

Figure 5.5.: Temperature stability over the time of melt-ejection at two induction coil configurations. Temperature drops fast at previous coil configuration and the ejection stops. This temperature stability is improved at new configuration.

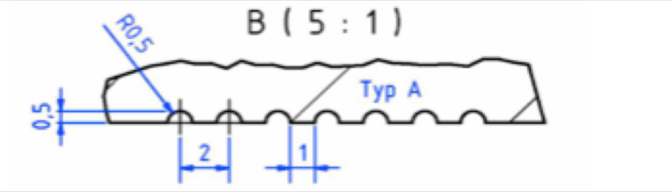 B (5 : 1) R0,5 Typ A 0,5 2 1	**Type A** **Distance bet grooves = 1,0 mm** **Groove width = 1,0 mm** **Groove depth = 0,5 mm**
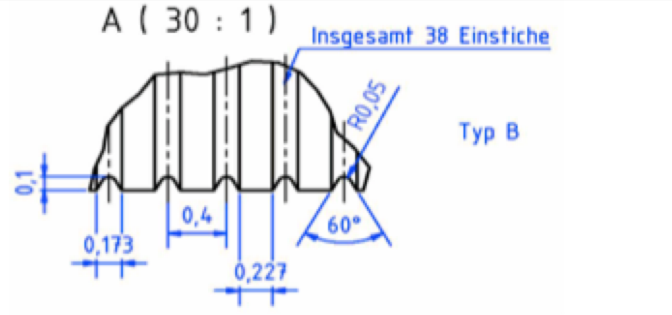 A (30 : 1) Insgesamt 38 Einstiche R0,05 Typ B 0,1 0,4 60° 0,173 0,227	**Type B** **Distance bet grooves = 0,227 mm** **Groove width = 0,173 mm** **Groove depth = 0,100 mm**
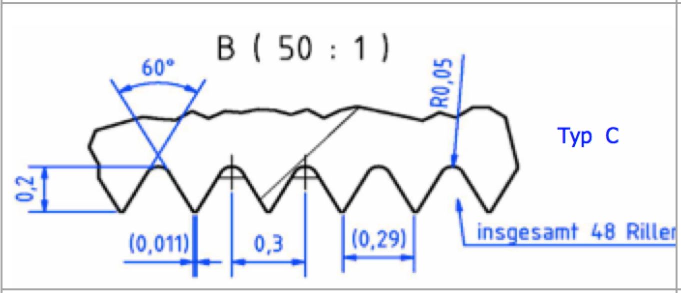 B (50 : 1) 60° R0,05 Typ C 0,2 (0,011) 0,3 (0,29) insgesamt 48 Riller	**Type C** **Distance bet grooves = 0,090 mm** **Groove width = 0,210 mm** **Groove depth = 0,130 mm**
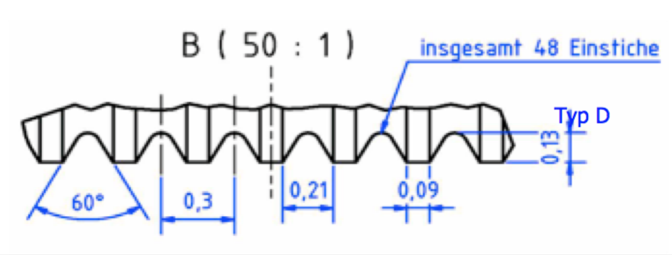 B (50 : 1) insgesamt 48 Einstiche Typ D 0,13 60° 0,3 0,21 0,09	**Type D** **Distance bet grooves = 0,011 mm** **Groove width = 0,290 mm** **Groove depth = 0,200 mm**

Figure 5.6.: Mechanical drawing of groove structures machined on the copper wheel. The size of the grooves and the distance between them is indicated for each structure.

5.2. Standard experimental procedure

The standard procedure for fabricating fibers by melt-spinning device is summarized here. The exact parameters can be changed depending on the material but the standard parameters for fabricating $Fe_{40}Ni_{40}B_{20}$ alloy fibers is given here in Table 5.1.

Figure 5.7 shows the melt-spinning device during fiber formation.

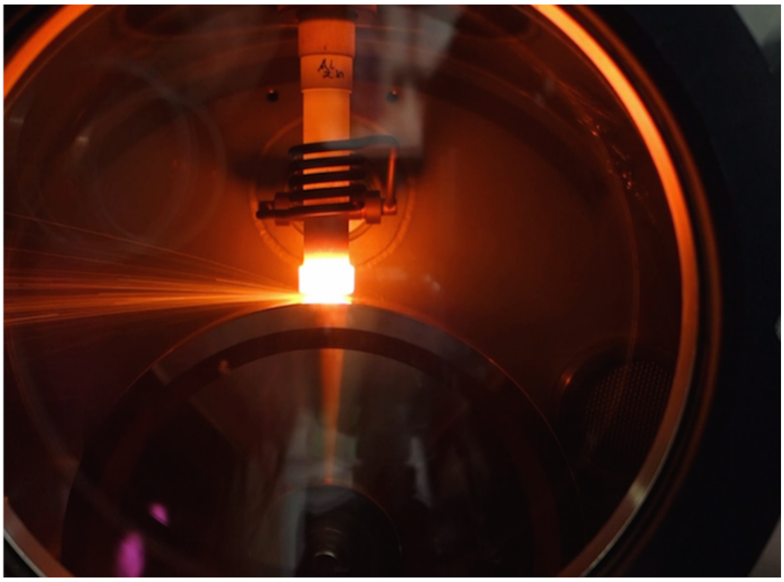

Figure 5.7.: Image taken from melt-spinning device during fiber fabrication.

Table 5.1.: Standard melt-spinning experimental parameters

Wheel type	V	δ	G	P	ΔP	$T_{ejection}$
unit	m/s	μm	μm	mbar	mbar	°C
Flat Cu wheel	60	50	200	400	1000	1350

6. Experimental Results

As it was already explained in the introduction, the main aim of this project is to evaluate the possibility of fabricating fibers based on melt-spinning device. For this purpose its part was modified and its experimental parameters were investigated in this project. In this part, we focus on the effect of modified parts and experimental parameters on the resulting casted material which can be in form of particle, ribbon, or fiber. Casted materials are further analyzed regarding their size distribution and shape. Based on these analysis, we might be able to answer whether or not it is possible to fabricate fibers by melt-spinning. Some of the experimental parameters investigated here include wheel structure, wheel material, wheel speed, slit size, slit distance to the wheel, chamber pressure, ejection pressure, and ejection temperature. It has to be noted that in this part all the experiments are done using $Fe_{40}Ni_{40}B_{20}$ alloy.

6.1. Wheel structure

The basic idea of modifying melt-spinning device for fiber formation started with modification of the wheel surface structure. For this reason, wheels with different surface structures as shown in Figure 5.6 were used. The optical images of casted materials on these structured wheels are shown in Figure 6.1. As a first trial starting from a ribbon-forming device, modification of wheel surface structure seems to be promising for forming fibers. Although one can not judge the homogeneity of produced fibers, but with good approximation they look like fibers. It is also visible that the casted material on wheel type C contain lots of powder and particles as well. If we take a closer look at the produced fibers by SEM, which can be seen in Figure 6.2, we realize that there are some round circular fibers together with some products which look more like a ribbon in the range of micrometer (microribbon). It is also noticeable that most ribbon-shaped fibers contain defects and irregular border on one of their sides. Regarding their size, they appear to be diverse ranging from 5μm up to 150μm.

Since the casted products are not all fully circular, from now on, we will consider them all as microfibers but we measure their deviation from fully circular shape fibers. If we consider a more ellipsoid cross section for these fibers, one can consider a certain width and thickness for their cross section. Figure 6.3 shows the schematic

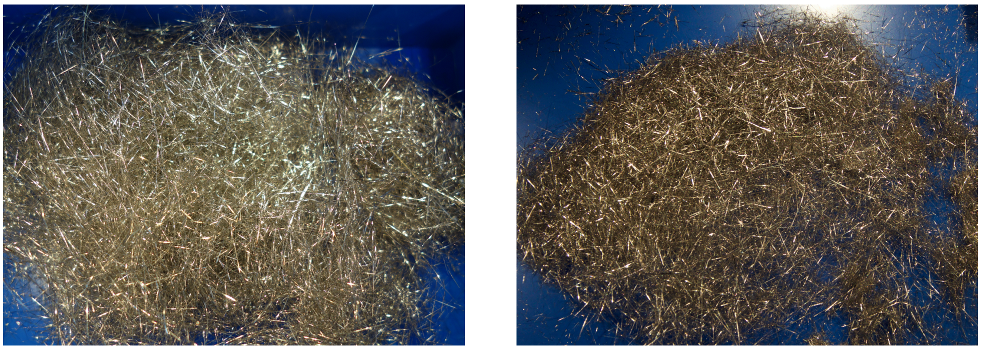

(a) casted material on wheel type A

(b) casted material on wheel type B

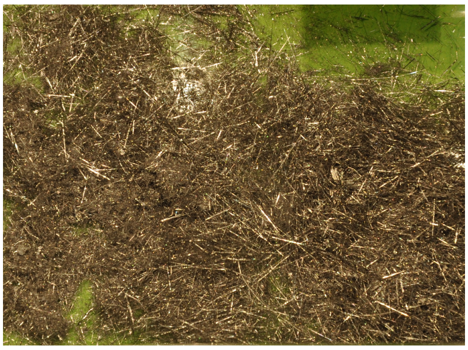

(c) casted material on wheel type C

Figure 6.1.: Optical picture of casted materials on three different wheel surface structures. They all macroscopically could be considered as fibers with a good approximation.

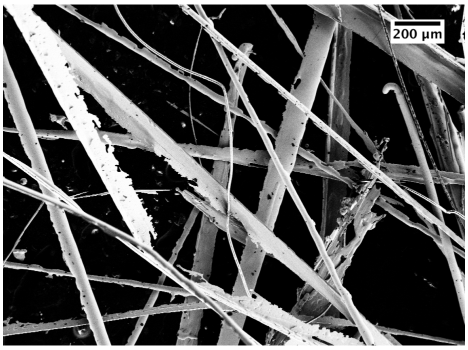

Figure 6.2.: SEM picture of casted material on wheel type C. Some casted materials are circular and have the shape of a fiber while some of them have a shape of ribbon in micrometer range.

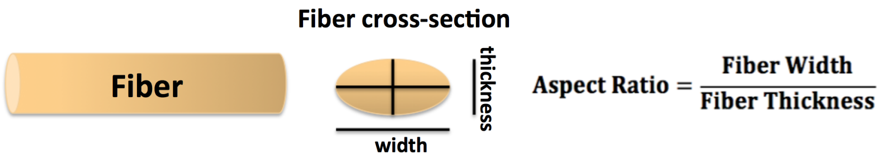

Figure 6.3.: Schematic representation of fibers cross section. The deviation from circularity and fully fiber shape can be evaluated using the aspect ration.

evaluation of fibers cross-section. The aspect ratio of fibers width to thickness can be a measure of circularity. The closer this ratio is to 1, the closer it is to perfect circular fibers.

The mean value of fibers widths is quantified for each fibers casted on different wheel types and is shown in Figure 6.4. This Figure shows more schematically the structure of the wheel surface and where the melt could have formed fibers on it. The blue dots are hypothetical places were the molten metal was solidified on them. In fact, one could expect the production of ribbons with the width comparable to the distance between the grooves on wheel surface or the size of the groove itself. However fibers mean width values does not fulfill this expectation. It is then concluded that certain parts of wheel structure were preferred for the melt to wet and form a film. For wheel type A, the fibers mean width value is almost 28 times less than a distance between the grooves. This value for wheel type B is about 8 times smaller, and for wheel type C the width of fibers is 21 times less than its groove distance. This shows no linearity between the groove distances and the produced fibers width. In fact, the shape of the grooves might have more effect on the final size of fibers widths.

However, the approach toward modifying the wheel surface structure did not go further for the technical problems it caused upon casting, leading to not fully reproducible results. Figure 6.5 shows the surface of the wheel type C after casting

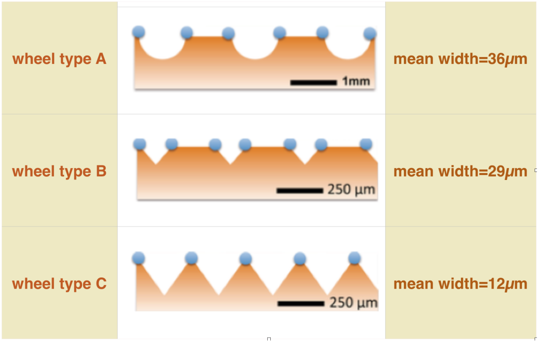

Figure 6.4.: Different wheel surface structures for fabricating fibers. The blue circles are indication of assumed places where the melt wets the wheel.

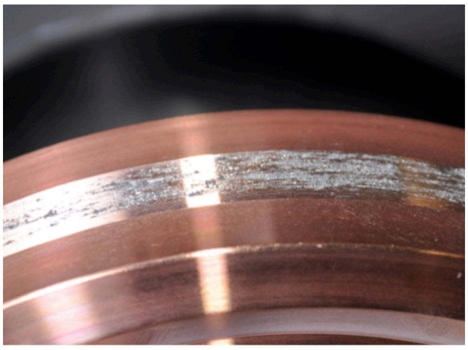

Figure 6.5.: Surface of wheel type C, after fabricating fibers. There is a thick solidified film of molten metal on the surface of the wheel.

material. As it can be seen in this figure, a thick film of solidified alloy remains on the wheel. The thickness of the solidified film is not constant on the wheel, and it varies at different parts of the wheel. Due to spike structure of the grooves, it is not practically possible to remove the solidified film by polishing after each experiment. Therefore, it is not possible to provide the same groove structure for the next experiment.

For the sake of reproducibility, flat wheel was examined to fabricate fibers. The first result based on melt-spinning on the flat wheel is shown in Figure 6.6. This is the first time fibers could be fabricated by melt-spinning. Here, fibers seem to be larger than the fibers casted on the structured wheels, but are promising enough to continue working on it.

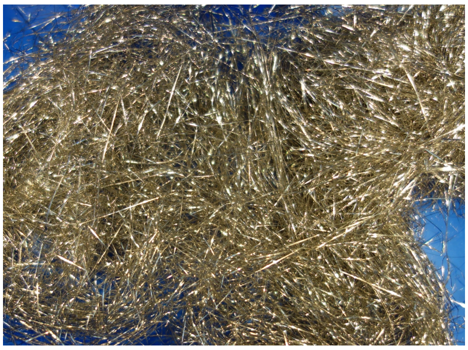

Figure 6.6.: Optical image from fabricated fibers on flat wheel by melt-spinning.

6.2. Slit size

After moving from structured wheel to a simple flat wheel, the focus on modifying the device for fiber fabrication went toward the effect of size of slit opening when the slit has a rectangular opening shown in Figure 5.3b. To evaluate the effect of changing slit size on the final shape and size of casted fibers, different slit sizes of 25μm, 50μm, 75μm, 100μm, 200μm, and 400μm were used.

Figure 6.2 shows the SEM picture of fibers top view and their cross section fabricated by 25μm and 200μm slit sizes. A general look at the SEM pictures, it is evident that the fibers casted by 200μm slit size are larger than the fibers casted by 25μm slit. Besides, fibers have more homogeneous size and shape at smaller slit size. Looking at their cross-section, the shape of the fibers can be compared too. At 25μm slit, the cross-sections are mostly circular or ellipsoid, whereas cross-sections at 200μm slit are almost all rectangular with a width in the range of 150-200μm.

Similar to Figure 6.2, SEM pictures of all fibers cross-sections at different slit sizes were obtained and measured for about 1000 fibers at each slit size and the mean value of their width and thickness is presented in Figure 6.2. The rest of experimental parameters kept constant for these experiments. From Figure 6.2 it is clear that there is a proportionality between fibers mean width/thickness value with their slit sizes. By increasing the slit size, fibers width and thickness mean values increases. If we assume a linear relation between the width/thickness and the slit size, the slope of this line for width-slit size is almost 8.5 larger than its slope for thickness-slit size graph.

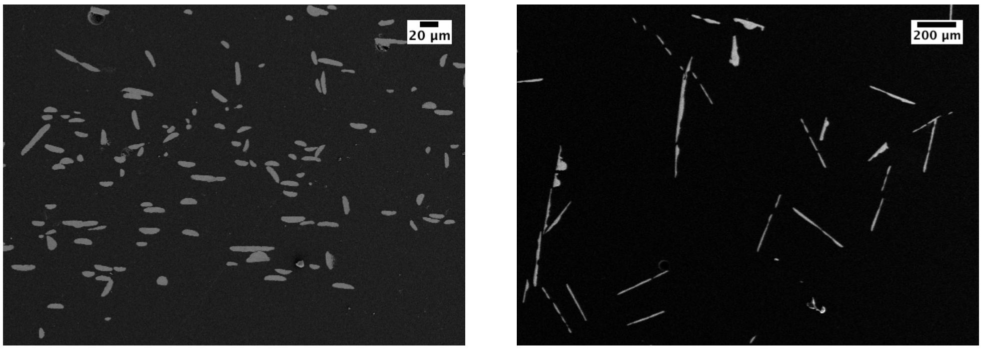

(a) cross-section view of fabricated fibers on 25μm slit size

(b) cross-section view of fabricated fibers on 200μm slit size

Figure 6.7.: SEM picture from fibers cross-sections fabricated by melt-spinning at 25μm and 200μm slit sizes. The cross-section is more circular at smaller slit size and is more rectangular at bigger slit size.

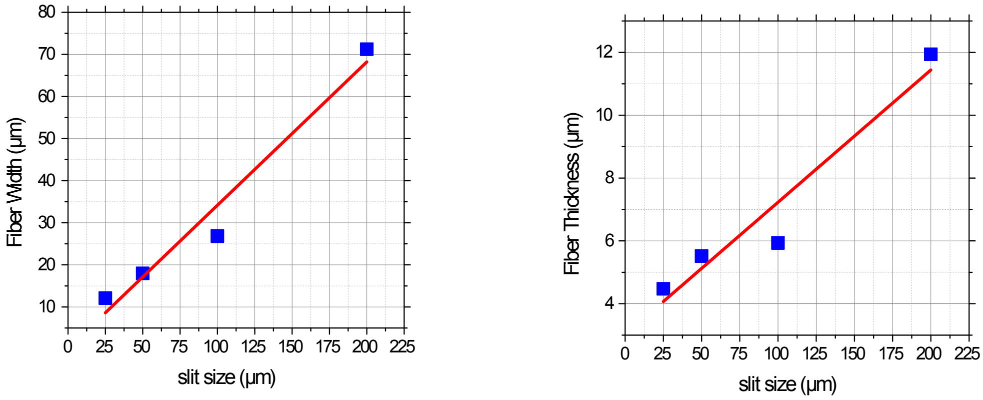

(a) correlation between fibers width and the slit size

(b) correlation between fibers thickness and the slit size

Figure 6.8.: Relation between the slit size and the width and thickness of fibers. It has linear relation with both of them. The slope of this linear relation is 8.5 times larger for width of fibers than their thickness.

Now that we observed the dependency of fibers width on slit size, their ratio is presented in Figure 6.9. The only new information from this graph is that fibers width fabricated at any slit size is always in the range of ≈ 5 to 6 times smaller than the slit size.

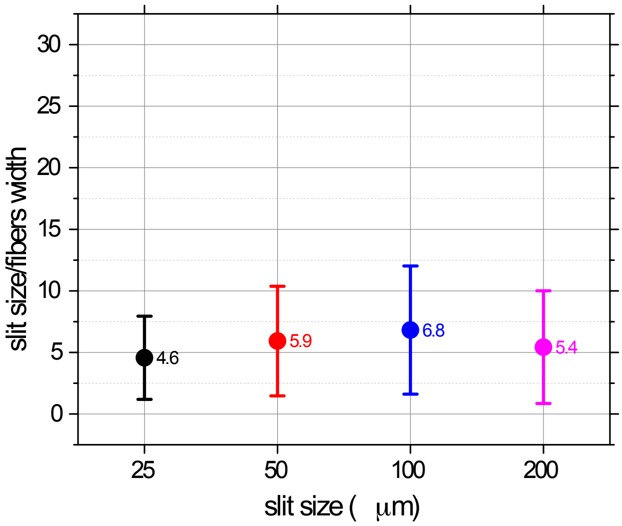

Figure 6.9.: The ratio of slit size over width of fibers at different slit sizes.

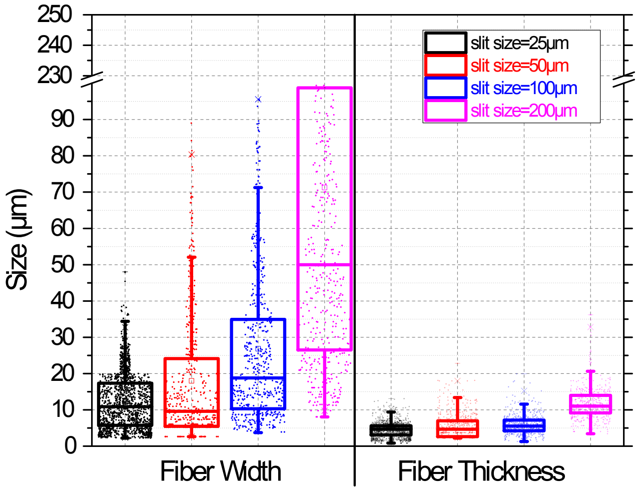

Figure 6.10.: Effect of slit size on size distribution of fibers width and thickness. The larger the slit size, the bigger the mean width value, and broader the size distribution. The fibers final thickness does not get affected significantly by slit size.

To analyze the size distribution of fibers width and thickness, their boxchart is presented in Figure 6.10 for each slit size. We have already observed in Figure 6.2 that the fibers width and thickness increases by increasing slit size. However, this figure gives us more details about how their sizes are distributed. Clearly, fibers width at 25μm slit have the most narrow size distribution. Moving toward larger slit sizes, this size distribution becomes broader. Size distribution of fibers thickness however, does not appear to be affected much by slit size. The only visible change is the shift of their mean value to larger numbers.

Figure 6.11 shows the cumulative counting of fiber sizes (width and thickness) with the bin size of 5μm. It shows the saturation behavior of sizes when fibers are fabricated by different slit sizes, and how their behavior could deviate from each other. It can be seen that fibers fabricated with slit sizes up to 100μm, their thickness values all get saturated around 17μm. However, fibers thickness fabricated by 200μm get saturated around 29μm. So, the thickness values at 200μm slit size deviates from the thickness values of smaller slit size and their curves. Similarly, looking at the width curves in this figure, we see that depending on the slit size, the size saturation behavior differs a lot for each slit size. The 25μm slit saturates at around 35μm width while 50 and 100μm slit sizes have the saturation value of about 100μm width.

So far, we evaluated the size of fibers and their distribution when fabricated by different slit sizes. To evaluate their shape quantitatively, aspect ratio of fibers

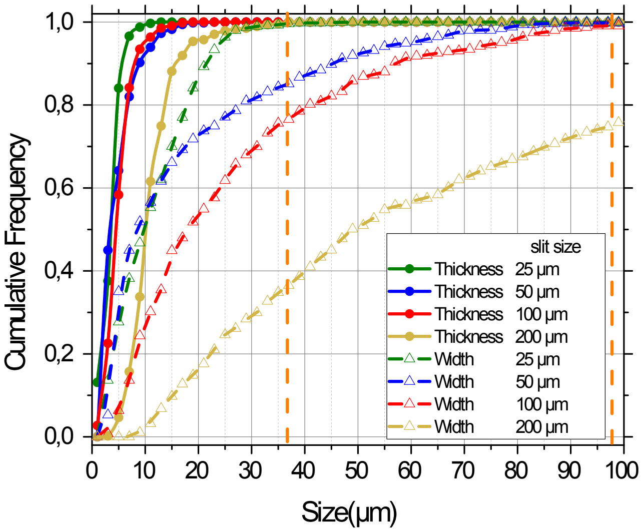

Figure 6.11.: Effect of slit size on cumulative counting of fibers width and thickness size. At different slit sizes, most fiber thickness values get saturated around 17μm , while this saturation value in case of width differs a lot depending on the slit size.

width to thickness in their cross-section was measured. Since this aspect ratio is a tool to see the deviation from perfect circular fibers, the closer this number is to 1 the more circular it is. Figure 6.12 shows the accumulative counting of fibers aspect ratios fabricated by different slit sizes. Each color block shows the percentage of fibers with that specific aspect ratio. Fibers with aspect ratio higher than 4 are all presented in purple color. According to this graph, more than 50% of the fibers have AR<2 using a 25μm slit size. The percentage of fibers with AR<2 decreases by increasing the slit size. Reaching 200μm slit size, less than 15% of fibers have AR<2. This was observed before, in their cross-section SEM picture in Figure 6.7b.

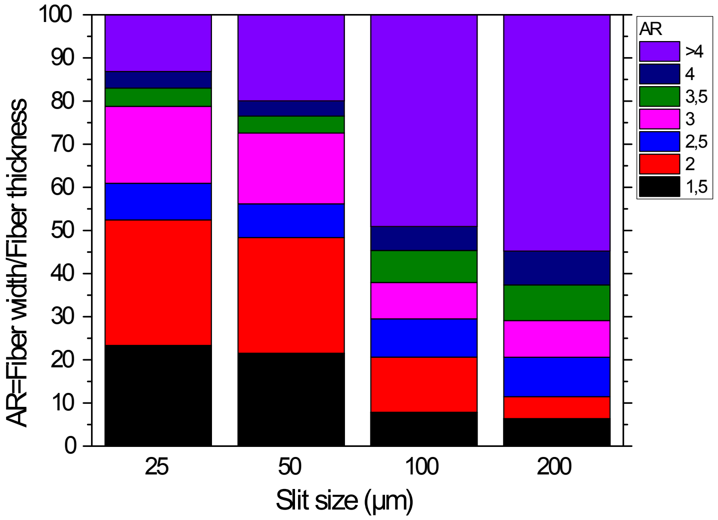

Figure 6.12.: Effect of slit size on aspect ratios of produced fibers. Fibers with AR<2 has the highest percent in 25μm slit size.

6.3. Wheel material

Up to now, we explored the possibility of using different wheel surface structures and slit sizes to fabricate fibers. Here, we investigate the possibility of using wheels made of different alloys/elements for fabricating fibers. One motivation to do this is whether we can switch the wheel material depending on the alloy we want to cast. Figure 6.13 shows the effect of this wheel material on melt-spinning $Fe_{40}Ni_{40}B_{20}$ fibers. When copper wheel is replaced by stainless steel wheel, the melt attaches to the wheel during ejection and it forms a solidified film on the wheel. No fiber was formed during this experiment and the only product besides of solidified film was $Fe_{40}Ni_{40}B_{20}$ powder. Copper wheel that was used already for different experiments however, does not form any remaining solidified film after melt-spinning. Besides of the different wetting behavior of copper and stainless steel, one clear difference they have is their thermal conductivity. The thermal conductivity of copper is 385 W/m.k whereas stainless steel heat conductivity is one order of magnitude smaller and is about 16.3 W/m.K.

Another type of wheel which was tested and its result was similar to pure copper wheel was CuCr1Zr (0.8%Cr,0.08%Zr,99,12%Cu) alloy wheel. The heat conductivity of this alloy is about 320 $W.m^{-1}.K^{-1}$ which is in the same order as copper wheel thermal conductivity.

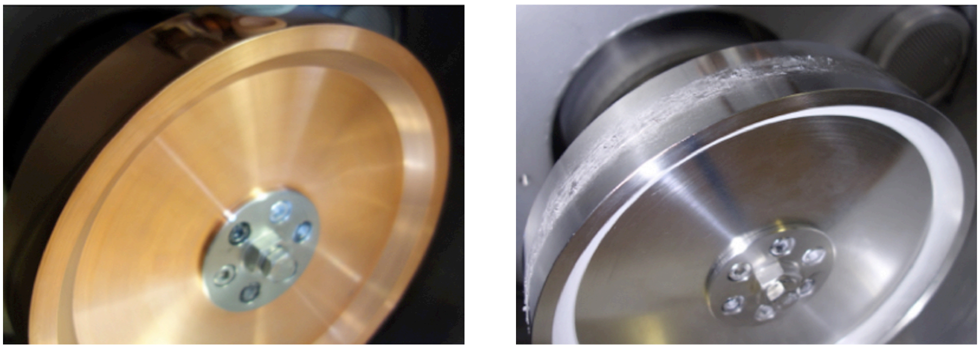

(a) copper wheel surface after melt-spinning

(b) stainless steel wheel surface after melt-spinning

Figure 6.13.: Different wheel material for melt–spinning fibers. a) Copper wheel with the heat conductivity of 385 W/m.k. b)Stainless steel wheel with the heat conductivity of 16.3 W/m.K. The stainless steel wheel forms a film of solidified alloy upon cooling.

6.4. Wheel speed

Here, we investigate the effect of wheel speed on fiber fabrication. In principle, three different wheel speeds were chosen for this purpose: 60m/s, 18 m/s, and 10m/s. The results from the wheel speed=10m/s is not presented here since the casted materials at this wheel speed were brittle needles forming powder upon handling. Similar to the graphs in section 6.2, we present in this section the size distribution of fibers width and thickness, their accumulative counting, and the accumulative counting of their cross-section aspect ratios.

Starting from the size distribution of fibers width and thickness, Figure 6.14 shows this distribution at two wheel speeds of 60m/s and 18m/s. The width mean value shifts from from 65 μm to about 20μm by increasing the wheel speed from 18m/s to 60m/s. Besides, the size distribution of width is much more narrow at higher wheel speed. Unlike the effect of slit size, here we clearly see broadening of fibers thickness size distribution at low wheel speed (18m/s). It is also clear that the mean thickness value shifts from 15μm at 18m/s to 5μm at 60m/s wheel speed.

Moving to the cumulative counting of fibers width and thickness sizes at Figure 6.15, the first observation is the big gap between the saturation behavior of fibers width and thickness at these two wheel speeds. Fibers thickness values at V=60m/s saturates 20μm and it saturates around 32μm at V=18m/s. Another observation is that at V=18m/s, thickness and width saturation curves appear to have two distinguishing slopes and behavior at two regions. Up to around 12-13μm thickness values they appear to have a certain slope which after this point gets sharper. Going to the width cumulative curve at V=18m/s, around 50% of

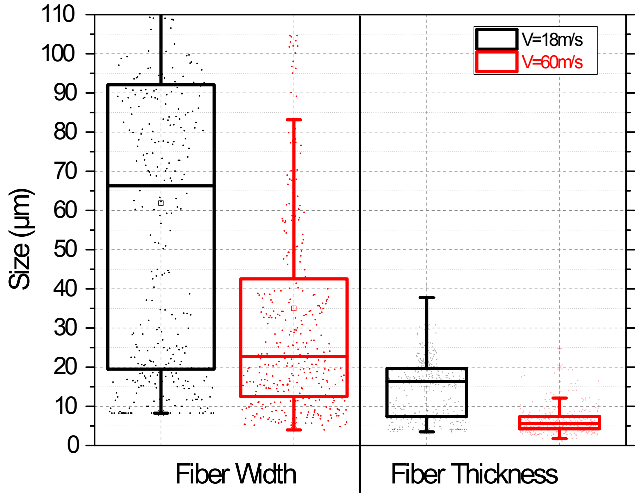

Figure 6.14.: Effect of wheel speed on size distribution of fibers width and thickness. The mean thickness value shifts from 15μm to 5μm by increasing the wheel speed from 18m/s to 60m/s. Size distribution of fibers width is significantly broader at lower speed (18m/s).

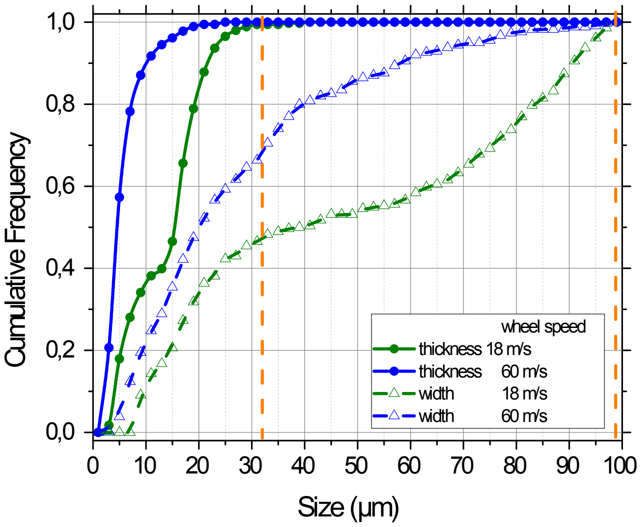

Figure 6.15.: Effect of wheel speed of cumulative counting of fibers width and thickness. The saturation behavior of fibers width and thickness at V=18m/s and 60m/s differs significantly from each other. At V=18m/s, it appears to have two distinguishing regions of fiber sizes. Thickness of fibers at both speeds saturates around 30μm. The saturation value for width of fibers is about 100μm.

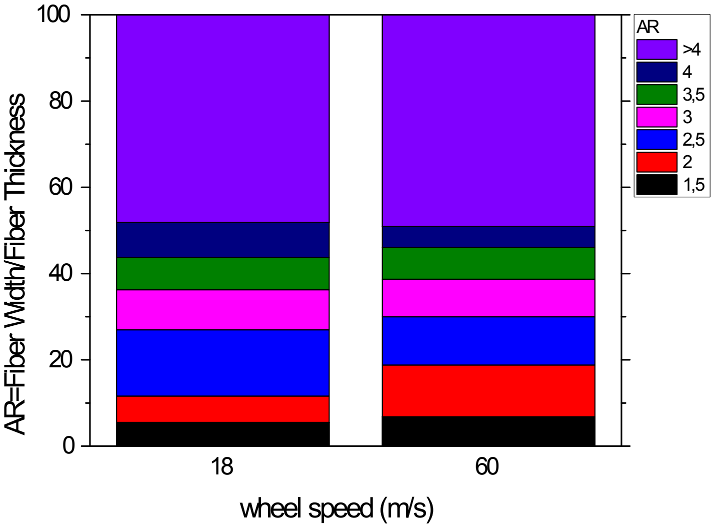

Figure 6.16.: Effect of wheel speed on aspect ratios of produced fibers. At V=18m/s, the fibers aspect ratios less than 2 is about 10% which increase twice to 20% at V=60m/s.

the fibers saturates around 45μm and the remaining 50% of fibers appear to have another type of distribution between 45μm to 100μm. Going back to Figure 6.14 to take a closer look at data point for width distribution of fibers at V=18m/s indicates the same observation.

The effect of the wheel speed on the shape of final fibers, or in other words their aspect ratios (width/thickness) is shown in Figure 6.16. At V=18m/s, fibers percentage with AR<2 is about 10% which increase twice to 20% at V=60m/s. For AR>2 no significant difference can be observed.

6.5. Applied pressure

Here we present the effect of applied ejection pressure on fabrication of fibers and their final size and shape. For an experiment with a certain slit size, it is needed a minimum applied pressure to have a continuous ejection. (This minimum pressure depends on several parameters including the type of alloy). To evaluate the effect of this pressure, three different pressures higher than minimum ejection pressure were selected: P=800 mbar, P=1000 mbar, and P=1500 mbar. Applying higher than 1500 mbar was technically not possible due to device limitation. Starting from the effect of applied pressure on the size distribution of fabricated fibers, Figure 6.17 presents the size distribution of fibers width and thickness. This figure indicates that there is no general linearity between the applied pressure and the fiber sizes. In fact, there is an optimum pressure for smallest width and thickness

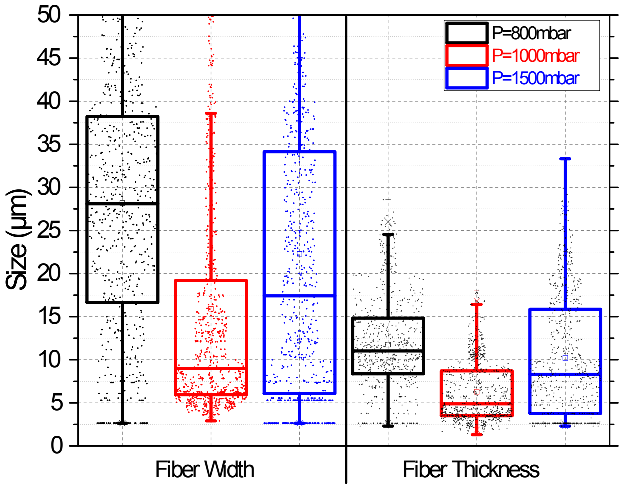

Figure 6.17.: Effect of applied pressure on size distribution of fibers width and thickness. The pressure has no linear relation with the size of fibers and in fact there is an optimum pressure for smallest fibers at P=1000mbar.

values at P=1000 mbar. The highest width mean value belongs to the lowest pressure, P=800 mbar ($\approx 27\mu$m). The width mean value is 3 times smaller at P=1000 mbar ($\approx 9\mu$m). Width mean value shifts to $\approx 17\mu$m at P=1500 mbar. Another observation is the distribution of fibers width which is the broadest at P=1500 mbar, and is the most narrow one at P=1000 mbar. Looking at the fibers thickness distribution, again the broadest distribution belong to P=1500 mbar. The mean thickness values is 2 times higher at P=800 mbar (10μm) comparing to P=1000 mbar (5μm). P=1000 mbar appears to be able to make the smallest fiber sizes with the most narrow size distribution.

Going to cumulative counting of fibers sizes with the bin size of 5μm at Figure 6.18, we can observe better the behavior of their size saturation behavior. Clearly, the thickness curve at P=1000 mbar deviates significantly from the curves at P=800 mbar and 1500 mbar. Fibers thickness values saturate $\approx 15\mu$m, while thickness values at P=800mbar and 1500mbar saturates $\approx 30\mu$m. Looking at width curve, each curve deviates from each other. Besides, if take a closer look at width curve of P=1000bar, we can see that up to 15μm, the slope of the curve is sharp and after this point, its slope gets smaller which means in this region there are more scattered width values. This is also visible if we take a look at the data points inside the boxchart of P=1000 mbar at Figure 6.17.

Figure 6.19 shows the effect of applied pressure on roundness of fabricated fibers. More than 60% of fibers at P=1500mbar has the aspect ratio of less than 2 (AR<2),

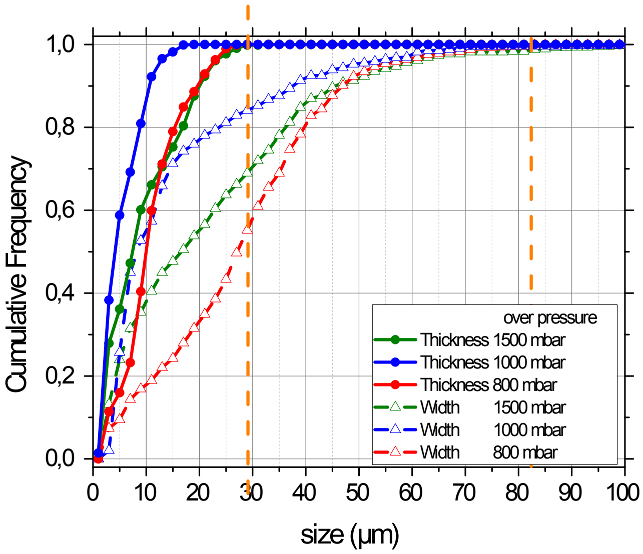

Figure 6.18.: Effect of applied pressure on cumulative counting of fibers width and thickness. P=1000 mbar appears to have the sharpest saturation slope for its cumulative width and thickness counting.

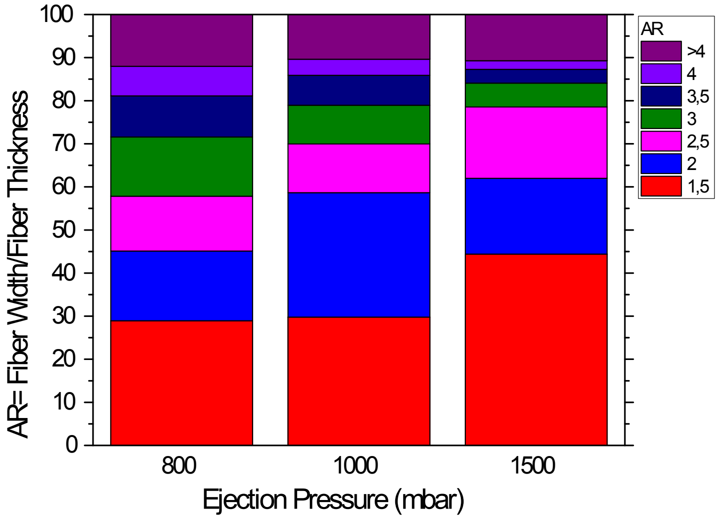

Figure 6.19.: Effect of applied pressure on aspect ratio of produced fibers. The highest applied pressure (P=1500mbar) contributes to the fibers with the smallest aspect ratios: AR<1.5. There is a continuous increase of fiber percent with low aspect ratios by increasing the applied pressure.

and at P=1000 mbar, this percentage is slightly less, while at P=800 mbar, it is limited to 45%. Another noticeable difference is that if we take a look at AR<2, the difference between P=1000 mbar and P=1500 mbar is negligible whereas if we take a look at AR<1.5, their percentage is equal at P=1000 mbar and P=800mbar while it is significantly more at P=1500mbar.

6.6. Ejection temperature

In this part we study the effect of ejection temperature or in other words overheating on fiber formation and their shape and size distribution. It needs to be noted that here only the overheating is studies and not the heating program. Two different temperatures were selected for this purpose : 1350°C and 1450°C. Going to higher temperatures were not technically possible due to maximum safe temperature BN crucible can stand to. Lower than 1350°C, the surface tension is too high to be able to eject the melt. Since the melting point of the alloy is ≈1150°C, the overheating used for this alloy is: ΔT=200°C,ΔT=300°C.

Figure 6.20 shows the effect of ejection temperature on size distribution of fibers width and thickness. According to this figure, size distribution of fibers width is very broad at higher ejection temperature (T=1450°C). However, its mean value is slightly smaller at T=1450°C comparing to T=1350°C. The difference between the mean values of fibers thickness at these two temperatures is negligible but its distribution is broader at lower temperature (T=1350°C).

Studying the cumulative counting of fibers sizes, Figure 6.21 shows no significant difference in saturation behavior of fiber sizes in the cumulative counting of fibers width and thickness.

Comparing the fibers shape and circularity at these two temperatures in Figure 6.22, we see that up to the aspect ratio of <1.5, higher temperature (1450°C) contributes to slightly more number of fibers. However if we compare the aspect ratios of AR<2, lower temperature (1350°C) contributes to larger number of fibers significantly. In fact, almost 60% of fibers have AR<2 at T=1350°C, while at T=1450°C, only ≈ 45% of fibers have AR<2.

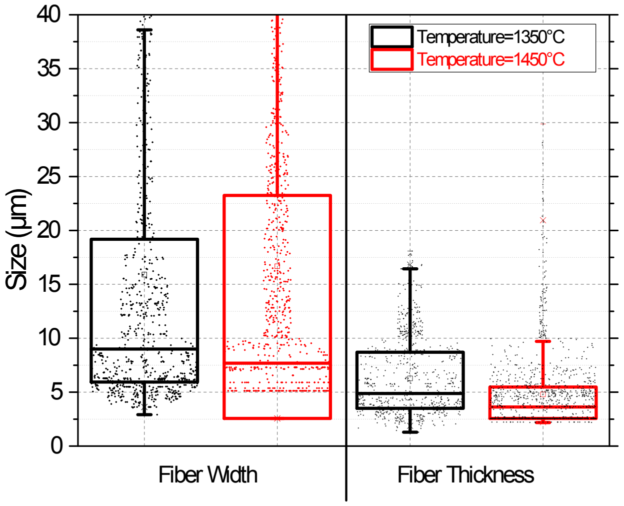

Figure 6.20.: Effect of ejection temperature on the size distribution of fibers width and thickness. Higher ejection temperature (1450°C) contributes to smaller mean values of fibers width and thickness. However, the size distribution of fibers width is significantly broad at higher temperature.

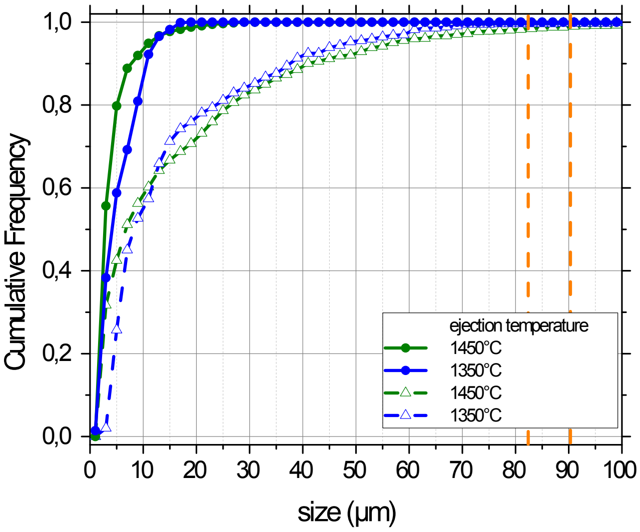

Figure 6.21.: Effect of ejection temperature on cumulative counting of fibers width and thickness. No significant difference can be seen in saturation behavior of fiber sizes at both ejection temperatures.

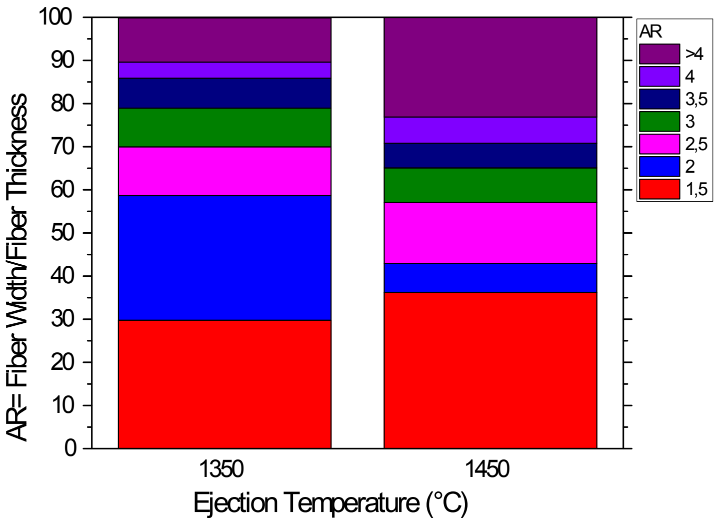

Figure 6.22.: Effect of ejection temperature on aspect ratio of produced fibers. At T=1350°C almost 60% of fibers have the aspect ratio of less than 2(AR<2), while at T=1450°C, only ≈45% of fibers have the aspect ratio of less than 2.

6.7. Slit distance to the wheel

Another parameter investigated to observe its effect on the size and shape of fibers was the distance between the slit nozzle opening and the wheel surface. This distance is shown here as "G". For safety reasons, this distance could not be closer than 100μm, and more than 300μm distance does not contribute to fiber/ribbon formation at standard melt-spinning conditions (see the standard conditions at Table 5.1). Here the result of fibers formed at three different distances 100μm, 200μm, and 300μm are presented. The efficiency of forming fibers by ejecting at G=300μm, 200μm, and 100μm were different as follows: 10.7%, 86.6% and 77.2%.

The effect of G on fibers size distribution of width and thickness is shown in Figure 6.23. At the first glance, there is no linear relation between G and fibers size mean values. In fact, at G=200μm fibers width and thickness mean value is minimum. Fibers width distribution is significantly broader at G=100μm and its width mean value is also 2 times larger than G=200μm and G=300μm. The distribution of fibers width at G=200μm and G=300μm is almost the same. But the most narrow thickness value distribution belongs to G=300μm. In general, the thickness mean value and distribution does not seem to be affected significantly at different G values.

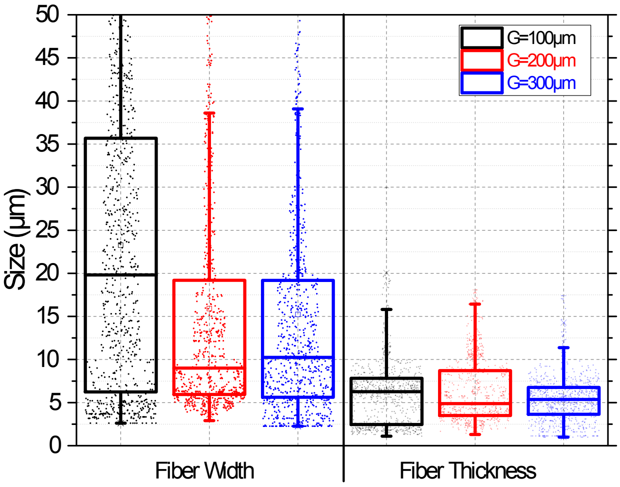

Figure 6.23.: Effect of slit distance to the wheel (G) on size distribution of fibers width and thickness. It seems that at all G values, the thickness size distribution is almost the same. At G=100μm, we observe the broadest width distribution, and its mean value is 2 times higher than the mean value of G=200μm and G=300μm.

Going to cumulative counting of fibers width and thickness at Figure 6.24, we observe that the thickness curve for all G values is almost the same. For width curve, G=100μm deviates significantly from the other two G values.

Figure 6.25 shows the aspect ratio of fibers obtained by melt-spinning at different slit distances to the wheel. At G=100μm we have the lowest number of fibers with aspect ratio less than 2. In fact, only around 25% of fibers have the AR$<$2, while this value for G=200μm and G=300μm is around 60% and 50% respectively. Thus, there is no linear increase of fibers numbers with small aspect ratios if we increase the distance between the slit and the wheel. It seems like for most round and circular fibers, we need to find an optimum value of G, which here is 200μm.

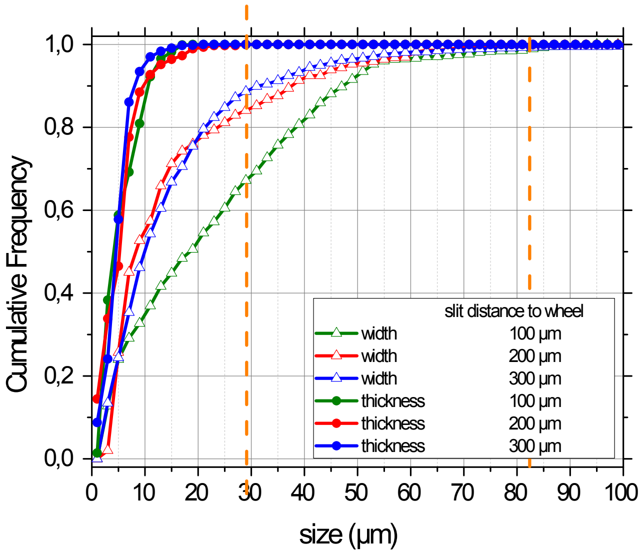

Figure 6.24.: Effect of slit distance to the wheel (G) on cumulative counting of fibers width and thickness. The saturation behavior of thickness values is almost the same at all G values. There is a large deviation of reaching maximum width value for G=100μm from the other G values.

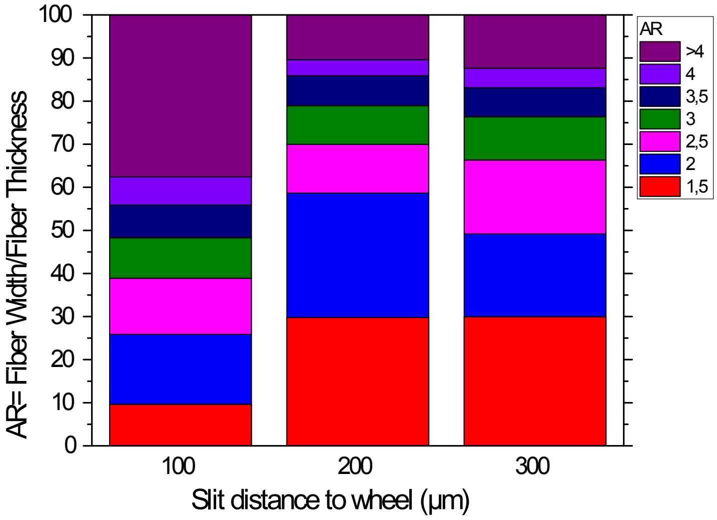

Figure 6.25.: Effect of slit distance to the wheel on aspect ratio of produced fibers. There is no linear relation between increasing the distance between slit and the wheel and the number of circular fibers. In fact, there is an optimum value for most circular fiber at G=200μm.

6.8. Chamber pressure

In this section we examine the effect of chamber pressure on fabrication of fibers. Different type of gases can be used for this purpose but we are testing all the pressures by Ar gas. Three different chamber pressures were chosen for this reason: P$<10^{-5}$mbar , P=400mbar, and P=800mbar. Figure 6.26 shows the effect of chamber pressure on size distribution of fibers width and thickness. The mean width value of fibers is shifted to 5 times bigger values at P$<10^{-5}$mbar. Their distribution is also larger than higher pressures. The mean thickness value at P$<10^{-5}$mbar is 2 times bigger than the mean thickness value at other higher pressures. However, it has the most narrow thickness size distribution. In terms of thickness at P=400mbar and P=800mbar, their mean value is almost equal except higher pressure has slightly narrower size distribution. Based on this boxchart figure, one can not see a linear relation between chamber pressure and narrow size distribution of fibers width and thickness.

Going to cumulative counting of fibers width and thickness at Figure 6.27, we see that the deviation of width values at P$<10^{-5}$mbar from other two pressures is significant. The thickness curve at P$<10^{-5}$mbar has the same saturation behavior of the other two chamber pressures, and is only shifted. Taking a closer look at the thickness curve of P=400mbar and P=800mbar, their slope is sharp in the

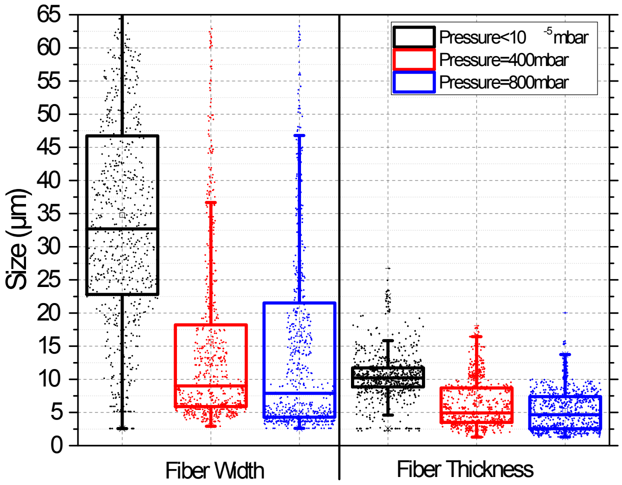

Figure 6.26.: Effect of chamber pressure on size distribution of fibers width and thickness. At P$<10^{-5}$mbar, width mean value is 5 times and thickness mean value is 2 times larger than higher pressures.

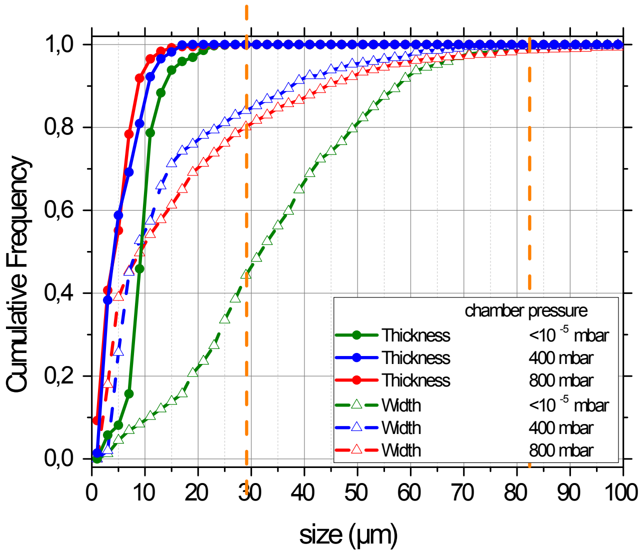

Figure 6.27.: Effect of chamber pressure on cumulative counting of fibers width and thickness. The saturation behavior of thickness values is almost the same at all chamber pressures and is only shifted to bigger values at P<10^{-5}mbar. The deviation of width values at P<10^{-5}mbar from the other pressures is significant.

beginning and they get to start saturated after they reach 15μm. The same thing is visible at Figure 6.26 about the data point of fibers width at P=400 and 800mbar.

Figure 6.28 shows the effect of chamber pressure on the shape of fibers. The most ribbon-shaped fibers are fabricated at P<10$^-$5mbar. Less than 20% of fibers at this pressure has the AR<2 and it is even less than 10% of fibers with AR<1.5. On the contrary, 60% of fabricated fibers at 400mbar has AR<2 which means they are more round in their cross section. Based on this graph, the optimum pressure for obtaining the most circular fibers is at P=400mbar.

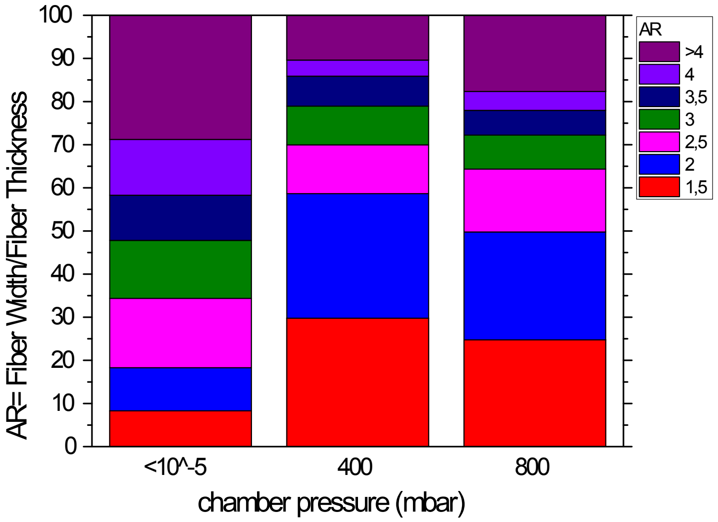

Figure 6.28.: Effect of chamber pressure on aspect ratio of produced fibers. There is no linear relation between increasing the chamber pressure and the number of circular fibers. The lowest number of round fibers belong to P<10^{-5}mbar (less than 10%), while this value is almost 60% at P=400mbar, and is maximum.

6.9. All parameters

In this section we put all the data together from all experimental parameters we studied before together to be able to find the optimum parameters for fabricating fibers. We evaluated their deviation from perfect circular fibers by measuring their cross section aspect ratio (width/thickness).

We previously observed that by changing different experimental parameters, the most significant effect is on fibers width; and the thickness, except in some cases, were not affected significantly. To have the most circular fiber they need to have AR<2. Figure 6.29 shows the relation between the width of fibers obtained from all the data and their corresponding aspect ratios. This color map counting graph shows that to have 1<AR<2, most fibers with such aspect ratios have the width of maximum 10μm. If we add each color (which corresponds to a certain percentage of fibers) together for width<10μm, we see that 50% of fibers with width<10μm, have AR<2.

We put all the experimental parameters and the size analysis of their resulting fibers together to find the correlation between size and experimental parameters. Figure 6.30 shows how thickness of fibers is related to parameters such as slit size, applied pressure and wheel speed. Of course, here we assumed the material prop-

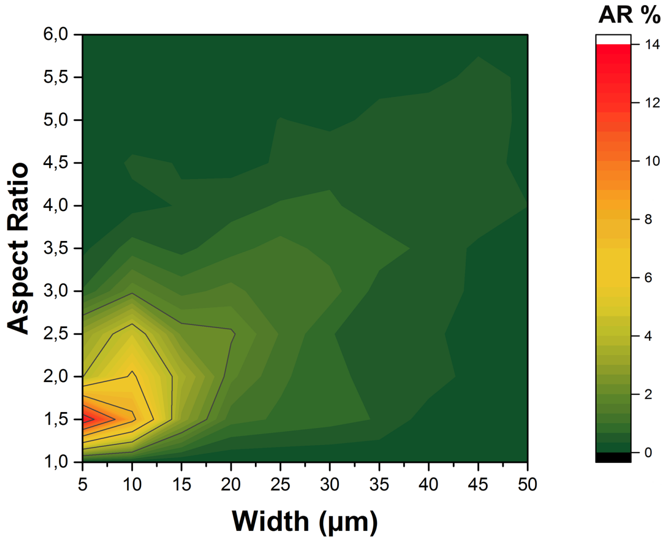

Figure 6.29.: The relation between fibers width and their corresponding aspect ratio (AR=width/thickness). The majority of fibers with width<10μm, have AR<2 and thus have round shape.

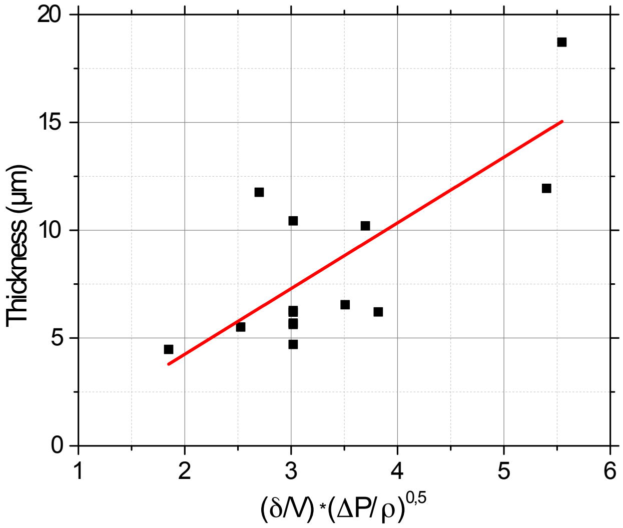

Figure 6.30.: Correlation between fibers thickness and melt-spinning parameter. According to this figure, this correlation can be written as equation 6.1.

erties to be constant and the constant values are obtained based on $Fe_{40}Ni_{40}B_{20}$ alloy physical properties. This relation can be written as:

$$t = 0.0346(\frac{\delta}{V})\sqrt{\Delta P} - 1.84 \tag{6.1}$$

Where: t=thickness, δ=slit size, V=wheel speed, and ΔP=overpressure.

6.10. Fibers reproducibility

One of the key points of producing fibers on flat wheel is their reproducibility. To be able to address whether running experiments sequentially will affect the fibers size production, several experiments right after each other were done by melt-spinning under same experimental conditions. No further treatment or polishing of the wheel was carried out in between. The size distribution of produced fibers is shown in Figure 6.31. As it can be seen in, the fibers size does not get affected by sequential running of the experiment, considering slight roughening of wheel surface, the heat generated on the wheel, and other slight experimental variations. It also shows that by applying the same experimental parameters, the same fibers can be reproduced.

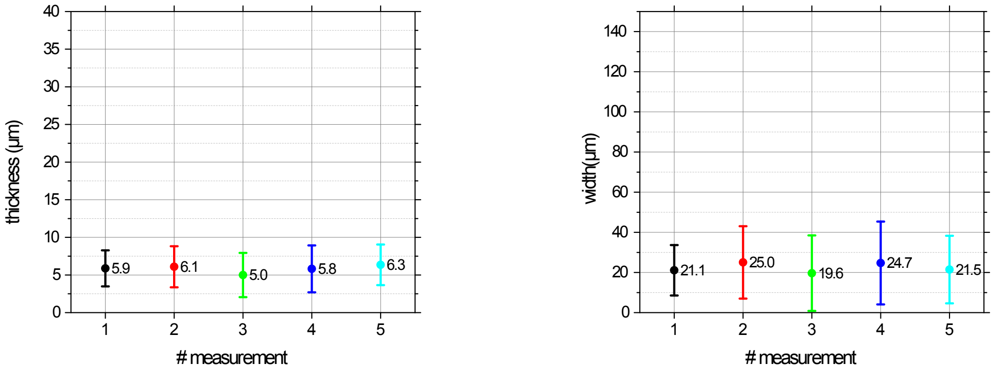

(a) Fibers thickness

(b) Fibers width

Figure 6.31.: Sequential production of fibers by melt-spinning under same experimental conditions. The fibers size distribution for their width and thickness has the same range for all experimental results.

6.11. Other materials

Up to now, all the experiments for fabricating fibers were done using $Fe_{40}Ni_{40}B_{20}$ amorphous alloy. To see whether the same technique can be used with the same principle for other classes of materials, different materials were tested. Four categories of materials were used for this purpose. Metal elements such as Zn, Al, Ag, and Cu; conventional alloys such as stainless steel grades: 316-Ti, 316L, and 304 austenitic grades; intermetallic alloys such as Ni_3Al and $Ni_3AlB_{0.4}$; and amorphous alloys such as commercially known vitrovac 6025X.

In principle, for each new material, melt-spinning parameters needed to be optimized. Here we show a SEM picture as an example from each fiber material. Each test for fabricating these fibers were repeated several times and were further analyzed using XRD (and in some case more tests for mechanical and magnetic characterization). Figure 6.11 shows the SEM pictures of fibers made of metal elements: Al, Ag, Zn, and Cu.

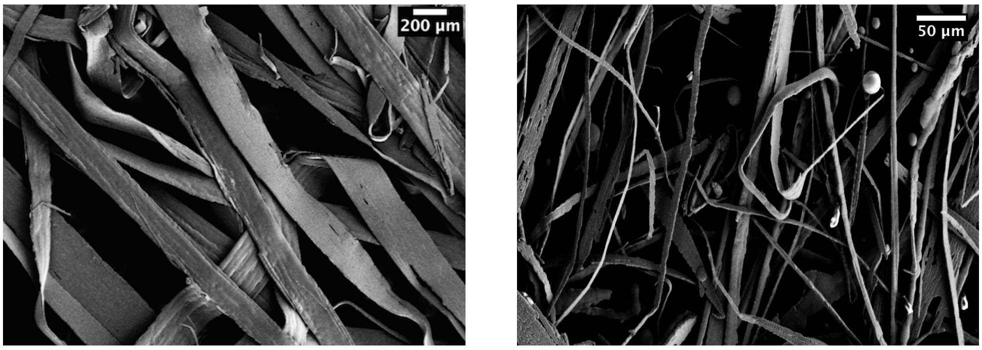

(a) Al fibers **(b)** Cu fibers

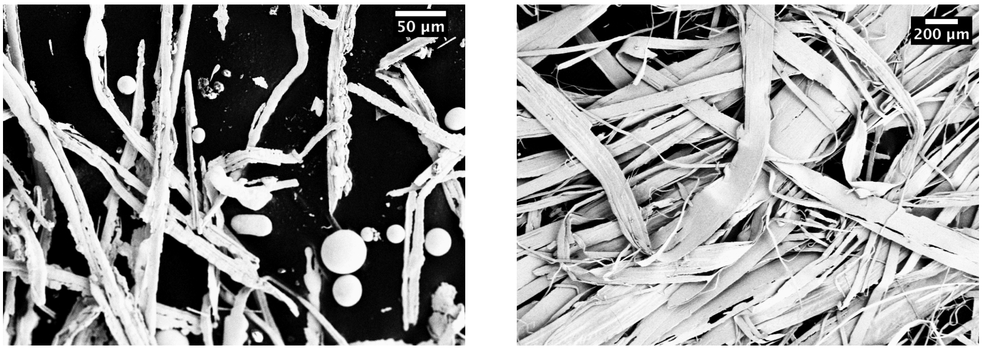

(c) Ag fibers **(d)** Zn fibers

Figure 6.32.: SEM pictures of casted metals by melt-spinning. a)Aluminum fibers b)Copper fibers c) Silver fibers d) Zink fibers. They are almost rectangular in the shape of ribbons. Silver and Copper tend to have smaller sizes.

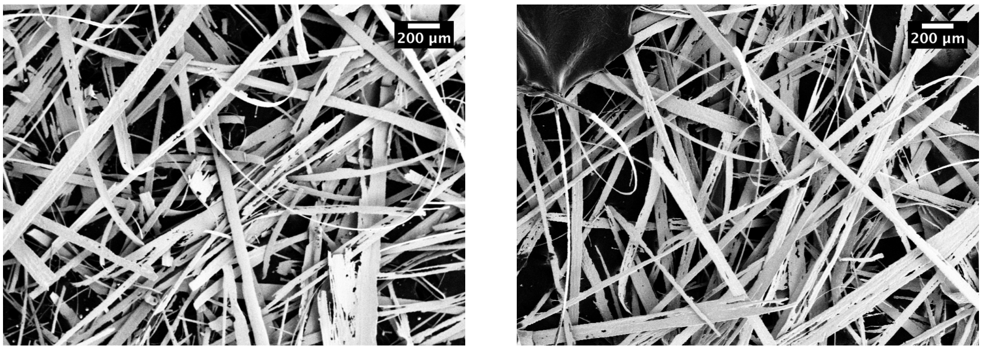

(a) Ni_3Al fibers **(b)** $Ni_3AlB_{0.4}$ fibers

Figure 6.33.: SEM pictures of casted intermetallic alloys by melt-spinning. a)Ni_3Al fibers b)$Ni_3AlB_{0.4}$ fibers. They are almost rectangular in the shape of ribbons.

As it can be seen in this pictures, in principle it is possible to make micro-ribbons/fibers using single metal elements. However, they do not seem to have a homogeneous size distribution and their cross sections are mostly rectangular instead of circular. Cu and Ag seems to be able to make smaller fibers. In case of silver, the irregular shape of casted material cannot be considered neither perfect fiber nor ribbon. There are some round particles among the Ag fibers as well.

Moving to the next class of materials, two different compositions of alloys were selected for melt-spinning: Ni_3Al and $Ni_3AlB_{0.4}$. It does not seem to be a big difference between these two alloys based on their SEM pictures in Figure 6.11. Although, their behavior during casting is slightly different. Some small round fibers are visible in their batch but are mostly ribbon-shaped with rectangular cross sections. There can be seen holes and defects on the fibers/ribbons surfaces. The surface of ribbons/fibers does not seem to be smooth and is quiet rough.

Another class of material used was conventional alloys such as stainless steel grades. For this purpose, 3 different austenitic grades of stainless steel were casted by melt-spinning: 316-Ti, 316-L, and 304. The exact chemical composition of these alloys can be found in Appendix. Figure 6.11 shows the SEM pictures of these fibers. The smallest fibers with mostly round shape seems to be possible using 316-Ti grade. Some flat-shaped bigger micro-ribbons are also visible but they are mostly smaller fibers in the range of 10μm to 15μm width. Most irregular shape of fibers with lots of surface holes and defects belong to 316-L stainless steel. 304 stainless steel fibers tend to be larger but are mostly rectangular ribbon-shape.

The last group of material which is the most appropriate one to work with melt-spinning are those alloys designed to form glassy structure. Figure 6.11 shows the SEM pictures of fibers made of $Fe_{40}Ni_{40}B_{20}$ and a Cobalt-based alloy commercially

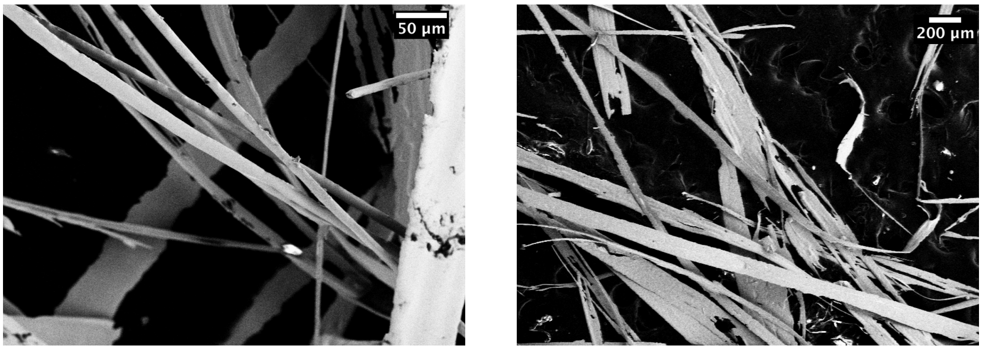

(a) 316-Ti stainless steel fibers

(b) 316L stainless steel fibers

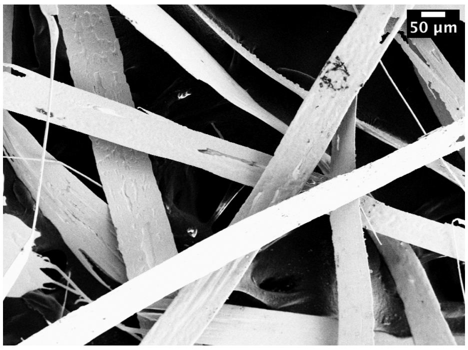

(c) 304 stainless steel fibers

Figure 6.34.: SEM pictures of casted stainless steel alloys by melt-spinning. a)316-Ti stainless steel fibers b)316-L stainless steel fibers c)304 stainless steel fibers. 316-Ti stainless steel is able to make more circular smaller fibers in the range of 10 to 15μm.

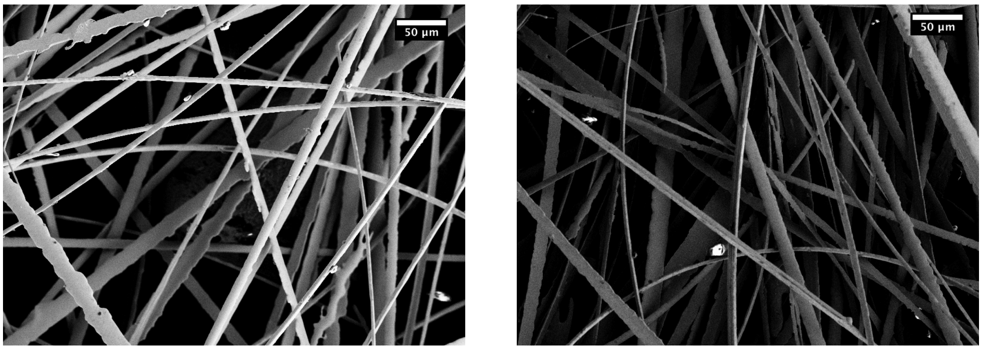

(a) Vitrovac 6025X alloy fibers

(b) $Fe_{40}Ni_{40}B_{20}$ alloy fibers

Figure 6.35.: SEM pictures of casted amorphous alloys by melt-spinning. a)vitrovac 6025X fibers b)$Fe_{40}Ni_{40}B_{20}$ fibers. Fibers made of vitrovac seems to have smaller sizes and more round/circular shape.

known as vitrovac 6025X. Both of these alloys are designed to form amorphous alloy. They are easy to be casted and processed by melt-spinning. Fibers made of vitrovac seems to be mostly circular and even more circular than fibers made of $Fe_{40}Ni_{40}B_{20}$. One small chapter is allocated for characterization of vitrovac fibers at the end of this thesis because of its unique magnetic properties.

6.12. Fiber formation

One of the ways to understand the behavior of melt-spinning for fiber formation was using the high-speed camera movies from the ejection process. At this section two movies taken from ejection process by applying standard parameters using 25μm and 50μm slit sizes and are shown in Figure 6.37.

As it can be seen in Figure 6.37, by using 50μm slit size, during the melt ejection a stationary melt-puddle forms. It can also be seen that some small droplets as a minor product also get ejected from the slit. The size of this stationary puddle is about 3000μm. Using 25μm slit size, no melt-puddle forms. single melt droplets with the diameter of 1200μm are formed and ejected from the slit by the constant time interval. It can also be seen that the first ejected droplet does not wet the wheel and moves further on the surface of the wheel whereas the second droplet vanishes (wets) the wheel surface at around 8mm distance from the center of slit opening. This disappearance distance to form the thin film is approximately constant and can be seen in the full video attached to this thesis file in forms of a video. Due to low resolution of camera, the creation of film cannot be captured during high-speed camera filming. The thickness of the thin film is approximated afterwards based on the thickness of formed fibers.

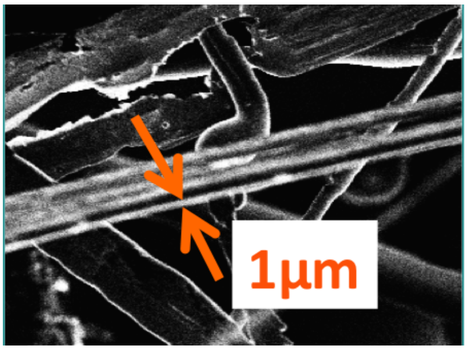

Figure 6.36.: SEM picture from a ribbon produced by melt-spinning partially broken to smaller width down to 1μm.

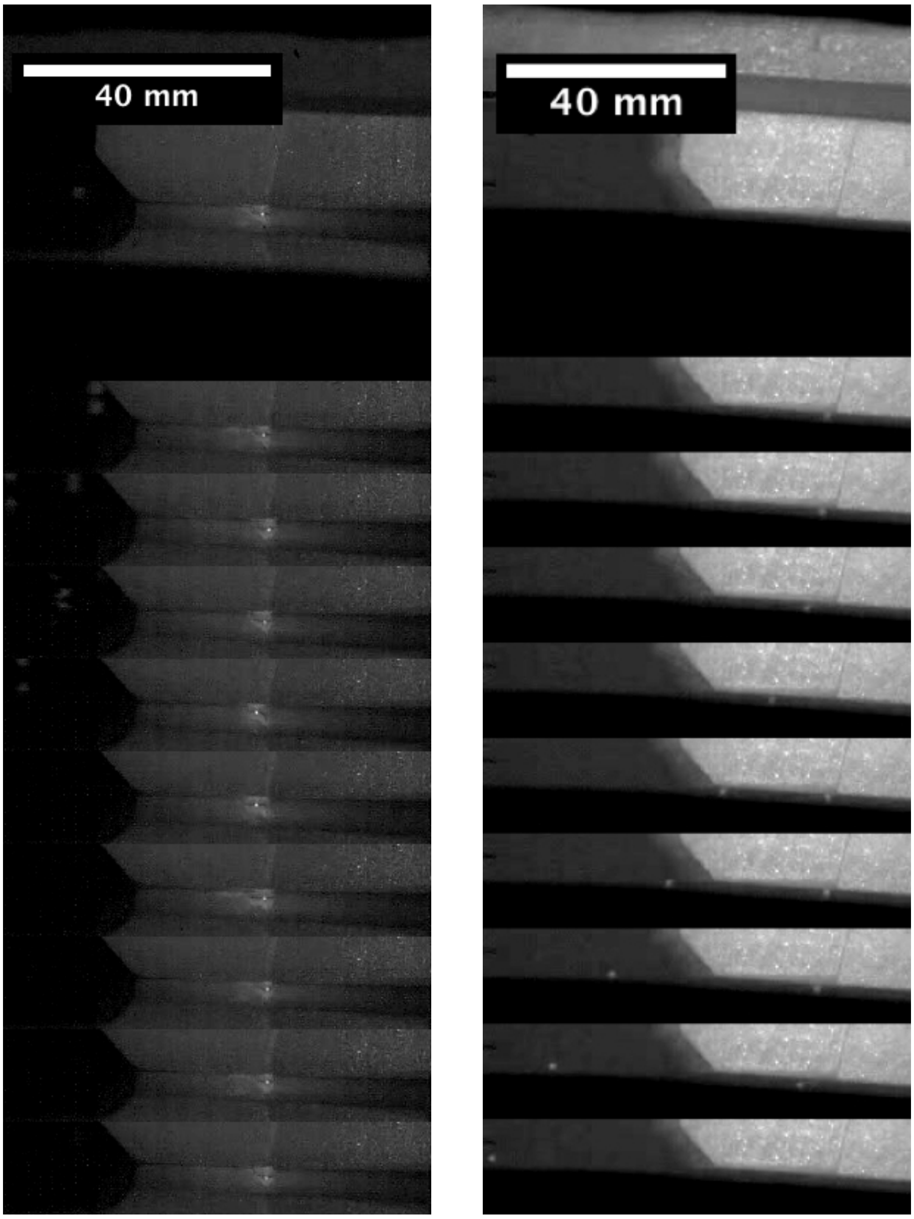

(a) 50μm slit size **(b)** 25μm slit size

Figure 6.37.: images taken from high speed camera movies during melt ejection a) Creation of melt-puddle during melt ejection using 50μm slit size. The puddle is stationary. b) No puddle creation using 25 μm slit size, and melt ejection droplet by droplet. There is a time interval between the ejection of each droplet.

Another way to study the fiber formation by melt'spinning was to take a closer look at its failed products. Figure 6.36 shows the ribbon which was broken to smaller widths down to 1μm but it could not break completely along its length.

7. Discussion

7.1. Experimental parameters effect

Modeling and studying melt-spinning system for ribbon formation was done by different groups and scientists[58], [59], [56]. Starting from the same system and modifying the device for micro-fiber fabrication, the original idea initiated from breaking down the melt puddle or in other words the ribbon to ribbons with smaller widths and eventually making micro-fibers. Following this idea, the first modification done on the device was changing the type of wheel surface structure.

The result of this idea which was shown in Figure 6.4 shows that by roughening and structuring the wheel we are able to make this transition from ribbons to micro-ribbons. Since we are starting from a ribbon system going to the direction of microfibers, it is difficult to define an exact transition point to distinguish between the terms "micro-ribbons" and "micro-fibers". That is why from this point on, we consider all micro-ribbons as micro-fibers and in stead we evaluate their deviation from the perfect circular micro-fiber size and geometry. Therefore, structuring wheel was one successful approach to generate microfibers by melt-spinning. This is the first time, one could generate fibers using melt-spinning.

Going back to Figure 6.4, based on the wheel surface structures, one could expect the production of ribbons with the width comparable to the distance between the grooves on wheel surface. However, looking at the mean width values of micro-ribbons fabricated on the wheels contradict this prediction. In fact, in all cases, the fibers width is smaller than the distance between grooves or the size of the grooves themselves. Among different wheel types, the most promising small microfibers were made on wheel type C. The reason for this result cannot solely depend on the size of the grooves this wheel has, and it could be more actually the effect of how the melt wets the wheel surface.

Going back to Figure 6.5, it depicts one major problem of this approach. Indeed, the grooves make the molten alloy film to break down to smaller films and because of the groove structure, the liquid films cannot easily dewet the surface or laterally detach from the wheel. Thus, they attach to the wheel surface. Solidified alloy inside the grooves do not allow the wheel to have the same surface for reproducing the same fibers, and reproducibility is one of the concerns on this project. This is why in the next part, the focus of modifying the device for fiber formation was moved toward other parts and parameters. Then the flat wheel remained as the constant part of melt-spinning.

The second major geometrical change toward fabricating fibers was to move from bigger slit sizes to smaller slit sizes. Starting from 400μm slit size toward 25μm slit size, we move from small ribbons to small microfibers (see Figure 6.2). As it was already mentioned in Figure 6.2 before, if we assume a line for both fibers width and thickness vs slit size, the slope of this line is 8.5 times larger for fibers width comparing to fibers thickness. If at each slit size, the minimum ejection pressure is used, keeping all the other parameters constant, it could be expected to form a film with the same thickness. This can be the reason that fibers thickness does not depend significantly on the slit size in comparison with fibers width. We observed from Figure 6.9 that the the slit size is around 5 times larger than the fibers width. Russew et al [55] explained that in PFMS, the width of the ribbon is equal to the slit opening when the distance between wheel and slit is small(G is small). However, here, even though we are close to the wheel, the slit size is 5 times larger than the fibers width. This could mean the ribbon with the width equal to slit size can break down to smaller ribbons and fibers eventually.

The cumulative counting of fibers width and thickness can be a good approach to observe the behavior of fiber formation under different experimental conditions. Since it does not only present the size distribution of fibers and it also shows how the size distribution gets saturated, when the behavior of system is different, its saturation behavior deviates from the other curves. Looking at Figure 6.11, we see that there are 3 categories of size saturation for the width of the fibers. One belongs to the smallest slit size 25μm, next one belongs to 50μm and 100μm, and the third category belongs to 200μm slit size. It is not incorrect if we say the larger the slit size gets, the closer we become to the original melt-spinning ribbon formation system. So here, the 200μm slit size has a big deviation from smaller slit sizes such as 50μm and 100μm. The next shift is when we reach 25μm slit size. At Figure 6.37 from high speed camera movie we saw that there is a melt puddle at 50μm slit size during ejection while no melt puddle forms for 25μm and the whole process of fiber formation relies on droplets wetting the wheel surface with a constant time interval between each droplet. Though, the source of width value deviation at 25μm and 50μm slit sizes can be understood based on their different mechanism of film formation. This droplet system might be a source for rounder fibers as well.

We observed at Figure 6.12 that at 25μm slit size, we have more than 50% round fibers. This percentage of round fibers decreases significantly as we get closer to bigger slit sizes.

Since the whole process of fiber formation relies on wetting a wheel surface, rapid solidification and then detaching the wheel, it is needed to know the possibility of using different wheel materials. The wheel material is important from two main aspects: first, the wheel is a tool to remove the sink of heat quickly from the molten metal film; which means it is important to have a high heat transfer coefficient. And secondly, to be compatible with the alloy we want to use, so how the material can wet the wheel surface. It is clearly not possible to go to the range of 16.3 W/m.K heat conductivity for the wheel (based on the result of melt-spinning on stainless steel wheel), and one order of magnitude higher heat conductivity is needed to be able to quench the material fast enough prohibiting lateral solidification of molten metal on the wheel. As it was already mentioned, the type of wheel material does not matter as long as the alloy can wet its surface and it has heat conductivity in the order of 385 W/m.k, and it does not need necessarily to be made of pure copper.

Until here, we mostly talked about parameters which we need to modify the device itself such as structuring the wheel surface, changing the size of the slit used or the type of the wheel material. However, from now on if we stick to the flat copper wheel with a certain slit size, the rest of the parameters can be investigated easier. One key parameter is the wheel speed. The effect of wheel speed on melt-spinning ribbons has been already investigated enough [56], [55]. If we use 50μm slit size which forms the puddle, the wheel speed determines the length of this puddle (eventually length of the fibers). If we have a constant applied pressure (which means constant ejection speed), the mass per unit area coming on the wheel is constant at any wheel speed. What differs is how fast this mass can be removed from the wheel upon solidification. So the immediate effect of wheel speed must be on the quenching rate of the alloy. This was also studied by Tkatch et al [56] for melt-spinning ribbons and he found out that the wheel speed affect cooling rate and the consequent cooling rate influences ribbon thickness (cooling rate $\propto d^{-3.1}$). Besides, the faster this wheel rotates, the thinner the formed film will become. So one should expect that the fibers thickness must be changed a lot at different wheel speeds. Looking at Figure 6.14 we see that the thickness from the mean value of about 5μm, reaches more than 15μm (3 times larger). What was observed at cumulative counting of fibrs size in Figure 6.15 was two different slopes for fibers width and thickness at V=18m/s. One possible explanation is that at low speeds, the mass flux removal rate is slower than higher wheel speeds. Keeping a mass for longer time on the wheel might lead to film attaching to the wheel. As time goes by and more mass comes to the wheel, a thicker film forms because previous film could not detached the wheel yet. Although wheel speed affects the fibers roundness as well, but its effect on this geometry is not as significant as its effect on fibers thickness.

Changing the ejection pressure in the melt-spinning system from the minimum pressure needed to eject the metal to higher pressures was investigated next. From the Figure 6.17, it was obvious that there must be an optimum pressure to obtain the smallest fibers width and thickness, which here happened to be 1000mbar. Even looking at the cumulative count of fibers sizes at Figure 6.18 shows that the behavior of the system at optimum pressure differs from lower and higher pressures (800mbar and 1500mbar here). Looking closer at Figure6.19 however has some interesting information in it. The roundest fibers with the aspect ratios up to 1.5 are more than 40% at the highest pressure (1500mbar). If we consider 800mbar as the lowest ejection pressure, it seems like that the best ejection pressure for forming fibers has to be slightly higher than the lowest ejection pressure.

The ejection temperature clearly affects the viscosity and surface tension of the melt, eventually the fiber formation. However, one thing must be remembered here and that is the fact that here, it is more emphasized on the amount of overheating (ΔT=$T_{ejection} - T_{melt}$). In fact, the heating program itself matters more in case of alloys with certain phase diagrams. e.g. when there is a phase separation or precipitation involved. Since the maximum temperature the BN crucible could tolerate was around 1500°C, and the melting point of $Fe_{40}Ni_{40}B_{20}$ alloy was about 1150°C, not so many different overheating ranges could be selected. Here the overheating of about 200°C and 300°C were chosen. Less than 200°C overheating, the viscosity of the melt and the surface tension is so high that melt ejection is almost impossible. More than 300°C overheating is also not possible due to crucible restriction. However, even only 100°C difference at overheating can clearly result in different fibers sizes. According to Figure 6.20, the mean thickness value of fibers at higher temperature (1450°C) is slightly smaller than the lower temperature (1350°C). Instead, the width of the fibers fabricated at higher temperature have much wider size distribution comparing to lower temperature(their mean value is still smaller though). One reason for this wide distribution of fibers width can be explained by the limitation of the device at its current state. Due to lack of temperature control that can keep the temperature constant during the whole time of ejection, and even though there is a temperature system installed, its feedback is not fast enough for such short ejection times; thus, starting from 1450°C, the fluctuations are stronger toward the lower temperatures, leaving the fabrication on a range of temperatures in stead of a certain ejection temperature. Of course, if the temperature drops lower than melting point or even a bit above that point, the ejection would stop immediately. In stead, at 1350°C this fluctuation is smaller leading to narrower size distribution. Apart from the size distribution, the behavior of melt in creating fibers at these two selected temperatures is really similar and can be clearly seen in Figure 6.21.

Figure 6.22 shows the effect of ejection temperature on morphology of fibers. Around 60% of fibers have AR<2 at T=1350°C whereas this number is limited to 42% at T=1450°C. One possible explanation could be due to higher surface tension of melt at lower temperature which makes them have rounder borders, eventually making them more circular.

The other parameter which affects fabricating fibers is the distance between the slit nozzle opening and the wheel surface (G). Indeed, if this distance is considerably larger than the slit size we might exit completely from planar flow melt spinning system and reach chill block melt-spinning system[56]. In this regard, and to see how this distance affects the fiber formation three G values were selected: 100μm, 200μm ,and 300μm. Lower than 100μm was not possible due to the safety distance between the wheel and the nozzle in case of wheel vibration, and more than 300μm distance could not form any fibers. Before we start analyzing the shape or size of the fibers, it is important to point out that the melt ejected from the slit did not form equal amount of fibers at all G values. So there must be a critical distance that more than that no fiber can be formed. At G=300μm, we observed that more than 89% of ejected melt solidifies in form of particles and only about 11% wet the wheel surface forming fibers. However in case of G=200μm and G=100μm, this number (amount of fibers) is about 86% and 77% respectively.

Continuing on how G could affect the size distribution of fibers in Figure 6.23, we can see the mean value of the thickness at all G values is still in the same range although it has a bit narrower size distribution at G=300μm. However, in case of fibers width size distribution, there is a big difference between G=100μm with G=200μm and G=300μm. The mean value is shifted to values 2 times larger, and the distribution is much wider. At G=200μm and G=300μm, they have the same width mean value and size distribution.

Figure 6.24 shows what we have just described in a more clear way. The behavior of thickness size values is the same at all G values meaning the distance between the wheel and the slit nozzle does not affect the thickness of the formed film (eventually fibers thickness). However, the deviation of fibers width values at G=100μm from the other 2 G values is even more clear here. It was mentioned before that in PFMS if we get close enough to the wheel, we must be able to form ribbons with the width equal to the slit opening size. At G=100μm, we observe that the maximum fibers width is equal to 50μm which is the size of slit opening. However, its width mean value deviates from this prediction which is understandable because the system is modified toward fiber formation, and the film could have been broken to smaller width later during the process.

Going to Figure 6.25 to evaluate the shape of the fibers, we see that the roundest fibers with AR<2 belongs to G=200μm. This amount is slightly less at G=300μm.

However only 25% of fibers have AR<2 at G=100μm. Again, the closer we are to the wheel, the closer the system is to original planar flow melt-spinning, ideal for forming wide ribbons. Since we are not affecting film thickness significantly, one could expect to have larger AR at wider width values.

In the system we use for fabricating fibers we rely mostly on the wheel for cooling down and solidifying the melt. All the experiments are done in a closed chamber filled by Argon gas. The standard pressure used for all experiments as mentioned before is 400mbar. However, to see if this pressure helps at all with the fiber formation, the same experimental conditions were applied to make fibers at near vacuum, and higher pressure (800mbar). Vacuum was created using the rotary pump and the final pressure was less than 10^{-5}mbar.

Figure 6.26 shows the size distribution of fibers. The fibers thickness created at $P < 10^{-5}$mbar, have thickness 2 times higher than high pressures (400mbar and 800mbar). Chamber pressure in fact helps with the quenching rate of melt and we already discussed that the quenching rate can change ribbon/fiber thickness. The effect of chamber pressure is of course not as significant as wheel speed but it does affect the thickness as expected. The shift of mean value for fibers width is even higher for $P < 10^{-5}$mbar and is about 3 times more than P=400mbar and 800mbar. Thus, there are at least two things that can be interpreted here. At near vacuum ($P < 10^{-5}$mbar), it is still possible to form micro-fibers. So in case it is needed for a certain alloy, the process can run in vacuum (very low pressures) for microfibers fabrication. However, at the same time, it is clear that the chamber pressure does affect the process of solidification. The best size distribution for fibers width and thickness belongs to P=400mbar and there is no linearity between the chamber pressure and smaller fibers sizes. In figure 6.27 it is even more clear the deviation of fiber formation behavior at $P < 10^{-5}$mbar from the other pressures, specially for fibers width. The reason there is no linear decrease of size by applying more chamber pressure could be related to the gas turbulence which is created at higher chamber pressures inside the chamber. In a closed chamber with a wheel running at 60m/s speed, the more gas we fill, the more gas turbulence we create inside. This gas flow can eventually disturb the process itself. We observed so far that for forming fibers it is important to first wet the wheel surface and form the film, and later the film break down and dewetting the wheel. However, if by the gas turbulence we disturb the first step, which is the formation of thin film by destabilizing the conditions, we can no longer form fibers at some point. Due to device limitation the critical chamber pressure in which one can no longer form any fibers could not be shown here.

Figure 6.28 shows the effect of chamber pressure on the shape of the formed fibers. The roundest fibers(60% of fibers with AR<2) belong to P=400mbar. This amount at P=800mbar is slightly less but at $P < 10^{-5}$mbar, less than 20% of fibers have the round shape.

Chamber pressure for sure help cooling down the chamber, helping faster solidification of molten metal. When this gas is missing, it takes longer time for the alloy to solidify. Thus, they need to spend more time on the wheel to solidify.

Going through some of the possible parameters affecting the fiber formation, if we gather all the data related to the shape of fibers, we get Figure 6.29. Since we are dealing with a system starting from ribbon formation to the direction of micro-fibers, the closer the fibers cross-section AR to 1, the closer we are to the circular fiber shape. In this figure, it is counted that which percentage of fibers have a certain aspect ratio and width. If we need fibers with 1<AR<1.5, to have the maximum number of fibers with this such AR, we see that the red, orange and yellow regions (maximum counting) belong to the fibers with width<10μm. We already observed that the thickness of fibers is less affected by different parameters comparing to the width of fibers, and the range of thickness changes limits mainly up to 10μm (except some parameters such as wheel speed that can change this number to 20 μm). So if one could control the width of fibers and keep them under 10μm, one can expect to have the most circular fibers in this range.

For better predicting the thickness of fibers based on experimental parameters, Figure 6.30 was made. Based on the data at different experimental parameters, equation 6.1 for $Fe_{40}Ni_{40}B_{20}$ alloy was obtained. As one can expect, the thickness of fibers for a certain material with a certain liquid density, is proportional to the applied ejection pressure and slit size, and is inversely proportional to wheel speed. To understand this formula better, a better understanding of the whole parameters in this system is needed.

Going toward the direction of understanding system, we can start from the most important concept most melt-spinning parameters are connected to and that is " mass flow per unit area " (MFA). Thickness of the film created on the wheel is strictly connected to this mass flow per area. For defining the mass flow per unit area we have:

$$MFA = \frac{m}{A} \tag{7.1}$$

where m is the ejected mass and A is the area this mass is moving before creating the film. So the area this mass is flowing to is the area along the length of slit opening (1cm in our system) and the distance it moves on the wheel. For calculating A we have:

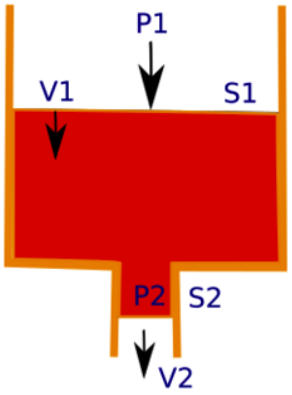

Figure 7.1.: Schematic drawing of applied pressures on melt inside the nozzle and slit opening

$$A = S \times x \tag{7.2}$$

where S is the length of the slit and x is the distance the ejected mass can move. To calculate the distance the mass can move, we can write with good approximation:

$$x = t \times V \tag{7.3}$$

where t is the ejection time and V is the wheel speed.

So now for MFA one can write:

$$MFA = \frac{m}{V \times t \times S} \tag{7.4}$$

The higher this mass flow, the thicker the film is created on the wheel. So we already can see why thickness is inversely proportional to wheel speed (V). The faster the wheel rotates, the lower the mass flow is which creates thinner films and fibers.

To connect other experimental parameters to MFA, let us assume a constant wheel speed(V), and ejection mass(m) (The slit length S is already constant and is 1cm). According to equation 7.4, MFA$\alpha\frac{1}{t}$. Ejection time t depends on several experimental parameters including the pressure applied on the melt. To be able to connect the ejection time to applied pressure (ΔP), one can write the following equations from Figure 7.1 which represents schematically the slit nozzle [55]
:

$$P_1 + \rho\frac{{V_1}^2}{2} = P_2 + \rho\frac{{V_2}^2}{2} + \rho gh \tag{7.5}$$

$$\rho{V_2}^2S_2 - \rho{V_1}^2S_1 = S_1P_1 - (S_2 - S_1)(P_1 + \rho\frac{{V_1}^2}{2}) - S_2P_2 \tag{7.6}$$

$$V1S1=V2S2 \tag{7.7}$$

where P_1,V_1, and S_1 are the applied pressure on the melt, the velocity as a consequence of this pressure, and the area this pressure is applied to (nozzle area). P_2,V_2, and S_2 are the pressure applied on the melt at the ejection point, the ejection speed, and the area this final pressure is applied to (at slit opening) and ρ is the melt liquid density. If we solve equations 7.5, 7.6 and 7.7, we will have:

$$V_2 = \sqrt{\frac{2\Delta P}{\rho[2-(\frac{S_2}{S_1})-(\frac{S_2}{S_1})^2]}} \tag{7.8}$$

.

Since $S_2 << S_1$, we can neglect S_2/S_1. In this case we have:

$$V_2 \approx \sqrt{\frac{\Delta P}{\rho}} \tag{7.9}$$

.

We already discussed that MFA$\propto \frac{1}{t}$, and t is $\propto \frac{1}{V_2}$. So one can say $MFA \propto \sqrt{\frac{\Delta P}{\rho}}$. Film (fiber) thickness itself is proportional to MFA. For a certain alloy with a constant liquid density ρ, then thickness $\propto \sqrt{\Delta P}$. This is in agreement from experimentally obtained equation 6.1.

From equation 7.9 we observed that the ejection speed (V_2) depends on the pressure differences(ΔP). The minimum pressure that need to be applied in order to eject the melt should overcome the surface tension of the liquid(γ). One can estimate the minimum pressure by [55]
:

$$P_{min} \approx \frac{4\gamma}{\delta} \tag{7.10}$$

where δ is the slit size and γ is the surface tension of the melt. Now we know why thickness depends on slit size. thickness $\propto \sqrt{\Delta P}$ and $P_{min} \propto \frac{1}{\delta}$; Thus, thickness is inversely proportional to slit size.

So far we discussed how mass flow affects the size of the fibers (thickness); however, it is not only the mass flow on the wheel that determines the size of fibers, but also the ability of the wheel to take away this mass and solidifies the film. That is where the wheel materials and speed comes into account. For solidifying the melt, we are counting on different factors: We expect the melt to wet the wheel surface, that being said it is important to have a wheel made possible for the alloy to wet its surface. The second factor is the heat transfer coefficient of the wheel. The higher this coefficient, the more heat can be transferred to the wheel from the melt. That is the reason a stainless steel wheel could not make fibers while the copper wheel could under the same conditions. The thermal conductivity coefficient of stainless steel used for that wheel is about 16.3 W/m.k which is smaller an order of magnitude than the copper wheel (385 W/m.k). The last parameter is the wheel speed which affect wetting, heat-transfer, and dewetting at the same time. Wheel speed was already discussed in this chapter and how it affects fibers sizes. It significantly changes the quenching rate of the melt and the quenching rate is inversely proportional to fibers thickness. The same principle is valid for ribbon thickness by melt-spinning.

7.2. Reproducibility and capability of melt spinning in fiber formation

In this project, the first aim was to develop a device capable of fabricating alloy microfibers. In this regard some parts of the device was modified and the rest of parameters were studied to reach the suitable parameters for fabricating microfibers. Since the device is going through an industrial path, it is important to make sure that the resulting fibers under certain experimental conditions have always the same range of sizes and shapes, and the second step is to evaluate the possibility of working with different class of materials within the same principle. So the same principle was applied to different classes of materials.

From Figure 6.31, it was very clear that repeating the same experimental conditions for $Fe_{40}Ni_{40}B_{20}$ alloy will result in fibers constant width and thickness values. Moving from $Fe_{40}Ni_{40}B_{20}$ alloy to other types of alloys and elements, we observed that in principle it is possible to make fibers using other materials. It was evident that the result of melt-spinning for amorphous-alloys such as vitrovac was the most promising one. For single metal elements such as Ag, Zn, Al or Cu produced fibers lack homogeneity in their shape and sizes. Ag, as a metal with low electrical resistivity is not a proper candidate to be melted by an induction method (copper coil) since Joule heating in induction method relies on metal electrical resistivity. Thus, serious problems would encounter melting it and keeping the melt temperature constant while ejection. Intermetallic alloys such as Ni_3Al and $Ni_3AlB_{0.4}$ had high melting points and one reason for their big fiber sizes could be due to low overheating. Corrosion of BN crucible was another problem which will not be discussed further here. Stainless steel fibers had the same problem similar to Ni_3Al since corrosion of BN crucible was an issue for them. Melt thermal fluctuation and slag formation were other technical problems prohibiting formation of homogeneous fibers. Even though many technical problems were involved with different class of materials, one could expect this problems to be fixed and optimized since the process worked for all of them in principle.

7.3. High speed camera movie

High speed camera movies taken from melt-ejection process using two different slit sizes was an important step toward understanding the process of fiber formation. Based on experimental results of using different slit sizes, we were aware of the deviation between saturation behavior of fibers width using the 25μm and 50μm. This difference in behavior can be explained by their different nature of film formation. Based on Figure 6.37, when we have 50μm slit size, it forms a melt-puddle of about 3mm. The puddle is stationary with slight disruption of some droplets ejecting out, so one should expect longer fibers forming here comparing to 25μm slit size, and this prediction matches real results. Going to smaller slit size: 25μm slit size, no melt-puddle forms at all. In fact, there are individual droplets wetting wheel surface in the process. Each droplet is ejected with a constant time delay sequentially. Some of the droplets cannot wet the surface because their surface tension is very high and if upon falling on the wheel with the high centrifugal force applied on them, wetting the wheel is not favorable , and they might only be accelerated and leave the wheel without forming any film. Besides, the lack of stationary puddle means fibers should have more or less a certain range of length if we assume all droplets have the same range of diameters. In this movie, these droplets are about 0.6 mm. If this droplets wets the wheel surface and forms the thin film, the equivalent volume of this film can be easily calculated:

$$\frac{4}{3}\pi r^3 = t \times w \times l \tag{7.11}$$

where t is film thickness, w is film width, and l is the length of this film. The thickness of the film is equal to the thickness of fibers, so the mean value of 5μm can be assumed for the film thickness. The length of final fibers are also constant and is in the range of 200mm. Now we are able to calculate the width of the formed film. Putting these values in equation 7.11, the film width must be around 0.9 mm. From SEM pictures in Figure 6.36 we observed that fibers are possibly formed after breaking down the film to smaller widths. If we follow this assumption, it means that each droplet wetting the wheel and forming a thin film of 0.9 mm wide, must break down later to around 60 fibers. (We divided total width of film to the mean width of fibers formed afterwards). Again, this matches experimental result during melt-ejection.

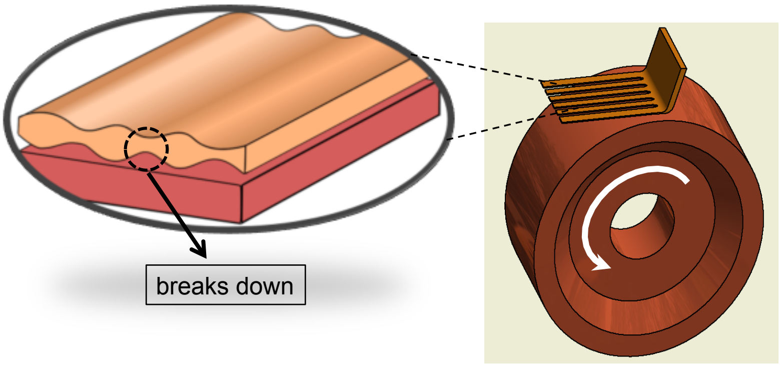

Figure 7.2.: Plausible fiber formation mechanism. The film created on rotating wheel breaking down to smaller widths at node points.

7.4. Possible fiber formation mechanism

Based on all the results and discussions, the process of fiber formation by melt-spinning can be explained in 2 steps: i) metal melt wetting the rotating wheel and film formation ii) spontaneous breaking of the film to form fibers. The first step is very clear and different parameters e.g. wheel speed, wheel material affect this film formation. The exact mechanism of film breakage is however not known. One plausible explanation is an approach similar to Rayleigh instability and formation of droplets out of a continuous liquid flow. Figure 7.2 shows schematically what we think happens to the formed film. Due to enormous centrifugal force applied on the film (and high wheel rotation frequency), one could expect to have non-ideal wetting of the film on the wheel surface. If this film becomes thiner at some node points, film will eventually break to smaller widths. This is in agreement with all the experimental results we had. In high speed camera movie section we observed that even a single droplet can contribute to a film 0.9 mm wide, and solidifies in forms of fibers with 5μm mean width size. Some SEM figures from failed products when the ribbon breakage to smaller fibers were not fully successful are aligned with this explanation as well. Of course some other parameters can influence and enhance this film breakage such as wheel surface roughness. More precise fiber formation mechanism and modeling of course could be done in further studies.

Part II.

Stainless Steel Microfibers

8. Introduction to Stainless Steel

8.1. Steel: Fe-C phase diagram

Steel is usually defined as an alloy of Iron and Carbon for 0.15-2.4wt%C. A typical phase diagram of steel is shown in Figure 8.1[60] for carbons up to 7% atom between 600°C and 1600°C. Each temperature and composition contributes to a specific thermodynamically stable phase. The stable phase of iron below about 900°C (α) and above about 1400°C (δ) is called ferrite which has a body centered cubic (bcc) crystal structure. The thermodynamically stable phase of iron between 900°C and 1400°C is austenite (γ) with faced center cubic (fcc) crystal structure[61]. Steel is hard and durable comparing to pure Iron even with slight addition of carbon atoms because carbon atoms while solving in Fe-fcc or Fe-bcc structure rearrange themselves within interstitial sites of iron lattice. Consequently, iron atoms have smaller range of movement ability. Thus, carbons cause a glue effect, strengthening the iron against deformation and fracture. The solubility of carbon in austenite is higher comparing to ferrite due to higher number of available interstitial sites. If we cool slowly austenite, and it reaches its lower thermodynamically stable ferrite phase, the excess C content needs to be precipitated in form of carbide or graphite.[62].

8.2. Hardening mechanisms of steels

There are different mechanisms which can be used in hardening steel. In this section we shortly describe the most common steel hardening mechanisms including strain hardening, grain size hardening and precipitation hardening.

8.2.1. Strain hardening

Strain hardening is a common method for steel hardening. One reason for that is the high melting temperature of steel. Strain hardening or in other words "work-hardening" is based on introducing dislocations into crystallites of steel so much that while interacting with each other, they get pinned or entangled with each other. This way, the dislocation movement which is the most dominant deformation mechanism at low-temperatures is interrupted. Consequently it harden the material. Cold work is commonly used for high melting point alloys at relatively low temperatures when T$\leq 0.5T_m$. At T$\leq 0.5T_m$, atoms cannot rearrange

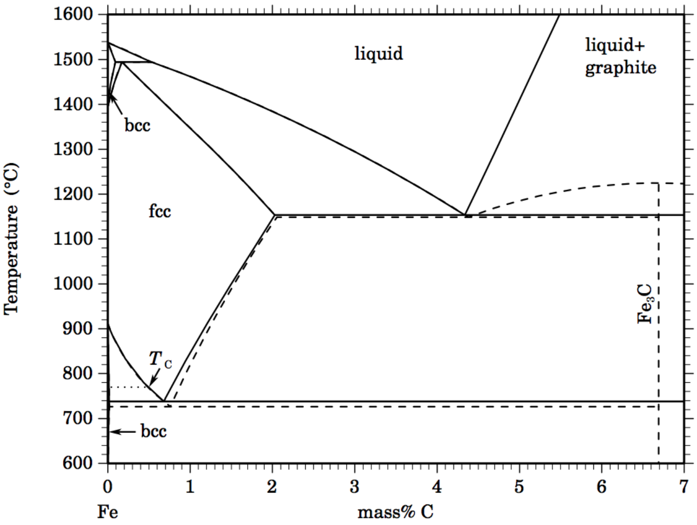

Figure 8.1.: Binary Fe-C phase diagram between 600°C and 1600°C for C content up to 7% atom[60].

themselves thus the effect remains. In contrast, hot work is done above the recrystallization temperature of alloys. Hot working is able to induce larger deformations comparing to cold work but it causes in many alloys surface oxidation. Thus, is not as popular as cold work[63, 64].

8.2.2. Grain size hardening

Grain size as one of the parameters that affects steel microstructure, contributes on changing its bulk mechanical properties including hardness. To evaluate the size of grains, optical microscopy is commonly used and in some cases XRD (peak broadening for nanocrystals). By decreasing the grain size, it is possible to harden and strengthen alloys and metals. Of course, smaller grains are able to pack closer and denser together. Thus, by applying an external stress it is more difficult to move and reposition atoms[62, 65, 66]. One can control the grain size by controlling the cooling curve of alloy. The faster the cooling process, the less time crystals have to grow, leading to smaller grain size. On the contrary, annealing an alloy (in the grain growth temperature range) leads to larger grains. The famous Hall-Petch equation for expected increase in strength of material by decreasing the grain size is given at equation 8.1, [67, 68, 69]:

$$\sigma_y = \sigma_0 + Kd^{-1} \tag{8.1}$$

Where σ_0 is the friction stress in the absence of grain boundaries, k is a constant and d is the grain size. According to equation 8.1, the yield strength increases when grain size becomes smaller because the smaller the grains become, the more they pile up, fewer dislocations form in this condition[70, 71]. It is however shown that Hall-Petch effect is valid until a critical grain size. This critical grain size is usually below 10nm because in very small grains, grains are unable to support dislocation pile-ups. Thus, in this regime, yield strength tend to decrease. This effect is known as the inverse Hall-Petch effect (IHPE)[72, 73, 74].

8.2.3. Precipitation hardening

One example of precipitation hardening in steel is when steel goes to high temperatures, and it forms large iron carbide crystallites. These crystallites make the slip deformation easier and cause softening of steel. If the steel stays longer at elevated temperature, it can interrupt Fe-Fe or Fe-C bonds in pearlite or bainite allowing cementite (Fe_3C) to agglomerate into spheres and later get dispersed in the ferritic matrix. When these spherical cementite crystallites disperse homogeneously within the ferritic microstructure, they make the slip between grains harder leading to hardening of steel. This method is common in many alloys including Al-Cu alloys. The heating process can be done using high energy sources such as laser for local surface hardening which eventually make them more resistant to wears as well. This principle can be used in many alloys. Since this method is based on ageing material, is also known as "age-hardening"[62, 75]. So, in principle this mechanism can be done by rapid cooling the alloy. The interaction mechanisms in which the precipitate could impede the dislocation motions could be through chemical strengthening, stacking fault strengthening, modulus hardening, coherency hardening, order strengthening[76, 77, 78].

8.3. Steel TTT diagram

Talking about rapid quenching steel and precipitating another phase, if we cool austenitic steel with a colling rate high enough to suppress ferrite or bainite formation, we can have a transformation to martensite structure. Martensite crystals for their needle-shape morphology increase the hardness of steel. The cooling program must be high enough not to reach the nose of steel TTT diagram. The tangent line to avoid the nose is considered as critical cooling rate. Figure 8.2 shows the TTT diagram of different grades of stainless steels[79].

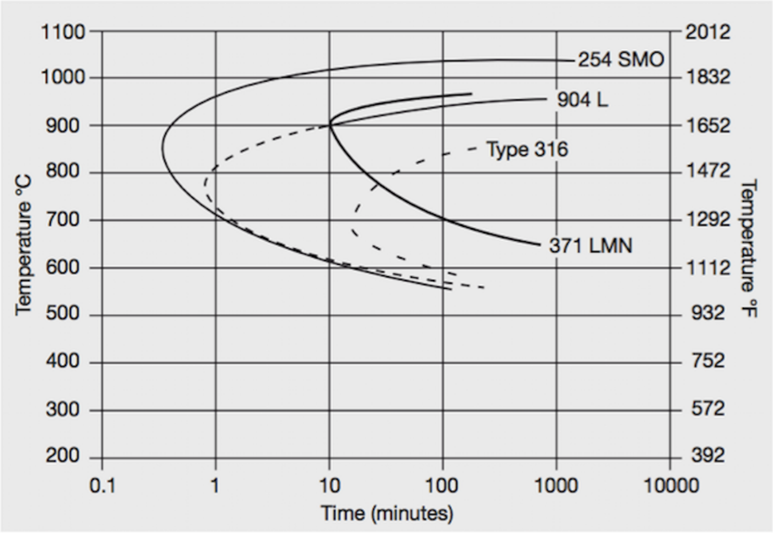

Figure 8.2.: TTT diagram for several commercial austenitic stainless steels with different molybdenum and nitrogen contents[79].

8.4. Stainless steel

Stainless steel (SS), has a wide range of applications from kitchenware to medical equipments or even nuclear reactor components because of its high corrosion resistance resulting from the passivation layer it forms[80, 81]. It is a remarkable achievement of modern metallurgy and is an alloy with a minimum 12 weight percent of chromium[82]. Chromium is added to protect steel from rusting and corroding. Cr addition is used to achieve high corrosion and oxidation resistance; besides it increases steel strength [83]. Other common alloying elements includes Nickel, Molybdenum, Silicon, and Manganese. The influence of these alloying elements on phase structure of steel were studied intensively, e.g. by Schaeffler. The Schaeffler diagram is important because it evaluates which structure will be obtained after rapid cooling from 1050°C to room temperature based on the proportion of alloying elements. It is evident from Figure 8.3[84] that Ni is an austenite stabilizer while Cr stabilizes ferrite. Other elements which stabilize ferrite are Ti, Mo, Si, and Nb. Similar to Cr, other elements besides Ni stabilizing austenite are C, and Mn. In equation 8.2 and 8.3, it is shown how to calculate the equivalent for %Cr and %Ni content[85, 86]. The red dash-lines in Figure 8.3 show the equivalent Ni and Cr content in the stainless steel used in this study. However, this diagram does not allow us to determine the composition and volume of the carbide phase formation.

$$\%Ni = \%Ni + \%Co + 0.5\%Mn + 0.3\%Cu + 25\%N + 30\%C \tag{8.2}$$

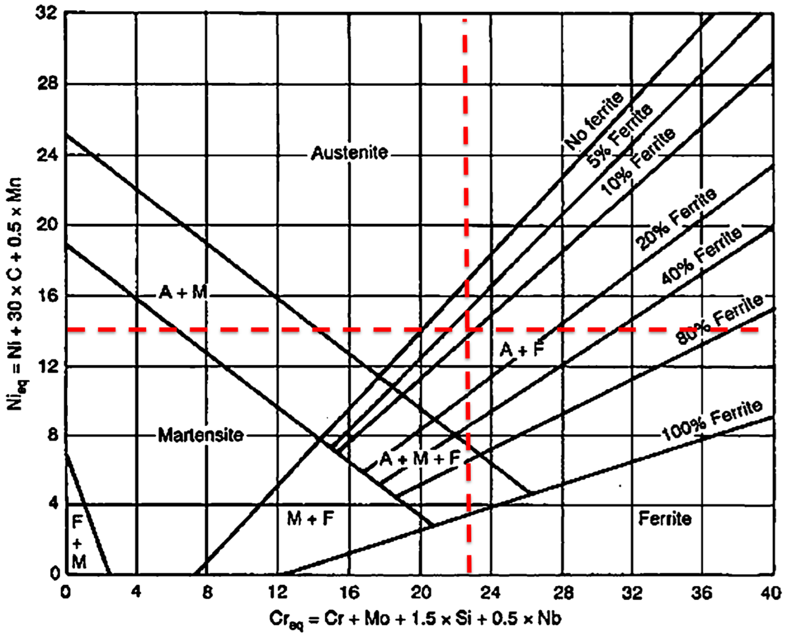

Figure 8.3.: Schaeffler diagram predicting the microstructure based on equivalent Cr% and Ni%. The equivalent Cr% and Ni% of the stainless steel used in this study is marked by dash lines[84].

$$\%Cr = \%Cr + 2\%Si + 1.5\%Mo + 5\%V + 5.5\%Al + 1.75\%Nb + 1.5\%Ti + 0.75\%W \tag{8.3}$$

Among the remarkable properties of stainless steel one can notice their high specific strength, high stiffness, high fracture toughness and corrosion resistance. These properties make stainless steel to compete with lighter elements such as Aluminum or Titanium even for applications such as aerospace. The next generation of stainless steel could be improved strength and corrosion stainless steels. Several strategies could be used for such improvements e.g. carburizing, alloying, thermochemical processing and more recently proved, grain refinement. Studies show that grain refinement can improve greatly stainless steel strength and corrosion resistance[87, 88, 89, 80]. However, many studies showed that although the strength improves significantly through grain refinement and nanocrystallization, it provides very poor plastic elongation in stainless steel comparing to coarse-grain stainless steel[90, 91]. Such problem arises from not ideal processing techniques of nanocrystallization such as mechanical milling/alloying, crystallization from amorphous materials or sever plastic deformation. These techniques lead to not fully homogeneously distributed grain size and samples with residual internal stress[92, 93].

It was previously believed that grain refinement and nanocrystallization must lead to low corrosion resistance because of their high free energy. However, in recent years, many corrosion-resistance tests were contradictory to each other, showing different corrosion behaviors. The routs of different behaviors might be due ot different preparation techniques if we exclude the effect of type of electrolyte. Different precessing techniques lead to not only different grain size, but also to different level of homogeneity in grain size distribution, chemical composition, dislocation density and other parameters affecting the corrosion behavior[80, 94]. Though, one cannot conclude how grain size directly affect the corrosion behavior without considering other parameters.

Stainless steels are divided in four main groups based on their microstructure: austenitic, ferritic, martensitic, and duplex. To cast each group, the composition and heating/cooling program differs. Each main group offers its own mechanical, magnetic, corrosion properties[95].

8.4.1. Austenitic stainless steel

Austenitic stainless steel grades contain a minimum 16 wt% of chromium and they can be classified to series 200 and 300. The 200 series are Fe-Cr-Ni-Mn-N alloys with minimum of 2 wt% Mn, while 300 series are based on Fe-Cr-Ni with maximum 2 wt% Mn according to AISI[86]. The grades 321 and 347 were developed by adding Ti, V, and Nb to Fe-Cr-Ni steels. Mo is often added to increase pitting resistance. Cu and V are often added to strengthen austenitic steels[96]. It was shown e.g. for Super304H austenitic grade before that by adding B, V, Mo, Cu, and W one can increase steel strength significantly[97]. The new austenitic heat-resistant steels such as NF709 and SAVE25 are developed by replacing part of Ni with N[98, 99].

In this project, different austenitic grades of 300 series are used. They are the most commonly used stainless steel grades and are widely used in applications such as transport equipments, surgical equipments, kitchen utensils, jeweleries, and implants[100].

9. Materials and Methods

In this chapter the methods and materials used specifically to fabricate and analyze stainless steel (SS316-Ti) microfibers is described. In case of regular materials characterization techniques and text book material, the description is avoided.

9.1. Fabricating micro-fibers

Fibers were fabricated by melt-spinning from 316-Ti austenitic stainless steel. The exact composition of this steels is presented in supplementary materials. This alloys was casted by materials preparation department of Max Planck Institute for Intelligent Systems in form of metal rodes. Experimental Conditions for fabricating stainless steel fibers by melt-spinning are summarized in Table 9.1.

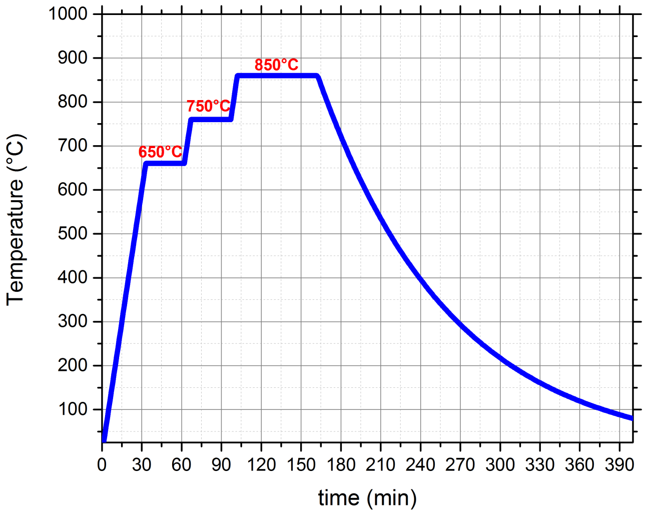

Figure 9.1.: Heat treatment program for SS316-Ti microfibers. Heating rate is 20°C/min and after holding time, they are furnace cooled. The atmosphere is Argon.

Table 9.1.: SS316-Ti fabrication experimental parameters

Wheel type	V (m/s)	δ (μm)	G (μm)	P (mbar)	ΔP (mbar)	$T_{ejection}$ (°C)
Flat Cu wheel	60	50	200	400	1200	1400

9.2. Heat treatment

Some SS316-Ti microfibers were further heat treated by reaching austenisation temperature step by step. The intermediate steps were 650°C and 750°C , holding 30min at each step. This holding time for the final step was 1h.The heating/cooling program is shown in Figure 9.1. The heating rate was 20°C/min and the cooling was furnace-cooled in an Argon atmosphere.

9.3. XRD and DTA measurements

Differential thermal analysis (DTA) experiments were carried out on a thermal analyzer NETZSCH STA409C (NETZSCH Geraetebau GmbH, Selb) in a constant flow of 50 ml$\cdot min^{-1}$ argon (>99.999%, Westfalen AG) with a heating rate of 10 K$\cdot min^{-1}$ in aluminum oxide crucibles. Before the measurements the thermal analyzer was flushed 3 times with argon, followed by a conditioning period at 40°C for 30 min with extended flushing. The samples were heated to 800°C and subsequently cooled down after reaching the maximum temperature. During the measurements a NETZSCH oxygen trap system (OTS) was used, allowing for residual oxygen contents below 1 ppm O_2. The systems starts to work at about 300°C and reaches maximum efficiency above 500°C.For powder X-ray diffraction measurements a $\Theta/2\Theta$ -system was used. The instrument is using filtered Co-Kα^1 and Co-Kα^2 radiation and Bragg-Brentano-geometry. The sample were directly used in forms of fiber.

9.4. TEM measurements

The fibers were prepared for cross-sectional imaging by a FIB (SCIOS-FEI dual beam FIB/SEM focused ion beam) with a NiCol electron column and a gallium liquid metal field ionization source. The Ga ions are used to mill out material and the speed of milling is controlled by current. The SCIOS dual beam is also equipped with a gas injection systems (GIS). In this case Pt (in an organometallic gas form - (methyl-cyclopentadienyl) trimethyl platinum) is used as deposited material for protecting the sample and for gluing over the transport-preparation process. Prior to the cross sectioning, a layer of 200nm + 1.5μm of Pt was deposited on top of the sample in order to protect the area of interest during milling with the ion beam. This layer will be referred as “protective layer” hereafter. A lamella was cut out of the thin film along a cross section and attached to a micromanipulator needle, and then transferred onto a Cu TEM grid. In order for the lamella to be electron transparent for the TEM imaging a thinning step was performed at different currents of the ion beam (from 1nA to 100pA). A final cleaning of the lamella was necessary, in order to eliminate the Ga ions deposited on the sample during milling. The cleaning steps where performed at 5kV and 48pA followed by a lower voltage of 2kV and 27pA. A Philips CM200-FEG transmission electron microscope (TEM) was used at 200kV for bright field imaging as well as for selected area diffraction patterns.

9.5. Nanoindentation measurements

Fibers were glued by two-component super glue to a plastic sample holder. After drying, their cross section was prepared by embedding them on Epofix resin and hardener. Samples were grinded by 1200 and 2400 and 4000 SiC Sand papers and polished further by 1μm diamond suspension, and Alumina powder suspension. Cleaning was done using Isopropanol followed by fast-drying of a hair dryer.

Nanoindentation test was done using the Nanoindenter XP software. The continuous stiffness method was used for the measurements. The indenter tip was cube-corner for SS316-Ti, otherwise stated (in supplementary materials, there are some tests done by Berkovich tip). The surface approach velocity was 30nm/s, and the surface approach distance was fixed to 3000nm. The harmonic displacement was 2nm with 45Hz frequency. The strain rate was 0.05 1/s. The depth limit of 250nm indentation was selected for SS316-Ti fibers. The Poisson ratio was considered in the range of 0.28 to 0.30.

10. Experimental Results

SS316-Ti microfibers shape and size were characterized by SEM. The SEM pictures from their top view and their cross sections view are shown in Figure 10.1a and Figure 10.1b respectively . Figure 10.1a from the top view, shows fibers with diverse shape and sizes. The smaller fibers are more circular while the larger fibers have ribbon shapes. Some fibers have irregular border shapes. The widths of some fibers are not always constant along the length of the fibers. Figure 10.1b shows that the cross section of these fibers are almost rectangular instead of circular.

Size distribution of fibers (width and thickness from cross section view) is presented in Figure 10.2. This diagram shows that the average thickness and width of fibers are 4μm and 14μm respectively. It was already shown in Figure 10.1a and Figure 10.1b that the thickness is expected to have more constant values. Here we see the distribution of thickness values is narrower than the width values. The fibers were further analyzed by X-ray diffraction (XRD) regarding their crystalinity. Figure 10.3 shows the diffraction pattern of quenched fibers and the starting material before making fibers by melt-spinning. The starting material, as expected, shows a mixture of bcc and fcc phases (ferrite and austenite). The fibers however, show a diffusive peak between $2\theta = 40° - 60°$. In fact no crystalline peak could be detected from the fibers after melt-spinning.

To better understand the crystallization behavior of SS316-Ti, in-situ XRD of the fibers were carried out between 400°C to 800°C in steps of 100°C. The XRD at

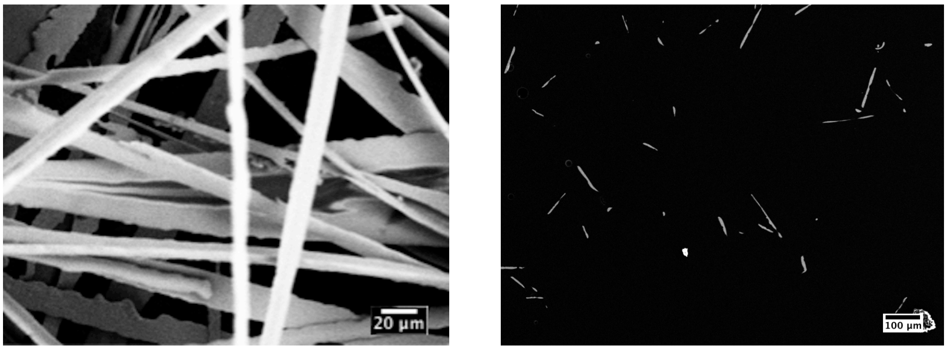

(a) full-view **(b)** cross-section view

Figure 10.1.: SEM pictures of SS316-Ti microfibers from top and cross-section view. The cross-section is rectangular in stead of circular

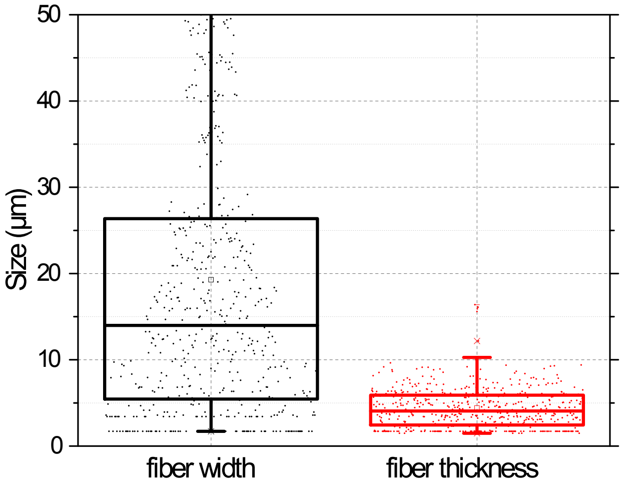

Figure 10.2.: Size distribution of SS316-Ti fibers (width and thickness). The mean value of thickness is around 4μm while the mean value of their width is almost 3 times larger, around 13.9μm

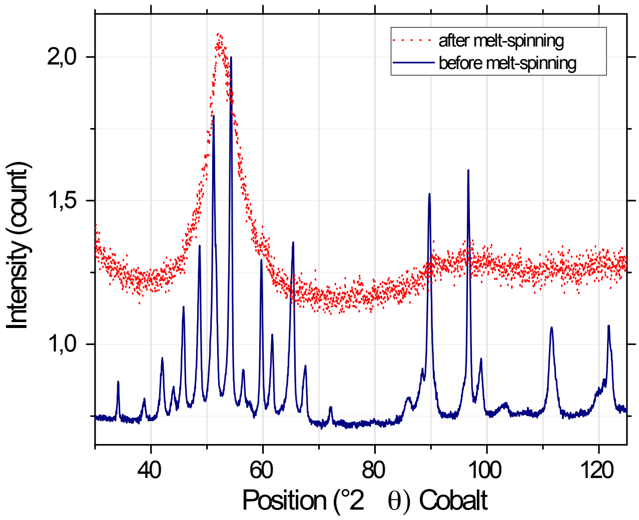

Figure 10.3.: XRD from SS316-Ti before and after melt-spinning process. The XRD pattern of the alloy before melt spinning shows the presence of bcc and fcc phases. After the melt spinning, a very broad diffusive peak is observed between $2\theta = 40° - 60°$.

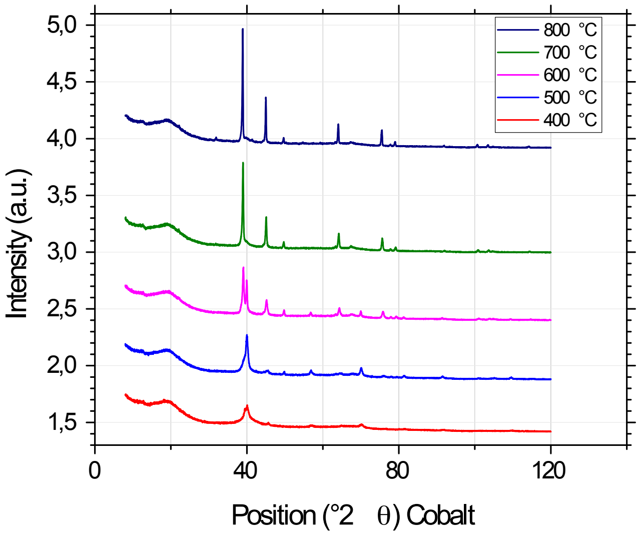

Figure 10.4.: In-situ XRD of SS316-Ti at different temperatures. Each diffraction pattern is obtained at room temperature after heating fibers and keeping them at proposed temperature for 1 hour. The evolution of crystalization at different temperatures is clearly visible.

room temperature after holding at each temperature steps is obtained. The result is shown in Figure 10.4. By increasing the temperature, the peaks get sharper.

For better estimation of glass transition temperature, DTA analysis from the same fibers was carried out and is shown in Figure 10.5. The red line indicates the heating process and the cooling curve is depicted by blue line. If we follow the heating curve, at around 437°C, we see a turning point followed by a peak at around 573.6°C. To make it more clear to find these points, the first derivative of heating curve is depicted in black. This derivative curve shows that the transition at around 437°C has to have a second-order nature, while the transition at 573.6°C is a first-order transition. The bumpy shape of cooling curve at around 770°C is due to crucible instabilities and should not be considered as a source of change in the material.

The fibers microstructure was further investigated by TEM. After thinning the fibers by focused ion beam (FIB), the TEM imaging and diffraction was done on the fibers cross-section area. Figure 10.6 shows a TEM bright field image of SS316-Ti cross section. No crystals can be seen in this region, and the diffraction pattern shows diffusive and broad ring pattern, which shows no preferred crystalline orientation.

The same analysis was made on SS316-Ti fibers after subsequent heat-treatment program. Figure 10.7-a shows the bright field image of its cross-section. There

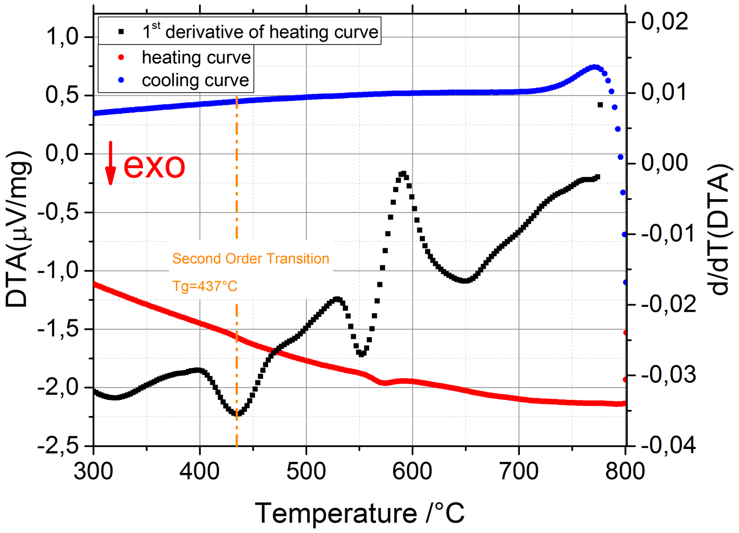

Figure 10.5.: DTA pattern obtained from amorphous 316-Ti stainless steel. At 437.8°C a weak second order exothermal signal was detected as an indication of glass transition temperature. At 573°C a first order exothermal signal was detected.

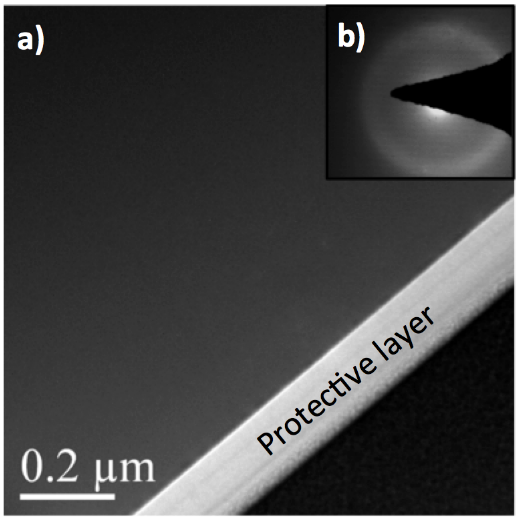

Figure 10.6.: a) TEM bright field image from the cross section area of as-quenched SS316-Ti after melt-spinning. No crystals can be seen in the cross section b) the diffraction pattern from this area shows a broad diffusive ring with no preferred crystalline orientation.

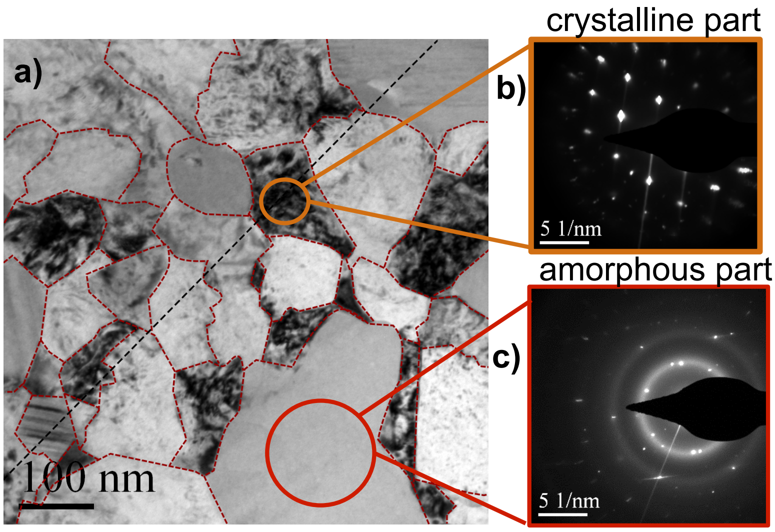

Figure 10.7.: a) TEM bright field image from SS316-Ti fibers after heat treatment. Several regions and crystals are visible with the average grain size of 84nm. Two distinctive areas is observed. b) the diffraction pattern from darker grains shows a crystalline structure c) the lighter grains shows a diffusive ring with presence of some diffracted points.

are numbers of grains visible in this picture which vary a lot in terms of size. To estimate its average size a line is made as a diagonal and the average grain size is estimated by dividing their size to the number of grains along the line. The result is about 84nm. The diffraction pattern at different grains was obtained and here it is shown two of them on Figures 10.7-b and Figures 10.7-c . The diffraction patterns are significantly different from each other on these two grains. Figures 10.7-b exhibit the crystalline structure while Figures 10.7-c exhibit a diffusive ring similar to previous as-quenched fibers, this time with slight diffracted points within the diffraction ring.

Since the diffraction ring of some grains of heat-treated fibers (Figures 10.7-c) were similar to as-quenched fibers in Figure 10.6, to compare their difference better, the intensity profile of diffusive rings are compared in Figure 10.8. It is evident that the diffusive ring after heat-treatment is much sharper and it shows a peak in the intensity profile while the previous as-quenched diffraction ring hardly shows any peak in its intensity profile.

Of course, what could be seen in diffraction pattern of some heat-treated fibers was the diffraction points on the ring itself which was not observed for as-quenched fibers. To observe the image of such diffraction point, the dark field image is obtained from each diffusive and diffraction points. These dark field TEM images are shown in Figure 10.9. In fact, Figure 10.9 shows the bright field image taken from heat-treated SS316-Ti cross-section, the diffraction pattern obtained from this

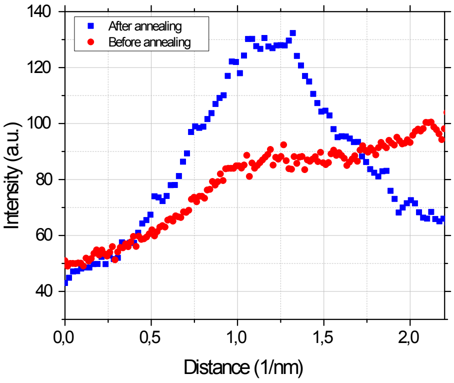

Figure 10.8.: Intensity profile of diffusive ring before and after heat-treatment in SS316-Ti fibers cross-section.

area, and the dark field images of each area shown in the diffraction pattern. The diffracted pints belong to grains with parallel lines on their grains. The diffusive ring however belongs to grains with no such structural lines.

Going to higher magnification on the grains with diffusive diffraction ring, several more information can be extracted. This higher magnification image is shown in Figure 10.10. The crystalline lattices with lattice parameter of 1.64°A is observed. Some regions with lines are one order of magnitude bigger than lattice parameter. In the area when two lattices meet each other, we can see clearly a stack fault.

Mechanical properties of as-quenched and heat-treated SS316-Ti were investigated using nanoindentation. Figure 10.11 shows the Elastic Modulus and Hardness values for different amorphous alloys and our amorphous SS316-Ti and heat-treated SS316-Ti. For comparison reason, the traditional SS316-Ti values (bulk-sample)

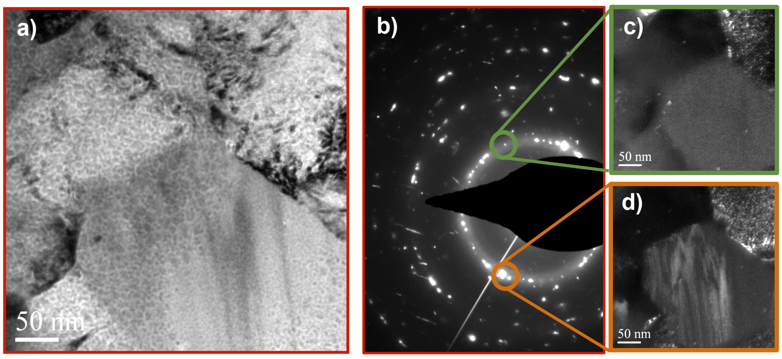

Figure 10.9.: a) Bright field TEM image from heat treated SS316-Ti cross-section b) Diffraction pattern made on lighter grains of heat-treated SS316-Ti. c) Dark field TEM image of diffusive part of the ring. d)Dark field TEM image of diffracted points of the ring.

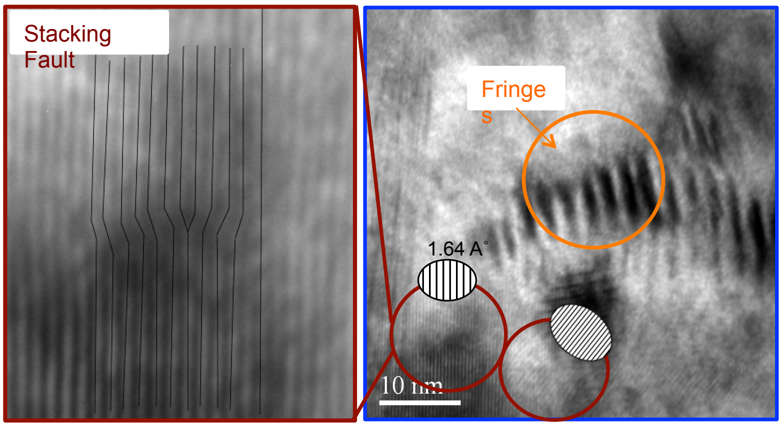

Figure 10.10.: TEM-bright field image from SS316-Ti light grain at higher magnification. the crystalline lattice with a lattice constant of 1.64°A is visible. Where two lattices reach each other, the dislocation is formed. There are areas indicated by an arrow, showing a moire fringe structure.

are also added. The exact values of all these bulk metallic glasses samples and their references is presented in Table 20.4 in supplementary materials. As it can be seen, Hardness vs Elastic Modulus follows a line for bulk metallic glasses and our as-quenched SS316-Ti stays close to this line. However, heat-treated SS316-Ti has higher hardness than other amorphous alloys with the same elastic modulus. In fact, if it wanted to stay within the line, it should have had less than 12 GPa hardness. The traditional bulk crystalline SS316-Ti has much lower hardness than any amorphous alloy and heat-treated SS316-Ti (7-times less than the heat-treated SS316-Ti).

The effect of grain size on hardness of heat-treated SS316-Ti and other SS304 alloys with different grain sizes are shown in Figure 10.12, these values are obtained from F.K.Yan et al[101]. The heat-treated SS316-Ti does not stay close to the predicted linear line (Hall-Petch formula) in this figure and has twice higher hardness value (14GPa).

Further comparison between the as-quenched and heat-treated SS316-Ti was made by wear-release test. This test makes a comparison between releasing ions into the solution of study (BSF), and this gives a source of comparison for their resistance against wear production. The concentration of ions in the solution was measured by ICP-OES. Figure 10.13 shows the release of main ions (Fe,Ni,Cr) from as-quenched and heat-treated SS316-Ti fibers into BSF solution. For releasing Cr and Ni, the range of ion-release is quiet similar in case of as-quenched and heat-treated SS316-Ti, although this release is slightly higher in case of as-quenched fibers. Another trend that can be seen in this figure, is the increase of ion-release by time in all cases. The slope of this increase decreases by time though. In

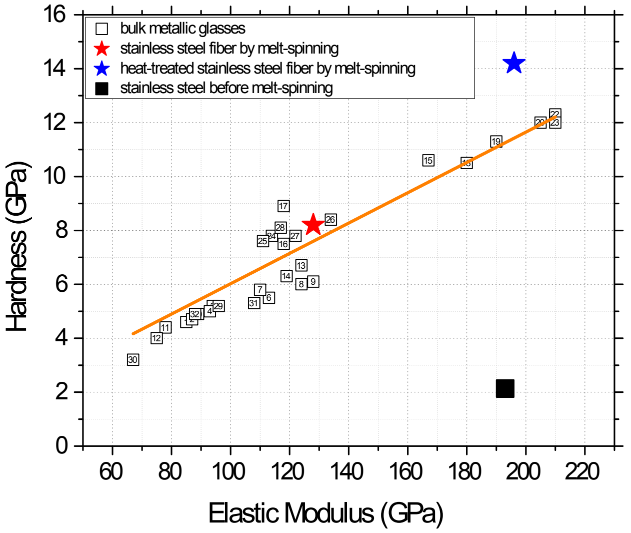

Figure 10.11.: Hardness vs Elastic Modulus for different amorphous alloys, conventional SS316-Ti, and our amorphous and heat-treated SS316-Ti. The complete value and composition for each alloy is presented in Table 1. All the amorphous alloys, including SS316-Ti follow a line and the heat-treated SS316-Ti has higher hardness than all. The conventional crystalline SS316-Ti has lower hardness than any other amorphous alloys.

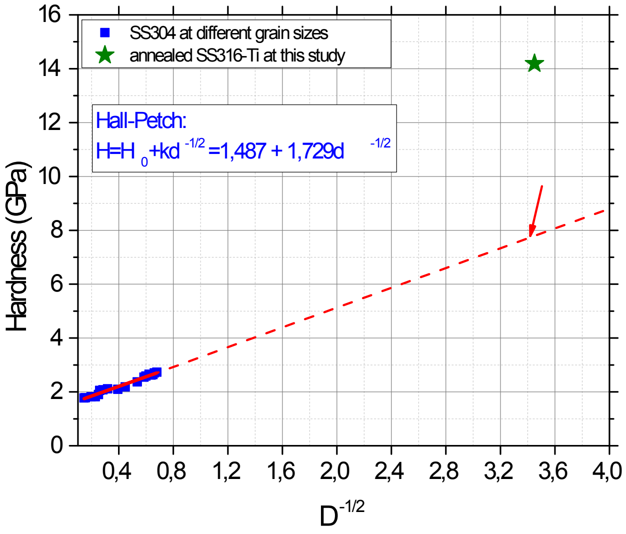

Figure 10.12.: Stainless steel hardness vs its grain size. Hardness has inversely a linear relation with square root of grain size of SS304. The heat treated SS316-Ti has twice the value of its predicted hardness on the line. Data points from 304 stainless steel are taken from [101].

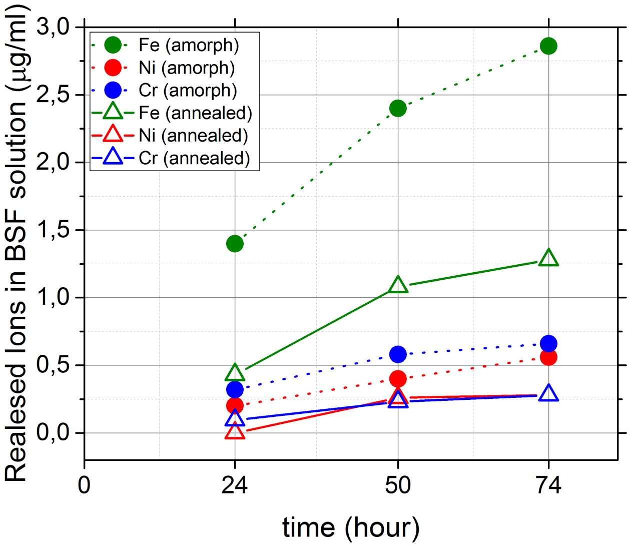

Figure 10.13.: ICP-OES measurements of released ions (Fe,Ni,Cr) from as-quenched and heat-treated SS316-Ti fibers into BSF saline solution. Measurements were done after 24,50, and 74h of keeping fibers in BSF solution. As-quenched fibers in general release more ions than heat-treated fibers. The ion release increase by time in all cases.

case of Fe-ions, there is a significant difference between the as-quenched and heat-treated samples. This difference in the beginning is three times higher release for as-quenched sample.

11. Discussion

The SS316-Ti fibers obtained by melt-spinning have rectangular cross-sections instead of round circular cross sections. This is due to the nature of the fabrication process (planar flow melt-spinning). As discussed in the previous chapters, to have round fibers one must control the fibers width values to be under 10μm. Here, the mean width values is about 14μm leading to rectangular cross-sections. As expected, the thickness of the fibers has more narrow size distribution comparing to their width size distribution because ejecting the melt with constant experimental parameters, creates a film of a certain thickness that later breaks down to ribbons and fibers with smaller widths. The experimental control over this breaking down is much less than the thickness of the created film. Consequently, we fabricate fibers (micro-ribbons) with more diverse width in their cross-section.

The broad XRD peak from the fibers is wider than what can be considered as a crystalline peak. Even in case of nanocrystalization which leads to peak broadening, the peak can not be as broad as 20° wide. The diffusive peak however, can provide information about the short-range atomic ordering within material. In fact, the similar peak is observed for most Fe-based glassy metals. This is however the first time a commercial stainless steel grade can form an amorphous structure within bulk region without adequate refractory element additives (amorphous stainless steel thin film is also reported before by Wang et al[102], [103]). Based on Fe-C phase diagram one should expect to have austenite fcc phase with traces of bcc phase after cooling down to room temperature. Following CCT diagrams of steel, one should also expect martensite formation in high quenching rates. However, based on the XRD results, we understand that the quenching rate must have been high enough to suppress crystallization in the first place during quenching from liquidus temperature, and if austenite could not form in the first place, it can no longer transform to martensite. We can estimate cooling rate by:

$$\frac{dT}{dt} = \frac{(T_{ejection} - T_g)\kappa}{XC_p\rho} \tag{11.1}$$

where κ is thermal conductivity, X is film(fiber) thickness, ρ is melt liquid density, and C_p is alloy specific heat capacity. If we put values of Table 11.1, we will have: dT/dt=2.72 × 10^8 °C/s. This cooling rate is so high that it prohibits any crystal formation. Lubrosky et al[57], computed the cooling rate of alloy $Fe_{40}Ni_{40}P_{14}B_6$ as a function of its section thickness for splat quenching and for chill block melt

Table 11.1.: Experimentally obtained values for SS316-Ti fibers

$T_{ejection}$(°C)	T_g(°C)	ρ ($g.cm^{-3}$)	C_p ($J.Kg^{-1}.K^{-1}$)	κ ($W.m^{-1}.K^{-1}$)	X (μm)
1450	437	7.75	502.416	16.3	4

spinning and showed that when the section thickness of this alloy reaches the order of 1μm, the cooling rate can have the same order of magnitude as we have in our system.(dT/dt=2.72 × 10^8 °C/s).

In-situ analysis of SS316-Ti shows that crystalization of amorphous fibers starts about 400°C, and it evolves up to austenization temperature (800°C). Even though, this data gives us an approximation of when the crsytalization occurs, more accurate data about glass transition temperature can be extracted from DTA analysis in Figure 10.5. The first second order exothermic transition is observed at 437°C as an indication of glass transition temperature. The second thermal transition was observed at 573°C which can be due to phase transformation within alloy contributing to higher temperature stable phases.

Since stainless steel was never reported as a potential alloy for forming glassy metals, its glass forming ability is estimated using the reduced glass transition temperature (T_{rg}) approach. As shown by Z.P.Lu et al[12], there is a correlation between glass forming ability with its reduce glass transition temperature. So, T_{rg}= T_g/T_l=437/1380=0.31. This value is in the spectrum of alloys which are not originally designed to form glassy structures due to lack of deep eutectics. The highest known values of T_{rg} for metallic alloys are in the range of 0.66-0.69 [13], [14]. It was shown before in Figure 4.3 that for each T_{rg}, there exist a critical cooling rate for forming glassy structure. Following this figure, for our alloy with $Trg = 0.3$, this critical cooling rate lies in the range of 10^8 °C/s. Of course, such high cooling rate is not accessible through most conventional fabrication methods. It was also shown in Figure 4.6 that for melt-spinning the cooling rate can reach this value as long as film (fibers) thickness stays in the range of 1μm to 5μm.

TEM analysis confirms the fully amorphous structure in as-quenched SS316-Ti since broad diffusive diffraction ring from its cross section shows no preferred crystal orientation contributing to forming the ring. The fibers after heat-treatment form crystals with average grain size of 84 nm. One clear information here is the inhomogeneous microstructure of SS316-Ti after heat-treatment. In fact, the diffraction pattern at different parts of the sample shows both amorphous and crystalline structure. Some grains are fully crystalline and represent themselves as sharp diffraction point and some areas are still remaining amorphous in the background with the presence of few nanocrystals within. The formation of nanocrystals within is observed by diffraction point at the diffusive amorphous ring. Formation of crystals here is not defect free and in higher magnification TEM images dislocation is formed in the border of two lattices. These dislocations cannot largely affect the plastic deformation of the sample since the dislocation motion will be stopped after maximum two or three lattices reaching the amorphous grain. Some scientists however described similar mechanism of deformation in amorphous metals to those of dislocations e.g. Gilman [104]. Other considerable parts of its microstructure is the formation of moire fringe by combining more than one crystal lattice. Since SS316-Ti has lots of alloying elements including carbide formers such as Cr and Ti, it is expected that some intermetallic alloys are also precipitated within the material while annealing.

Going back to the amorphous ring of heat-treated SS316-T, we see that it has much sharper intensity profile than the amorphous ring of as-quenched SS316-Ti. This is because annealing a metallic glass can produce reversible and irreversible structural relaxations. It is very difficult to characterize the structural changes but the irreversible relaxation is often associated with the short-range topological changes. As a consequence of this topological change, the density increases and consequently the elastic modulus. Indeed, looking at Figure 10.11 again, we observe that annealed SS316-Ti has a elastic modulus 36% larger than its amorphous form. Knuyt et al [105] previously reported that Elastic Modulus in amorphous alloys is about 30 smaller than the corresponding crystalline structure. This difference in elastic modulus can be explained in terms of change in atomic spacing. Wearire et al[106] proposed that the local environment influences the atomic rearrangement in response to shear stress. In a crystalline structure, atomic spacing is well-defined and thus their displacement toward a specific macroscopic strain is defined. However, in a glass structure, there are wider ranges of atomic environments and since they are not as densely packed as crystals, there are more possibilities for their rearrangement toward a macroscopic strain. Simulations show that these “internal rearrangements” reduce the shear modulus by about 30, in agreement with the experimental observations[106],[105].

Figure 10.11 shows a linear relationship between the hardness and elastic modulus values in amorphous metals. This linearity is not observed for crystalline metals and alloys and one cannot predict a hardness value of a crystalline alloy based on its elastic modulus. Going back to the mechanism of plastic deformation in glassy metals, we can explain why. The macroscopic scale plastic deformation in amorphous alloys is essentially a biased accumulation of local strains which happened during the operation of STZs and the redistribution of free volume. If the flow (steady-state condition) is homogeneous, there is a balance between events creating free volume and the annihilation of these free volumes. We previously discussed that density affects elastic modulus; on the other side, how densely atoms are distributed or in other words the availability of free volume determines the plastic response of amorphous alloys. That is why the hardness and elastic modulus of these materials are linearly correlated. In crystalline metals however, at each temperature there are numbers of phenomena that can contribute to plastic deformation e.g. dislocation, creep, climb. In fact, it is the mechanism with the lowest activation energy that determines which phenomena will be dominant. Such simple linearity between the elastic modulus and their hardness cannot be observed therefore.

Going back to Figure 10.11 again, the conventional and heat-treated SS316-Ti share the same elastic modulus values. However, the heat-treated SS316-Ti has 7 times higher hardness. One argument to justify such higher hardness value is through Hall-Petch effect and grain refinement. SS304 has mechanical properties almost identical to SS316-Ti. In Figure 10.12, the hardness of SS304 with different grain sizes is shown. Based on Hall-Petch formula, their hardness is increasing inversely linear to square root of grain size. If we follow the slop, for SS316-Ti with average grain size of 84nm the hardness must reach 7.45 GPa but we know that its hardness is almost 2 times higher. Thus, grain refinement cannot cause such high hardness alone.

We observed already in TEM images and diffractions that heat-treated SS316-Ti is a mixture of amorphous and nanocrystalline structure. If it was fully amorphous, based on its Elastic Modulus (and density) its predicted hardness could be around 12 GPa, and if fully nanocrystalline about 7.5 GPa. Its final hardness is however higher than both cases and about 14GPa. This behavior can be explained similar to composites mechanical properties where 2 phases mechanically different from each other contribute to higher hardness.

Classical wear theories emphasizes hardness as the prime property defining the wear resistance of a surface. It was Oberle for the first time who started ranking material according to their ratio of hardness to elastic modulus (H/E) and figured out that this ratio is in good agreement with wear resistance. Many studies later that this ratio gives a measure of elastic limit in the surface[107]. Thus, wear release can be avoided by predicting the elastic limit in the surface. In this chapter nanoindentation and wear resistance of as-quenched and heat-treated SS316-Ti were measured to see this correlation. If we predict the wear resistance according to H/E ratio, this ratio will be equal to 0.06 and 0.07 for as-quenched and heat-treated SS316-Ti fibers respectively. Based on this ratio one must predict higher wear resistance for heat-treated samples comparing to as-quenched fibers. This is in agreement with ICP-OES measurements of released ions from as-quenched and heat-treated fibers.

It was for a long time believed that nanocrystallization must lead to low corrosion resistance due to their high free energy. However, it was later shown that there is no such direct correlation between nanocrystallization and low corrosion resistance[80], [94]. Here, we can explain this difference in corrosion resistance by the fact that first of all the surface hardness of annealed fiber is much higher that can contribute to less wear release. Secondly, the annealed sample contains relax residual amorphous phase which means its internal stress due to processing technique is reduced. The comparison between their relax state was previously made in Figure 10.8. Consequently, less internal stress and higher surface hardness can lead to better wear resistance observed in ICP-OES measurements.

Better understanding of how dual-phase microstructure in stainless steel can contribute to such increase in mechanical properties requires more microstructural and micromechanical investigations which is beyond the purpose of this thesis.

Part III.

Vitrovac Microfibers

12. Introduction to Vitrovac

Among all the alloys and elements used for melt-spinning microfiber, the most promising result belonged to vitrovac. This small chapter is allocated to vitrovac fibers characterization.

$Co_{66}Fe_4Mo_2Si_{16}B_{12}$, commercially known as vitrovac 6025X, is an amorphous metallic ribbon produced by Vacuumschmelze GmbH which is an ideal material for magnet heads, magnetic field sensors, chokes, transformers, and electronic article surveillance tags. It has very high magnetic permeability and very low losses, and its saturation induction (B_s) is equal to 0.58 T. The very soft magnetic properties such as low coercivity and high initial magnetic permeability can be improved upon annealing at temperatures below the crystallization temperature[108].

Magnetic softening due to nanocrystallization was shown by Aguilarsahagun et.al[109], and Betancourt et.al[110] for $Co_{66}Fe_4Mo_2Si_{16}B_{12}$ alloy, $Co_{66}Fe_4Mo_2Si_{16.5}B_{11.5}$ [111], and $Co_{66}Fe_4Ni_1Si_{15}B_{14}$ [112]. The magnetic behavior is based on Co-based grains in the range of 2 to 20nm which are embedded in an amorphous Fe-rich matrix. The magnetic exchange interaction length is larger than grain size; thus, magnetic interactions lead to the averaging the magnetocrystalline anisotropy. The magnetic interactions in this case is much more complicated than Fe-based nanocrystalline alloys because of Co, Co_2B and Co_3B crystalline phases. In the alloys mentioned above, magnetic interactions seem to be much more complicated than in Fe-based nanocrystalline alloys owing to the presence of different Co, Co_2B and Co_3B crystalline phases[112],[111]. Swierczek et.al reported that by annealing $Co_{71}Fe_1Mo_1Mn_4Si_{14}B_9$, it get harder (magnetic). He also showed that showed that conventional heating of amorphous Vitrovac 6025X causes its further softening which occurs in the amorphous state. This effect might be due to the size increase of the atomic MRO domains [113].

13. Materials and Methods

13.1. Fabricating vitrovac fibers

$Co_{66}Fe_4Mo_2Si_{16}B_{12}$ alloy commercially known as Vitrovac 6025X was purchased from Vacuumschmelze GmbH in the form of ribbons, and then were re-melted and casted in the form of metal-rode with 12mm diameter at Max Planck Institute for Intelligent Systems materials preparation group. The standard procedure of melt-spinning for fiber formation was used for fabricating vitrovac fibers. Experimental melt-spinning parameters are summarized in Table 13.1.

13.2. SQUID and ULF measurements

All the magnetic measurement were done by MPMS3 SQUID Magnetometer (superconducting quantum interference device) from "Quantum Design". The device had the capability of in-situ heating chamber, and measuring at ultra low field for less than 10 Oe magnetic fields. Single fibers, or parallel fibers with comparable size were fixed in the sample holder and placed parallel or perpendicular to the external magnetic field. The field range was selected for each sample depending on its H_c value. As-quenched vitrovac fibers were measured by Ultra Low Field (ULF) wizard from the same device. All the measurements were done at room temperature.

Table 13.1.: Vitrovac fabrication experimental parameters

Wheel type	V (m/s)	δ (μm)	G (μm)	P (mbar)	ΔP (mbar)	$T_{ejection}$ (°C)
Flat Cu wheel	60	25	200	400	1850	1400

14. Experimental Results

Optical image of vitrovac fibers after melt-spinning is shown in Figure 14.1. They macroscopically look homogeneous regarding shape and size.

Taking a closer look at vitrovac fibers using SEM in Figure 14, we get to see more details regarding of their shape and size. Even though here no quantification is presented, it is clear that fibers have homogeneous size and look. Figure 14.2a shows that there are two categories of fibers shapes within the same batch: the more circular fibers and the more ribbon-shape fibers. The smaller fibers are more circular and bigger fibers have more ribbon-shape. The surface of fibers look quiet smooth unlike what has been seen before in case of other elements and alloys.

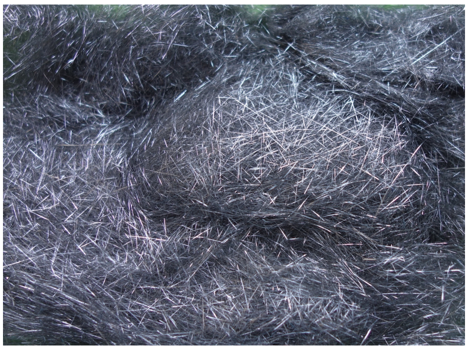

Figure 14.1.: Optical image of vitrovac fibers made by melt-spinning.

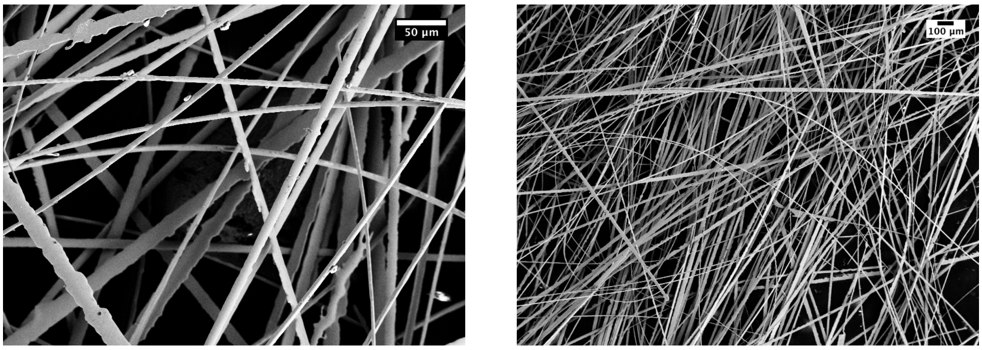

(a) high magnification SEM

(b) low magnification SEM

Figure 14.2.: SEM pictures of Vitrovac fibers at two different magnifications. It can be seen that fibers have the same range of size and are mostly round and circular.

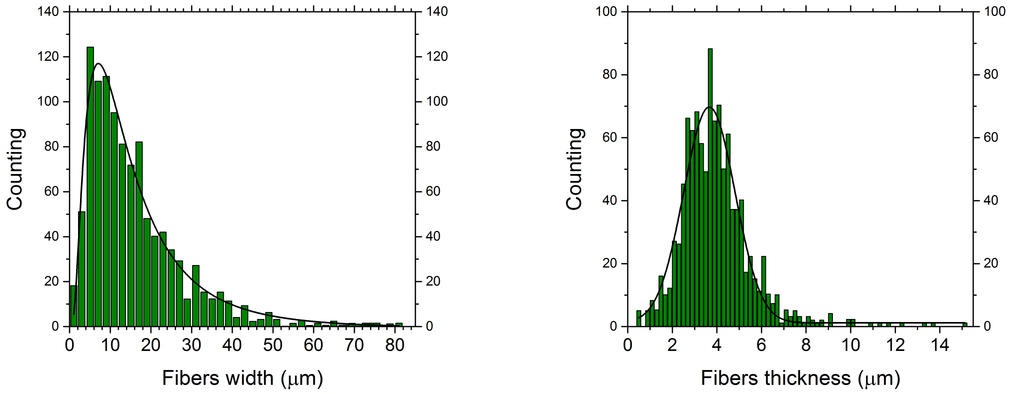

(a) vitrovac fibers width size distribution **(b)** vitrovac fibers thickness size distribution

Figure 14.3.: Vitrovac fibers width and thickness size distribution. Thickness distribution follows a Gaussian while there is a deviation from Gaussian shape for width distribution of fibers.

To have some values regarding the size of fibers, 1065 fibers sizes were measured regarding their width and thickness which is shown in Figure 14. According to these figures, vitrovac fibers thickness has a Gaussian distribution, while their width is not Gaussian, and its peak is shifted to smaller width values. The mean value for thickness is about 10μm while this mean value is half of this value for their thickness ans is about 5μm.

To evaluate the crystalline state of fibers, X-ray diffraction was used directly on the fibers. Their XRD is shown in Figure 14.4. No crystalline peak can be seen instead a very diffusive peak is observed between 2θ=40°-60°.

To be able to determine the glass transition temperature of vitrovac fibers, differential thermal analysis (DTA) was used. This DTA curve during cooling and heating is shown in Figure 14.5. The measurement shows a strong artifacts at 250°C resulting from the non-linear heating behavior of the furnace at low temperatures. At 525.0°C, a weak second order exothermal signal was detected. At 602.4°C a first order exothermal signal was observed. After the measurement a mass change of Δm = –0.05 mg was observed. Therefore, a significant oxidation of the material was excluded.

Vitrovac 6025X is a soft magnetic material. To be able to characterize its magnetic properties, superconducting quantum interference device (SQUID) and ultra low field SQUID (ULF) was used. The SQUID and ULF measurements of vitrovac fibers are shown in Figure 14. The left figure represents the hysteresis of hundreds of fibers placed parallel to the external magnetic field while the right figure shows the hysteresis of a single vitrovac fiber parallel to the external magnetic field. The

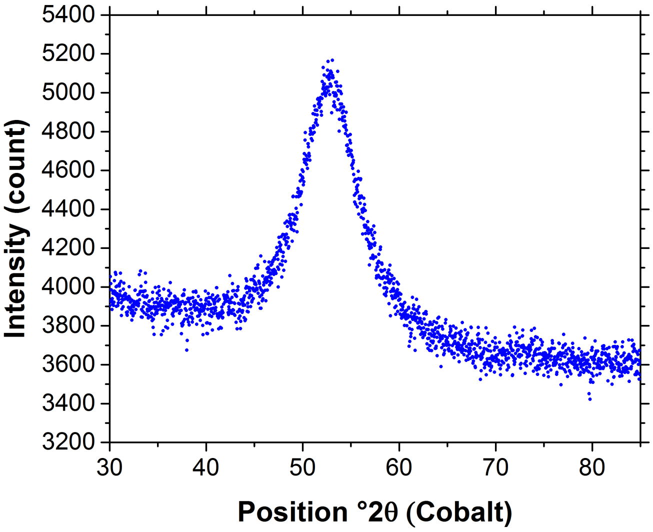

Figure 14.4.: Vitrovac fibers XRD. No crystalline peak can be seen. A diffusive peak between $2\theta = 40 - 60^\circ$ can be seen which is an indication of amorphous structure.

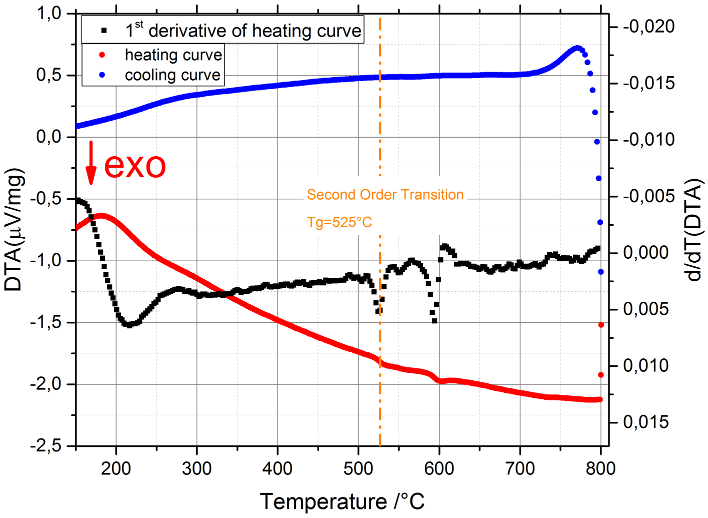

Figure 14.5.: DTA pattern obtained from vitrovac fibers. At 525.0°C a weak second order exothermal signal was detected as an indication of glass transition temperature. At 602.4°C a first order exothermal signal was detected.

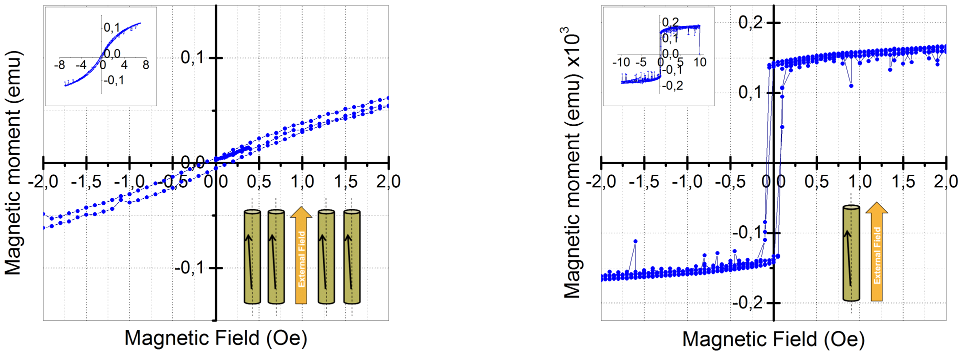

(a) hundred fibers parallel to external field

(b) single fiber parallel to external field

Figure 14.6.: Ultra low field SQUID measurement of vitrovac fibers when: a) 100 parallel fibers are placed parallel to external magnetic field b) a single fiber is placed parallel to external magnetic field. The hysteresis for a single fiber is very sharp while its transition is smooth for 100 parallel vitrovac fibers.

hysteresis is very narrow and the width of the hysteresis is about 0.1 Oe. The saturation level of their magnetic moment is different and in the case of hundreds of parallel fibers is 3 order of magnitude higher than a single fiber. It can also be seen in this figure that the hysteresis of hundred parallel fibers have a smooth saturation behavior while a single fiber is behaving almost like a magnetic switch and its saturation is very sharp.

To see the behavior of the single vitrovac fiber according to the direction of external magnetic field, the same fiber was fixed and placed perpendicular to the external magnetic field. The difference between these two orientations is shown in Figure 14. As it can be seen, when the fiber is placed perpendicular to the external magnetic field direction, the width of its hysteresis gets wider. H_c at this orientation is 200 times higher than when the fiber was placed parallel to the external magnetic field. Another distinguishing facts in this figure is that the magnetic moment hardly get saturated at perpendicular orientation.

To see how the crystallization can affect the hysteresis of vitrovac fibers, they were heat treated at three different isothermal temperatures: 650°C, 750°C, and 850°C. The in-situ XRD of the fibers at each of these temperatures were also done. Figure 14 shows the in-situ XRD of the fibers at these selected temperatures and the hysteresis of fibers annealed at each of these temperatures. The evolution of crystallization can be seen in the in-situ XRD of the fibers. Starting from amorphous structure, crystalline peaks appear at 650°C. Going to higher temperatures, no new peak appears but all crystalline peaks get sharper. We previously measured

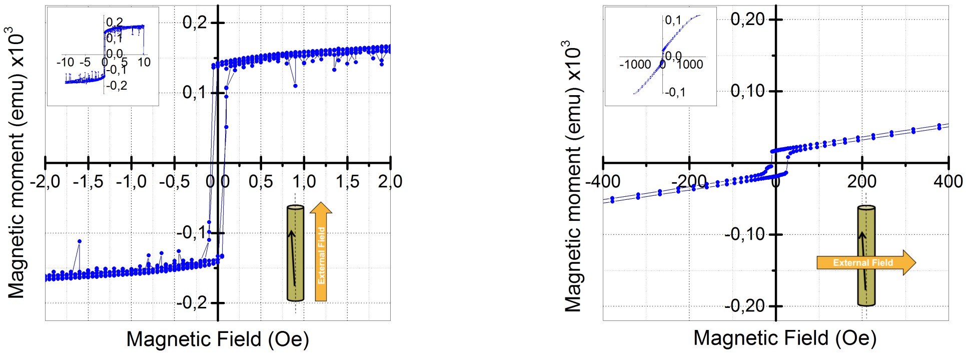

(a) single fiber parallel to external field **(b)** single fiber perpendicular to external field

Figure 14.7.: Comparison between the effect of fibers orientation toward external magnetic field direction. Hc of perpendicular fiber is 200 times higher than the parallel fiber and it hardly get saturated at all.

H_c=0.1 Oe for amorphous fibers, now this H_c is 40 Oe for fibers annealed at 650°C. Going to higher temperature at 750°C, this H_c increases even more: H_c=125 Oe. However, increasing the annealing temperature to 850°C, this H_c returns to its original amorphous value which here is less than 5 Oe (normal SQUID device cannot measure lower than 5 Oe).

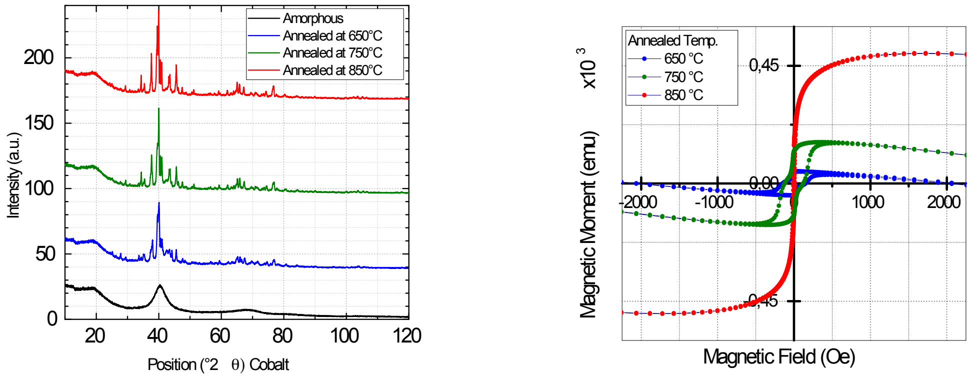

(a) XRD after annealing **(b)** hysteresis after annealing

Figure 14.8.: a) In-sit XRD of vitrovac fibers at different temperatures:650°C, 750°C, and 850°C. The hysteresis measurement of fibers annealed at this temperatures shows an increasing trend of H_c up to 750°C and then a sudden decrease to its original value before annealing at 850°C.

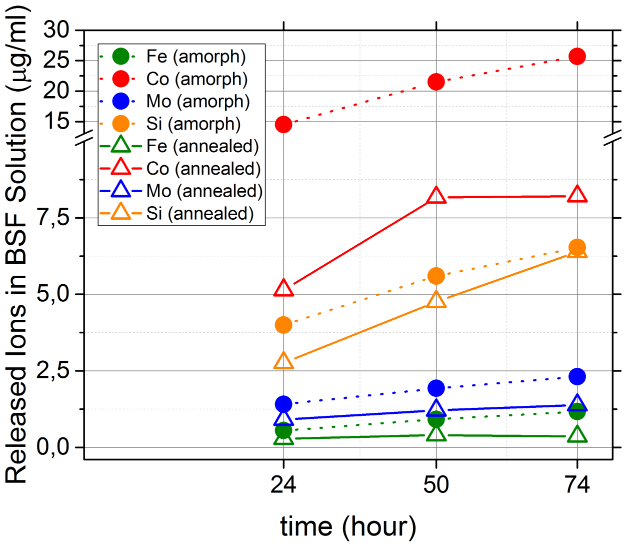

Figure 14.9.: ICP-OES measurements of released ions (Co,Fe,Mo,Si) from as-quenched and heat-treated vitrovac fibers into BSF saline solution. Measurements were done after 24,50, and 74h of keeping fibers in BSF solution. As-quenched fibers in general release more ions than heat-treated fibers. The cobalt-ion release increases by time significantly for as-quenched vitrovac fibers.

The comparison between isothermally annealed vitrovac and as-quenched vitrovac was made doing ICP-OES measurement of releasing ions from fibers to the BSF solution. The result is shown in Figure 14.9. The annealed fibers seem to release less ions and have higher wear resistance comparing to as'quenched fibers. This is specially visible for Cobalt ions which are the major composition of vitrovac alloy. In fact, annealed vitrovac fibers seem to saturate in releasing Cobalt ions after 50 hours. Mo and Fe ions are not released much in both heat-treated and annealed fibers and their release in BSF do not increase significantly by time.

Nanoindentation measurements of elastic modulus and hardness of vitrovac fibers are shortly presented in supplementary materials.

15. Discussion

Vitrovac fibers fabricated by melt-spinning had the most reproducible results in this project. Looking at their optical image in Figure 14.1, and SEM pictures in Figure 14 clearly show that they are almost homogeneous in shape and size. However, there are minor fibers in Figure 12.2 which shows that some fibers are more flat and they might even have an irregular shape. Quantification of fibers width and thickness sizes in Figure 12.3 shows that thickness values follow a Gaussian distribution function while the width of fibers have deviation from Gaussian is shifted toward larger values.

X-ray diffraction of vitrovac fibers has the broad diffusive peak as an indication of amorphous structure. This is for sure what one could expect from this alloy since it is designed to form an amorphous structure upon solidification. To estimate the glass transition temperature in vitrovac fibers, differential thermal analysis was done. Upon heating we observed the first "second order exothermal transition" at around 525°C which represents the glass transition temperature of vitrovac fibers. The second peak which is a first order exothermal transition was observed around 602.4°C which might be due to transformation to higher-temperature stable phases.

To characterize magnetic properties of vitrovac fibers, their hysteresis was measured using ultra low field SQUID. Figure 14 shows that when we measure the hysteresis for a single fiber, it has a sharp transition when it reaches maximum filed(H_c), and its magnetic moment immediately gets saturated. Thus, it is not wrong to say that it behaves like a magnetic switch. However, this behavior is not observed when hundreds of the same fibers are all aligned parallel to each other. They show a smooth saturation behavior. This can be explained by demagnetization of fibers aligned in the middle. Each fiber on the outer part demagnetize the fibers in the middle point which can later leads to this non-sharp smooth saturation behavior. To figure out the preferred direction of internal magnetic moment, a single fiber was fixed perpendicular to the direction of external magnetic field as well and the result shown in Figure 14 shows that this internal preferred direction is almost parallel to the direction of fibers length. That is why H_c is 200 times higher when the fibers are perpendicular to external magnetic field comparing to parallel orientation. This is also why their magnetic moment hardly get saturated at perpendicular orientation.

The extreme narrow hysteresis is due to the amorphous structure of vitrovac fibers. Since these fibers have no crystalline grain and thus grain boundaries, the domain wall can grow and move with the least microstructural obstacles resulting in very soft magnetic behavior.

In Figure 14 we observed that when the fibers are annealed at elevated temperatures (650°C, 750°C, and 850°C), they get crystallize and these crystals grow more and more, which can be seen as sharpening of their crystalline peaks in their XRD patterns. When the hysteresis of these annealed fibers are measured, their H_c first increases 400 times more than their original value (amorphous state) after annealing at 650°C. Annealing at higher temperature 750°C increases their H_c even more up to 125 Oe (1250 times higher than the original value). However, by going to 850°C and crystallizing them even more, suddenly their H_c returns to near its original value. This is a very known phenomena. When fibers are first annealed at 650°C, their grain size is in the nanometer range so their H_c increases significantly because of grain boundary creation. Increasing the number of grains by annealing them at 750°C makes their H_c closer to their maximum value. However, annealing at 850°C causes these grains to grow more until they are in the range of micrometer which can be compared with sintering effect when the number of grains reduce and so the grain boundaries. In this case, their H_c comes back to almost its original value.

Regarding the wear resistance comparison between annealed and as-quenched vitrovac fibers one can explain the increase of resistance after annealing by reducing internal stresses which was produce within vitrovac fibers during the melt-spinning process.

Overall, vitrovac 6025X could form small with homogeneous size distribution fibers by melt-spinning. Their magnetic properties are attractive and can be manipulated by annealing at different temperatures.

16. Final Summary

In this thesis, first, modification of geometrical parts of melt-spinning device and their effect on the final casted product were investigated e.g. wheel surface structure, slit size. Roughening and structuring the wheel surface could help in fiber fabrication. However, they could not provide a reproducible wheel surface and for that reason the rest of the research was carried out on the flat wheel surface. The slit size was shown to affect greatly the width and thickness of the produced fibers. It was shown that heat transfer coefficient of the wheel material determines its capability in processing any fibers.

Further modification of the process was pursued by optimizing and investigating melt-spinning experimental parameters such as wheel speed, applied pressure, ejection temperature, chamber pressure. Effect of each parameter on final size and shape of the fibers were presented and discussed. Wheel speed could affect the most the thickness of produced fibers while the rest of the parameters were significantly affecting the width of produced fibers. Minimum ejection pressure could not result in smallest fibers and an optimum pressure at 1000mbar could contribute to the smallest fibers. The gap between the wheel and the slit nozzle was shown to determine the shape of the fibers. When this distance is small, fibers tend to reach ribbon shape, and increasing greatly this distance might lead to no or very little fiber formation. Chamber pressure was shown to have effect on final size of the fiber, although it is possible to produce fibers even at very low chamber pressures.

Based on all experimental results, it was shown that by controlling the width of the fibers to less than 10μm one can produce the roundest fibers with AR<1.5. The equation predicting the thickness of $Fe_{40}Ni_{40}B_{20}$ alloy based on experimental parameters was obtained: t=0.0346 δ/V $\sqrt{\Delta P}$-1.84.

It was shown that running several experiments under the same experimental parameters would result in the same size of fibers. Thus, it was proved that not only the proof of principle in fiber formation by melt-spinning is valid, but it is also highly reproducible. The capability of the process for fabricating fibers based on other groups of materials such as metal elements, intermetallic alloys, conventional alloys and other amorphous alloys was examined, and in all cases fibers were formed by melt-spinning meaning the process was promising in terms of material choice. Besides, the results were more promising as expected for amorphous alloys.

High speed camera movies of melt-spinning process during melt ejection showed that when the slit size is very small (25μm), no melt-puddle forms and individual droplets sequentially wetting the film, forming the thin film are responsible for fiber formation. At larger slit size (50μm) however, the stationary melt-puddle was observed.

Based on SEM images of some not-fully formed fibers, and other experimental results it was concluded that the possible mechanism of fiber formation is as follows: i)wetting the rotating wheel and forming the thin film ii)spontaneous rupture of thin film (similar to Rayleigh instability) to smaller widths, and dewetting the wheel in forms of fibers.

Second chapter was fully dedicated to characterization of as-quenched and heat-treated SS316-Ti fibers. The astonishing result of these fibers were forming fully-amorphous structure for the first time after melt-spinning without any addition of refractory materials or other compositional changes. The subsequent heat-treatment was shown to create a dual phase microstructure in stainless steel consisting of relaxed residual glass phase and nanocrystals. The initial hardness of stainless steel before melt-spinning in the range of 2GPa increases to 8GPa after amorphization and it increased to even more, 14GPa, by subsequent heat-treatment. The High hardness value after heat-treatment was shown that is not due to only Hall-Petch effect. This high hardness value could be understood similar to composite microstructures where two mechanically different phases are involved. Wear resistance test also showed better resistance for heat-treated sample as one could expect based on the ratio of H/E of these alloys.

Last chapter was a small chapter dedicated to vitrovac fibers fabricated by melt-spinning. The purpose of this chapter was to better show the capability of melt-spinning in preparing soft-magnetic materials such as vitrovac in a very homogeneous size and shape distribution. They showed very soft magnetic properties. It was shown that by annealing at different temperatures, one can increase their H_c. ICP-OES measurements were also done to show their increase of mechanical properties after annealing.

Putting everything into a nutshell, this project was successful in introducing a new technique in fabrication of metal microfibers with small sizes, reproducible results, and wide material choices. The cooling rate of the process was enhanced comparing to the conventional melt-spinning which was responsible for amorphization of SS316-Ti fibers. Consequently, leading to ultra hard stainless steel microfibers after annealing.

17. Conclusion and Remarks

In this work, for the first time, metal microfibers were fabricated by melt-spinning technique. The results show that producing fibers in the range of 5μm is possible, and it is reproducible under same experimental parameters. Produced fibers however, have deviation from perfect circular fibers and this deviation was studies by a factor called cross-section aspect ratio(width/thickness of fibers).

The effect of different experimental parameters on final shape and size of fibers were investigated. It was shown that these parameters affect significantly the size of fibers width and fibers thickness mostly get affected by wheel speed. The experimental relation between parameters and fibers thickness was obtained.

It was shown that fibers cross-section aspect ratio is mostly circular when the width of fibers is less than 10μm. Therefore, one must control the width to have circular fibers.

The same principle was applied to different classes of materials, and it was shown that it is possible to work with single elements, intermetallic alloys, and conventional alloys and is not only designed for amorphous alloys. However, based on the results, the most promising results belonged to amorphous alloys in terms of fibers size and shape homogeneity. Fabrication of fibers based on single elements had the most technical difficulties.

High speed camera movies of melt-spinning process during melt-ejection showed that by decreasing the slit size, no melt-puddle forms and in stead the formation of fibers relies on single droplets wetting the rotating wheel with a constant diameter.

Microstructure and mechanical properties of SS316-Ti fibers was studied in a separate chapter. Fully amorphous stainless steel without any addition of refractory materials was reported, for the first time, in this work. The possibility of making stainless steel amorphous relied on the high quenching rate of modified melt-spinning device which was shown that it is capable of going to cooling rates as high as 10^{8}°C/s. The mechanical properties of amorphous SS316-Ti is in agreement with other glassy alloys (linear relation between hardness and elastic modulus). Further heat treatment of SS316-Ti results in dual-phase alloy consists of nanocrystals together with relaxed residual amorphous phase. The heat-treated SS316-Ti show ultra hardness comparing to its original crystalline form or even amorphous form. Its hardness is in the range of 14GPa. It was shown that grain refinement cannot cause such increase of hardness based on hall-petch effect. Therefore, the mechanism of its hardening could be similar to those of composite materials.

Vitrovac fibers were also shortly discussed in a separate chapter mostly because of their interesting magnetic properties. Their hysteresis confirms their very soft ferromagnetic properties. Their preferred internal magnetic direction is along the length of the fibers and in case of applying perpendicular external magnetic filed, their magnetic moment hardly get saturated. It was shown also that by annealing the fibers, it is possible to have larger H_c.

18. List of Publications

Pending patent application: "Apparatus and method of manufacturing metallic or inorganic fibers having a thickness in the micron range by melt spinning".

19. Future Work

Based on the promising result of fiber formation based on melt-spinning, it is meaningful to study further the mechanism of fiber formation and its modeling in future works. Since the project has a great potential for industrial applications, larger scale fabrication of fibers can be the next step to be studied as well.

Studying the dual phase structure of amorphous phase and nanocrystals can be very interesting to study in future, and their effect on mechanical properties of material.

20. Supplementary Materials

20.1. Melt-spinning parameters of all experiments

The experimental parameters of all experiments done at this project by the author of this thesis is summarized in Table 20.1. Here, the flat copper wheel is shown by Cu and flat copper-alloy as Cu_a. W is the wheel material, δ is the slit size, f is the wheel frequency, P is chamber pressure, ΔP the applied pressure, G is the distance between slit and wheel, and T is the melt ejection temperature. The Cu_g wheel had grooves on its cross-section. Some special slit structures are stated as a, b, etc. The slit a had microstructures at one side of the slit. Slit b had an internal 20° inside the slit. Slit c had the internal angle toward the opposite direction of ejection. Slit d was a microchannel (see Materials and Methods). Slit e has a 100 μm diameter hole instead of rectangular cross-section. Slit f has 5 holes, each 100 μm diameter .

Table 20.1.: Melt-Spinning experiments and their parameters.

Nr.	Material	W	δ	f	P	Δ P	G	T
unit	-	-	μm	Hz	mbar	mbar	μm	°C
MS027	$Fe_{40}Ni_{40}B_{20}$	B	100	85	400	300	200	1350
MS028	$Fe_{40}Ni_{40}B_{20}$	B	100	85	400	400	200	1350
MS029	$Fe_{40}Ni_{40}B_{20}$	B	100	85	400	400	200	1350
MS030	$Fe_{40}Ni_{40}B_{20}$	B	100	85	400	400	200	1350
MS031	$Fe_{40}Ni_{40}B_{20}$	B	100	85	400	400	200	1350
MS032	$Fe_{40}Ni_{40}B_{20}$	B	100	85	400	400	200	1350
MS033	$Fe_{40}Ni_{40}B_{20}$	C	100	85	400	400	200	1350
MS034	$Fe_{40}Ni_{40}B_{20}$	A	100	85	400	400	200	1350
MS035	$Fe_{40}Ni_{40}B_{20}$	A	75	85	400	600	200	1350
MS036	$Fe_{40}Ni_{40}B_{20}$	A	50	85	400	1000	200	1350
MS037	$Fe_{40}Ni_{40}B_{20}$	A	50	85	400	1000	200	1350
MS038	$Fe_{40}Ni_{40}B_{20}$	C	50	85	400	1000	200	1350
MS039	$Fe_{40}Ni_{40}B_{20}$	C	75	85	400	600	200	1350
MS040	$Fe_{40}Ni_{40}B_{20}$	Cu	a	85	400	200	200	1350
MS041	$Fe_{40}Ni_{40}B_{20}$	Cu	50	85	400	1000	200	1350
MS042	$Fe_{40}Ni_{40}B_{20}$	Cu	50	85	400	1000	200	1350
MS043	$Fe_{40}Ni_{40}B_{20}$	Cu	50	85	400	1500	200	1350

MS044	$Fe_{40}Ni_{40}B_{20}$	Cu	75	85	400	600	200	1350
MS045	$Fe_{40}Ni_{40}B_{20}$	Cu	100	85	400	400	200	1350
MS046	$Fe_{40}Ni_{40}B_{20}$	Cu	50	100	400	1500	200	1350
MS047	$Fe_{40}Ni_{40}B_{20}$	Cu	200	95	400	200	200	1350
MS048	$Fe_{40}Ni_{40}B_{20}$	Cu	400	95	400	200	200	1350
MS049	$Fe_{40}Ni_{40}B_{20}$	Cu	25	95	400	1500	200	1350
MS050	$Fe_{40}Ni_{40}B_{20}$	Cu	50	95	400	1000	200	1350
MS051	$Fe_{40}Ni_{40}B_{20}$	Cu	75	95	400	600	200	1350
MS052	$Fe_{40}Ni_{40}B_{20}$	Cu	100	95	400	400	200	1350
MS053	Zn	Cu	200	95	400	200	200	700
MS054	Zn	Cu	50	95	400	1000	200	750
MS055	Al	Cu	200	95	400	200	200	850
MS056	Al	Cu	50	95	400	1000	200	900
MS057	SS316-Ti	Cu	200	95	400	300	200	1500
MS058	SS316-Ti	Cu	75	95	400	800	200	1500
MS059	$Fe_{40}Ni_{40}B_{20}$	D	50	95	400	1000	200	1350
MS060	$Fe_{40}Ni_{40}B_{20}$	D	25	95	400	1500	200	1350
MS061	$Fe_{40}Ni_{40}B_{20}$	C	75	95	400	600	200	1350
MS062	$Fe_{40}Ni_{40}B_{20}$	C	100	95	400	400	200	1350
MS063	$Fe_{40}Ni_{40}B_{20}$	C	200	95	400	200	200	1350
MS064	$Fe_{40}Ni_{40}B_{20}$	C	400	95	400	200	200	1350
MS065	$Fe_{40}Ni_{40}B_{20}$	C	50	95	900	1000	200	1350
MS066	$Fe_{40}Ni_{40}B_{20}$	C	75	95	900	600	200	1350
MS067	$Fe_{40}Ni_{40}B_{20}$	C	50	95	400	1000	200	1350
MS068	$Fe_{40}Ni_{40}B_{20}$	C	50	95	400	1000	200	1350
MS069	$Fe_{40}Ni_{40}B_{20}$	C	25	95	400	1500	200	1350
MS070	$Fe_{40}Ni_{40}B_{20}$	Cu	50	95	400	1500	200	1350
MS071	$Fe_{40}Ni_{40}B_{20}$	Cu	50	95	400	1500	200	1350
MS072	$Fe_{40}Ni_{40}B_{20}$	Cu	50	95	400	1500	200	1350
MS073	$Fe_{40}Ni_{40}B_{20}$	Cu	50	95	400	1000	300	1350
MS074	$Fe_{40}Ni_{40}B_{20}$	Cu	25	95	400	1500	200	1350
MS075	$Fe_{40}Ni_{40}B_{20}$	Cu	25	95	400	1500	200	1350
MS076	$Fe_{40}Ni_{40}B_{20}$	Cu	50	95	400	1000	200	1350
MS077	$Fe_{40}Ni_{40}B_{20}$	Cu	50	95	400	1000	200	1350
MS078	$Fe_{40}Ni_{40}B_{20}$	Cu	50	95	Vac.	1000	200	1350
MS079	$Fe_{40}Ni_{40}B_{20}$	Cu	75	95	400	600	100	1350
MS080	$Fe_{40}Ni_{40}B_{20}$	Cu	75	95	400	600	300	1350
MS081	$Fe_{40}Ni_{40}B_{20}$	Cu	75	95	400	600	250	1350
MS082	$Fe_{40}Ni_{40}B_{20}$	Cu	75	95	400	600	200	1350

MS083	$Fe_{40}Ni_{40}B_{20}$	Cu	50	95	400	1000	100	1350
MS084	$Fe_{40}Ni_{40}B_{20}$	Cu	50	95	400	1000	200	1350
MS085	$Fe_{40}Ni_{40}B_{20}$	Cu	25	95	400	1000	100	1350
MS086	$Fe_{40}Ni_{40}B_{20}$	Cu	25	95	400	1000	100	1350
MS087	$Fe_{40}Ni_{40}B_{20}$	Cu	50	95	400	1000	300	1350
MS088	$Fe_{40}Ni_{40}B_{20}$	Cu	50	95	400	1000	200	1350
MS089	$Fe_{40}Ni_{40}B_{20}$	Cu	50	95	400	1000	200	1500
MS090	$Fe_{40}Ni_{40}B_{20}$	Cu	50	95	400	1000	200	1300
MS091	$Fe_{40}Ni_{40}B_{20}$	Cu	50	95	400	800	200	1350
MS092	$Fe_{40}Ni_{40}B_{20}$	Cu	50	95	400	700	200	1350
MS093	$Fe_{40}Ni_{40}B_{20}$	Cu	50	95	400	650	200	1350
MS094	$Fe_{40}Ni_{40}B_{20}$	Cu	50	95	400	650	200	1350
MS095	$Fe_{40}Ni_{40}B_{20}$	Cu	100	95	400	400	200	1350
MS096	$Fe_{40}Ni_{40}B_{20}$	Cu	100	95	400	400	200	1350
MS097	$Fe_{40}Ni_{40}B_{20}$	Cu	100	95	400	400	200	1350
MS098	$Fe_{40}Ni_{40}B_{20}$	Cu	50	95	400	1000	200	1400
MS099	$Fe_{40}Ni_{40}B_{20}$	Cu	50	95	400	1000	200	1300
MS100	$Fe_{40}Ni_{40}B_{20}$	Cu	50	95	400	700	200	1300
MS101	$Fe_{40}Ni_{40}B_{20}$	Cu	50	95	400	700	200	1300
MS102	$Fe_{40}Ni_{40}B_{20}$	Cu	50	95	500	700	200	1400
MS103	$Fe_{40}Ni_{40}B_{20}$	Cu	50	95	500	700	200	1400
MS104	$Fe_{40}Ni_{40}B_{20}$	Cu	50	95	400	700	200	1300
MS105	$Fe_{40}Ni_{40}B_{20}$	Cu	50	95	400	700	100	1300
MS106	$Fe_{40}Ni_{40}B_{20}$	Cu	50	95	400	650	100	1300
MS107	$Fe_{40}Ni_{40}B_{20}$	Cu	50	95	400	700	100	1300
MS108	$Fe_{40}Ni_{40}B_{20}$	SS	50	95	400	800	200	1300
MS109	$Fe_{40}Ni_{40}B_{20}$	SS	400	60	400	100	200	1300
MS110	$Fe_{40}Ni_{40}B_{20}$	Cu	b	95	400	800	200	1400
MS111	$Fe_{40}Ni_{40}B_{20}$	Cu	b	95	400	800	200	1300
MS112	$Fe_{40}Ni_{40}B_{20}$	Cu	25	95	400	1300	200	1400
MS113	$Fe_{40}Ni_{40}B_{20}$	Cu_a	25	95	400	1500	200	1400
MS114	SS316-Ti	Cu_a	50	95	400	1200	200	1400
MS115	SS316-Ti	Cu_a	50	95	400	1200	200	1560
MS116	Zn	Cu_a	50	95	400	800	200	650
MS117	Zn	Cu_a	50	95	400	650	200	650
MS118	Al	Cu_a	50	95	400	800	200	880
MS119	Al	Cu_a	50	95	400	800	200	1080
MS120	$Fe_{40}Ni_{40}B_{20}$	Cu_g	75	85	400	600	200	1350
MS121	$Fe_{40}Ni_{40}B_{20}$	Cu	75	60	400	600	200	1350

MS122	$Fe_{40}Ni_{40}B_{20}$	Cu	75	95	400	600	200	1350
MS123	$Fe_{40}Ni_{40}B_{20}$	Cu	75	30	400	600	200	1350
MS124	$Fe_{40}Ni_{40}B_{20}$	Cu	75	10	400	600	200	1350
MS125	SS316-Ti	Cu	50	95	400	1300	200	1450
MS126	SS316-Ti	Cu	50	95	400	1300	200	1450
MS127	SS316-Ti	Cu	50	95	400	1200	200	1450
MS128	SS316-Ti	Cu	50	95	400	1200	200	1450
MS129	$Fe_{40}Ni_{40}B_{20}$	Cu	50	95	400	700	200	1350
MS130	$Fe_{40}Ni_{40}B_{20}$	Cu	50	95	400	700	200	1350
MS131	$Fe_{40}Ni_{40}B_{20}$	Cu	50	95	400	700	200	1350
MS132	SS316L	Cu	50	95	400	1200	200	1450
MS133	SS316L	Cu	50	95	400	1200	200	1450
MS134	$Fe_{40}Ni_{40}B_{20}$	Cu	25	95	400	1500	200	1350
MS135	$Fe_{40}Ni_{40}B_{20}$	Cu	75	95	400	500	200	1350
MS136	$Fe_{40}Ni_{40}B_{20}$	Cu	100	95	400	400	200	1350
MS137	$Fe_{40}Ni_{40}B_{20}$	Cu	200	95	400	200	200	1350
MS138	$Fe_{40}Ni_{40}B_{20}$	Cu	400	95	400	100	200	1350
MS139	$Fe_{40}Ni_{40}B_{20}$	Cu	50	95	400	700	200	1350
MS140	SS316L	Cu	50	95	400	1200	200	1450
MS141	SS316-Ti	Cu	75	95	400	1200	200	1450
MS142	$Fe_{40}Ni_{40}B_{20}$	Cu	25	95	400	1800	200	1350
MS143	$Fe_{40}Ni_{40}B_{20}$	Cu	50	95	400	700	200	1500
MS144	$Fe_{40}Ni_{40}B_{20}$	Cu	50	95	400	700	200	1300
MS145	$Fe_{40}Ni_{40}B_{20}$	Cu	75	95	800	500	200	1350
MS146	Vitrovac	Cu	100	95	400	600	200	1400
MS147	$Fe_{40}Ni_{40}B_{20}$	Cu_a	75	95	400	700	200	1350
MS148	$Fe_{40}Ni_{40}B_{20}$	Cu_a	25	95	400	1500	200	1350
MS149	$Fe_{40}Ni_{40}B_{20}$	Cu_a	75	95	400	700	200	1350
MS150	$Fe_{40}Ni_{40}B_{20}$	Cu_a	50	95	400	1000	200	1350
MS151	$Fe_{40}Ni_{40}B_{20}$	Cu_a	50	95	400	1000	200	1350
MS152	$Fe_{40}Ni_{40}B_{20}$	Cu_a	50	95	400	1000	200	1350
MS153	$Fe_{40}Ni_{40}B_{20}$	Cu_a	50	95	400	1000	200	1350
MS154	$Fe_{40}Ni_{40}B_{20}$	Cu_a	50	95	400	1000	200	1350
MS155	Vitrovac	Cu_a	100	95	400	600	200	1400
MS156	Vitrovac	Cu_a	c	95	400	1700	200	1400
MS157	$Fe_{40}Ni_{40}B_{20}$	Cu_g	25	95	400	1400	200	1300
MS158	$Fe_{40}Ni_{40}B_{20}$	Cu_g	100	90	400	500	200	1300
MS159	$Fe_{40}Ni_{40}B_{20}$	Cu_g	25	90	400	1500	200	1300
MS160	$Fe_{40}Ni_{40}B_{20}$	Cu_g	50	90	400	1000	200	1300

MS161	SS316-Ti	Cu_a	50	95	400	1500	200	1450
MS162	SS316-Ti	Cu_a	100	95	400	1000	200	1450
MS163	SS316-Ti	Cu_a	50	95	400	1000	200	1450
MS164	SS304	Cu_a	50	95	400	1000	200	1450
MS165	$Fe_{40}Ni_{40}B_{20}$	Cu_a	25	95	400	1500	100	1300
MS166	Ag	Cu_a	25	95	400	1200	200	1100
MS167	Ag	Cu_a	25	95	400	1400	200	1100
MS168	Ni_3Al	Cu	50	95	400	1200	200	1500
MS169	Ni_3Al	Cu	50	95	400	1200	200	1500
MS170	$Ni_3AlB_{0.4}$	Cu	50	95	400	1400	200	1500
MS171	Vitrovac	Cu	25	95	400	1850	200	1400
MS172	Vitrovac	Cu	25	95	400	1850	200	1400
MS173	Vitrovac	Cu	25	95	400	1850	200	1400
MS174	Vitrovac	Cu	25	95	400	1850	200	1400
MS175	Cu	Cu	50	95	400	800	200	1320
MS176	Cu	Cu	25	95	400	800	200	1250
MS177	$Ag_{90}Co_{10}$	Cu	50	95	400	400	200	1100
MS178	Cu	Cu	75	95	400	800	200	1271
MS179	Cu	Cu	50	95	400	700	200	1271
MS180	Cu	Cu	100	95	400	300	200	1300
MS181	Ag	Cu	25	95	400	1000	200	1220
MS182	Ag	Cu	75	95	400	300	200	1220
MS183	Ag	Cu	200	95	400	failed	200	1220
MS184	$Ag_{70}Co_{30}$	Cu	75	95	400	300	200	1200
MS185	SS316-Ti	Cu	50	95	400	1200	200	1460
MS186	SS316-Ti	Cu	50	95	400	1100	200	1460
MS187	SS304	Cu	50	95	400	1100	200	1460
MS188	$Fe_{40}Ni_{40}B_{20}$	Cu	50	95	400	1000	300	1460
MS189	$Fe_{40}Ni_{40}B_{20}$	Cu	50	95	400	1000	100	1350
MS190	$Fe_{40}Ni_{40}B_{20}$	Cu	50	95	400	1000	200	1350
MS191	$Fe_{40}Ni_{40}B_{20}$	Cu	50	95	800	1000	200	1350
MS192	$Fe_{40}Ni_{40}B_{20}$	Cu	50	95	Vac.	1000	200	1350
MS193	$Fe_{40}Ni_{40}B_{20}$	Cu	d	95	400	200	200	1350
MS194	$Fe_{40}Ni_{40}B_{20}$	Cu	50	95	400	1000	200	1450
MS195	$Fe_{40}Ni_{40}B_{20}$	Cu	50	95	400	800	200	1350
MS196	$Fe_{40}Ni_{40}B_{20}$	Cu	50	95	400	1500	200	1350
MS197	$Fe_{40}Ni_{40}B_{20}$	Cu	e	95	400	1700	200	1350
MS198	$Fe_{40}Ni_{40}B_{20}$	Cu	f	95	400	700	200	1350

Table 20.2.: Stainless steel alloys atomic composition (atomic%)

Type	C	Mn	Si	Cr	Ni	P	S	other
304	0.08	2.00	1.00	18.0-20.0	8.0-10.5	0.045	0.03	...
316-Ti	0.08	2.00	1.00	16.0-18.0	10.0-14.0	0.045	0.03	Ti≤5%C to Max 0.70%
316-L	0.03	2.00	1.00	16.0-18.0	10.0-14.0	0.045	0.03	2.0-3.0 Mo

20.2. Stainless steel alloy compositions

Three different austenitic grades of stainless steel were used in this project. Their chemical compositions is shown in Table 20.2.

20.3. Stainless steel fibers XRD

Due to lack of some experimental control during melt-spinning, specifically temperature, in some cases temperature deviation caused crystallization of samples during solidification by melt-spinning. Thus, the XRD of obtained as-quenched fibers differs from what discussed previously in stainless steel chapter. For this reason, the XRD analysis of some as-quenched fibers without such diffusive XRD-peaks are shown in Figure 20.3. Figure 20.2 is presented for better comparison between all the XRD graphs, and their peaks.

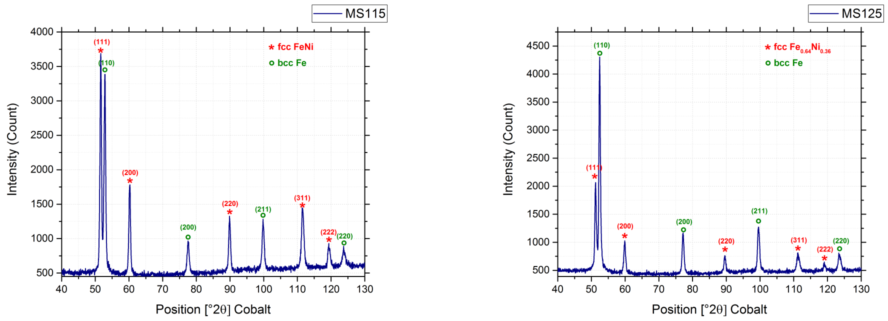

(a) 316-Ti stainless steel fibers **(b)** 316-Ti stainless steel fibers

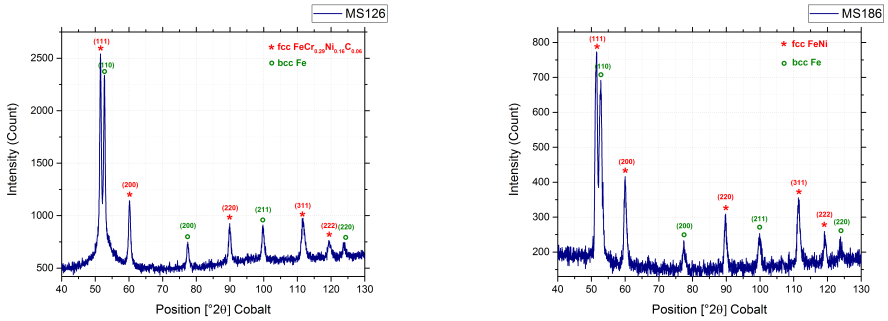

(c) 316-Ti stainless steel fibers **(d)** 316-Ti stainless steel fibers

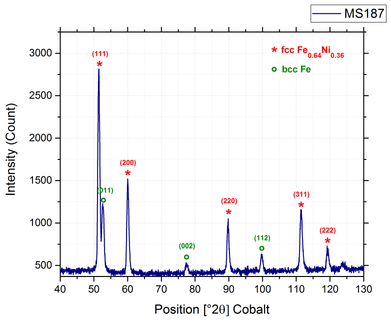

(e) 304 stainless steel fibers

Figure 20.1.: XRD obtained from stainless steel fibers after melt-spinning. The first four graphs are related to 316-Ti stainless steel. Even though the same peaks are identified for all of them, the intensity of peaks are not equal for the same type of steel fibers.

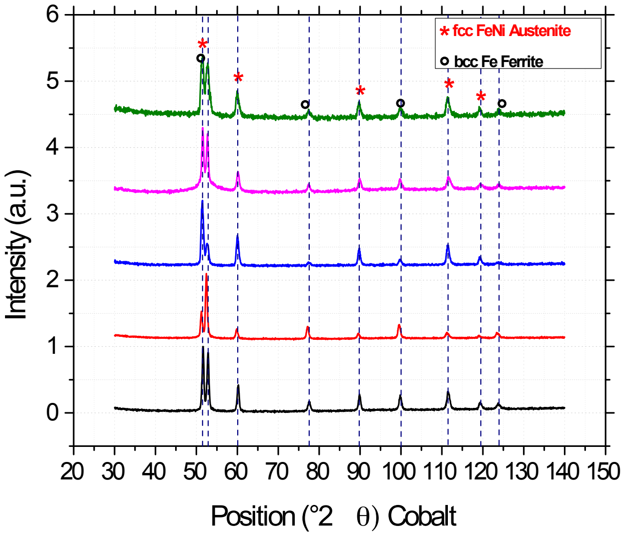

Figure 20.2.: XRD results of as-quenched SS316-Ti fibers after melt-spinning. They all share the same crystalline peaks, although the intensity of these peaks differs from sample to sample. The type of crystals found for all samples are fcc and bcc.

20.4. Mechanical properties of different fibers

The hardness and elastic modulus of fabricated fibers by melt-spinning are presented in Table 20.3.

Table 20.3.: Nanoindentation measurements of Elastic modulus and hardness for fabricated fibers

Material	Tip	Elastic Modulus (GPa)	Hardness (GPa)
SS304	cube corner	61.8	5.78
SS316-Ti crystalline	cube corner	101.17	7.90
SS316-Ti amorphous	cube corner	128.49	8.23
SS316-Ti annealed	cube corner	196.58	14.20
Vitrovac	cube corner	100	11.08
copper	berkovich	125.9	3.0
silver	berkovich	73.3	2.3

20.5. Bulk metallic glasses mechanical properties

In this section, a complete values of bulk metallic glasses hardness and elastic modulus taken from literature are presented. The numbers correspond to the ones used in Figure 10.11.

Table 20.4.: Elastic Modulus and Hardness values of different amorphous alloys used in Figure 10.11

Nr.	Alloy	E	H	Ref
unit	-	GPa	GPa	-
1	$Zr_{57}Ti_5Ni_8Cu_{20}Al_{10}$	85±1	4.6±0.1	[114]
2	$Hf_{11.4}Zr_{45.6}Ti_5Ni_8Cu_{20}Al_{10}$	87±1	4.7±0.1	[115]
3	$Hf_{22.8}Zr_{34.2}Ti_5Ni_8Cu_{20}Al_{10}$	94±1	5.2±0.1	[116]
4	$Zr_{52.5}Ti_5Ni_{14.6}Cu_{17.9}Al_{10}$	93±2	5.0±0.2	[116]
5	$Hf_{10.5}Zr_{42}Ti_5Ni_{14.6}Cu_{17.9}Al_{10}$	108±3	5.3±0.1	[116]
6	$Hf_{21}Zr_{31.5}Ti_5Ni_{14.6}Cu_{17.9}Al_{10}$	113±2	5.5±0.1	[116]
7	$Hf_{31.5}Zr_{21}Ti_5Ni_{14.6}Cu_{17.9}Al_{10}$	110±3	5.8±0.2	[116]
8	$Hf_{42}Zr_{10.5}Ti_5Ni_{14.6}Cu_{17.9}Al_{10}$	124±2	6.0±0.2	[116]
9	$Hf_{52.5}Ti_5Ni_{14.6}Cu_{17.9}Al_{10}$	128±4	6.1±0.2	[116]
10	$Zr_{57}Nb_5Ni_{12.6}Cu_{15.4}Al_{10}$	89±1	4.9±0.1	[116]
11	$(Al_{0.84}Y_{0.09}Ni_{0.05}Co_{0.02})_{95}Sc_5$	78	4.4	[117]
12	$(Al_{0.85}Y_{0.08}Ni_{0.05}Co_{0.02})_{95}Sc_5$	75	4.0	[117]
13	$Cu_{60}Hf_{25}Ti_{15}$	124	6.7	[118]
14	$Cu_{60}Hf_{30}Ti_{10}$	119	6.3	[118]
15	$Fe_{80}B_{20}$	167	10.6	[57]
16	$Fe_{80}P_{13}C_7$	118	7.5	[57]
17	$Fe_{78}B_{10}Si_{12}$	118	8.9	[57]
18	$(Fe_{0.75}B_{0.2}Si_{0.05})_{96}Nb_4$	180	10.5	[119]
19	$((Fe_{0.9}Co_{0.1})_{0.75}B_{0.2}Si_{0.05})_{96}Nb_4$	190	11.3	[119]
20	$((Fe_{0.8}Co_{0.2})_{0.75}B_{0.2}Si_{0.05})_{96}Nb_4$	205	12.0	[119]
21	$((Fe_{0.7}Co_{0.3})_{0.75}B_{0.2}Si_{0.05})_{96}Nb_4$	210	12.2	[119]
22	$((Fe_{0.6}Co_{0.4})_{0.75}B_{0.2}Si_{0.05})_{96}Nb_4$	210	12.3	[119]

23	$((Fe_{0.5}Co_{0.5})_{0.75}B_{0.2}Si_{0.05})_{96}Nb_4$	210	12.0	[119]
24	$Ni_{45}Ti_{20}Zr_{25}Al_{10}$	114	7.8	[120]
25	$Ni_{40}Cu_6Ti_{16}Zr_{28}Al_{10}$	111	7.6	[120]
26	$Ni_{40}Cu_5Ti_{17}Zr_{28}Al_{10}$	134	8.4	[120]
27	$Ni_{40}Cu_5Ti_{16.5}Zr_{28.5}Al_{10}$	122	7.8	[120]
28	$Ni_{39.8}Cu_{5.97}Ti_{15.92}Zr_{27.86}Al_{9.95}Si_{0.5}$	117	8.1	[120]
29	$Zr_{41.25}Ti_{13.75}Ni_{10}Cu_{12.5}Be_{22.5}$	96	5.2	[121]
30	$Pd_{80}Si_{20}$	67	3.2	[57]
31	$Pd_{40}Ni_{40}P_{20}$	108	5.3	[122]
32	$Pd_{77.5}Cu_6Si_{16.5}$	88	4.9	[122]

21. Acknowledgment

I had a chance of working on this project which was truly exciting and challenging at the same time for me. Working on this project, a bit off-topic from the rest of the department might have seemed difficult first, but it gave me the opportunity to explore the rest of the departments in Max Planck Institute for Intelligent Systems and Max Planck Institute for Solid State Physics, meeting wonderful people, working and learning from every single one of them. It was indeed the best part of this project. Many tests were inspired by talking to these people which many of them are my friends now; numerous technical problems which was impossible to solve if I could not have their support. I will try to name few here but it truly is more than what I just write down here.

I would like to first thank deeply Prof. Joachim Spatz for the chance he gave me to work on this project. He trusted me with many decisions, and gave me a lot of flexibilities to work on this project. I had the advantage of working under his direct supervision and I learned a lot from him.

Secondly, I would like to thank Dr. Alexandre Micoulet who contributed a lot in this project and for sure our beloved technician Mr. Reinhard Mager without whom all these could just be theoretical discussions. It was a lot of fun working with him in the lab. He saved me a lot of times by taking care of the device, collecting and documentation of many experiments. For me, coming from engineering background, it was also easier to communicate with him since many experimental problems needed practical opinion, and he indeed was the best person to get help from.

Dr. Moyu Watari, helped me in every single part of this PhD project. Besides of a great scientist she is, she was a true genuine friend to me. I cannot possibly put it into words to thank her enough. She always helped with the discussion of my thesis, presentations, talks, thesis-corrections and was more than a colleague to me. Knowing her for sure was one of the greatest thing about doing this PhD.

From the beginning of this project, I worked closely to Edmund Buehler GmbH and Binzer GmbH. I specially thank Mr. Schlecht and Mr. Bogenschuetz for their technical support regarding the melt-spinning device development. I had a pleasure to have regular meetings and discussion with Dr. Guenter Stephani which was a great scientific help to me. Mr. Seip the previous member of Binzer GmbH

also helped in many discussions and am grateful for all of these people help and contribution.

I have done mechanical testing and characterizations such as nanoindentation together with the Dr. Zaklina Burghard material science department of Stuttgart University. She helped with all the related discussions and her PhD students, Stefan Kilper and Achim Diem helped me a lot in nanoindentation and tensile test measurements. Her department were really friendly and I had real fun working with them.

I owe the experiments regarding the TEM images, FIB preparations and discussions related to stainless steel microstructure to Prof. Guido Schmitz and his PhD student Efi Hadjixenophontos. All related experiments were done in his department of Stauttgart University, in Max Planck IS campus. I appreciated a lot all the help Efi did and am looking forward to work with her again in future.

All the magnetic characterizations including SQUID and ULF measurements were done in Prof. Gisela Schuetz department in Max Planck IS. Dr Eberhard Goering, Dr Claudia Stahl and Stephen Ruoss contributed a lot into discussions and measurements.

It is clear that each part of this project was done with a different group. One major part of the project was dealing with lots of technical problem since the device was in development stage. At this stage, all the people from Max Planck mechanical shop, and materials preparation people including Mr. Arnold Weible and Mr. Thomas Meisner. To me, they make Max Planck a magical place like Hogwarts. They always have great tips, incredible ability in problem-solving and am grateful to work closely with them. Many ideas came into my mind talking to them. The produced microfibers had dimensions that no real set-up was available for their characterization. Each experiment needed a set-up and I developed them together with these wonderful people.

Mrs Felicitas Predel helped me a lot in metallography samples and Mr Samir Hammoud helped a lot in ICP-OES measurements. Mr Janis Grigoridis for his help with SEM and his sense of humor cheering us up all the time. Actually, if you google "Carlos Queiroz" the Portuguese football manager who is currently in charge of the Iran national football team, you will see that Janis has an identical face with him. I thought it is worth mentioning :D . For the XRD experiments, Mr G.Maier in the former department of Prof. Mittemeijer in Max Planck IS helped a lot. Dr. Marc Widenmeyer in the department of Prof. Anke Weidenkaff of Stuttgart University helped a lot in DTA measurements and the related discussions. Mrs. Christine Stefani from XRD service group of Prof. Dr. Robert E. Dinnebier in Max Planck fkf supported us in in-situ XRD measurements.

When I first came to Max Planck IS, I was a master student in the same department. So I had a chance of making friends for a life time, and they were an important part of my life during my master and PhD project. Being abroad and dealing with different challenges could be tough at times but overall it is friends who make the whole thing worth it and an enjoyable memory of a life time. Maybe even the best part of my stay in Germany was them. I would like to name few of them which forever made this time of my life magical. Adria Sales Ramos, which is a guy and people kept sending email to him referring as a lady :D . The most incredible human-being one can indeed know. Judit Guasch and her husband Daniel Rosenblatt, incredible friends I will always remember. And the rest of our "gang" Michael Thaller who taught me how to dance also, and Galina Khachaturyan, Hossein Riahinezhad, and Neda Aslankoohi. Mohammad Raoufi which was always like an older brother to me; and of course the rest of our group, specially Jennifer Young who helped me in reviewing my thesis.

Being one of PhD-representatives of Max Planck for Intelligent Systems gave me the chance to work together with an incredible team. It was fun organizing seminars, we organized the legendary PhD-trip together, and had so much fun on the trip together; Jim, Jan, Maryam, Katrin, and Alessio, thank you.

Last but not least, amore mio tesorino Francesco which was always there for me no matter what. I actually met him during my PhD in another department of Max Planck IS and the story of how we met could be a book itself. You are the best thing has ever happened to me, Francesco. I am finishing this PhD gladly to move on to the next chapter together with you.

Thanks to Max Planck Society for the funding, all the friends in and outside MPI; Elahe, Maral, Zolfar, Danny, Melissa, Atefeh, and many more. You made my life awesome.

22. Declaration

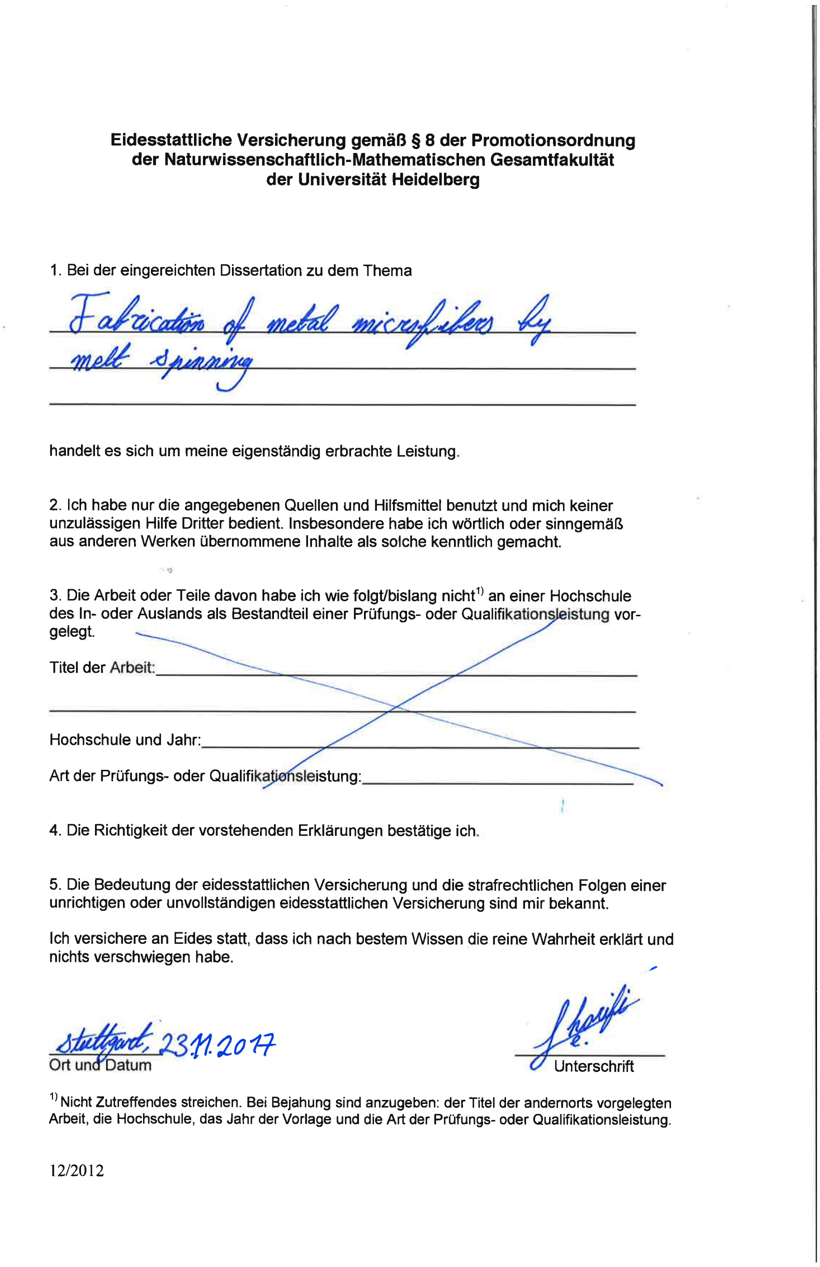

Eidesstattliche Versicherung gemäß § 8 der Promotionsordnung
der Naturwissenschaftlich-Mathematischen Gesamtfakultät
der Universität Heidelberg

1. Bei der eingereichten Dissertation zu dem Thema

Fabrication of metal microfibers by
melt spinning

handelt es sich um meine eigenständig erbrachte Leistung.

2. Ich habe nur die angegebenen Quellen und Hilfsmittel benutzt und mich keiner unzulässigen Hilfe Dritter bedient. Insbesondere habe ich wörtlich oder sinngemäß aus anderen Werken übernommene Inhalte als solche kenntlich gemacht.

3. Die Arbeit oder Teile davon habe ich wie folgt/bislang nicht[1] an einer Hochschule des In- oder Auslands als Bestandteil einer Prüfungs- oder Qualifikationsleistung vorgelegt.

~~Titel der Arbeit:~~

~~Hochschule und Jahr:~~

~~Art der Prüfungs- oder Qualifikationsleistung:~~

4. Die Richtigkeit der vorstehenden Erklärungen bestätige ich.

5. Die Bedeutung der eidesstattlichen Versicherung und die strafrechtlichen Folgen einer unrichtigen oder unvollständigen eidesstattlichen Versicherung sind mir bekannt.

Ich versichere an Eides statt, dass ich nach bestem Wissen die reine Wahrheit erklärt und nichts verschwiegen habe.

Stuttgart, 23.11.2017
Ort und Datum

Unterschrift

---

[1] Nicht Zutreffendes streichen. Bei Bejahung sind anzugeben: der Titel der andernorts vorgelegten Arbeit, die Hochschule, das Jahr der Vorlage und die Art der Prüfungs- oder Qualifikationsleistung.

12/2012

List of Figures

4.1. Estimated range of maximum section thickness of glass phase as a function of T_{rg} . . . 11
4.2. Schematic time-temperature transformation (TTT) diagram of an alloy. . . . 12
4.3. Predicted and experimentally measured critical cooling rate for glass formation plotted against reduced glass temperature for a representative range of elements and alloys. . . . 12
4.4. Schematic representation of flow defect or more commonly known as "shear transformation zone" (STZ). . . . 14
4.5. (a) Schematic of melt spinning apparatus and (b) enlarged schematic of the puddle region (not to scale). . . . 16
4.6. Cooling rate as a function of section thickness for the glass forming alloy $Fe_{40}Ni_{40}P_{14}B_6$. . . . 17

5.1. Edmund Buehler Melt-Spinner SC. . . . 19
5.2. Schematic representation of melt-spinner design and its main parts. 20
5.3. Three main slit nozzle designs used at this work. . . . 21
5.4. New vs. previous configuration of copper induction coil. . . . 22
5.5. Temperature stability over the time of melt-ejection at two induction coil configurations. . . . 22
5.6. Mechanical drawing of groove structures machined on the copper wheel. . . . 23
5.7. Image taken from melt-spinning device during fiber fabrication. . . . 24

6.1. Optical picture of casted materials on three different wheel surface structures. . . . 26
6.2. SEM picture of casted material on wheel type C. . . . 26
6.3. Schematic representation of fibers cross section. . . . 27
6.4. Different wheel surface structures for fabricating fibers. . . . 27
6.5. Surface of wheel type C after fabricating fibers. . . . 28
6.6. Optical image from fabricated fibers on flat wheel by melt-spinning. 28
6.7. SEM picture from fibers cross-sections fabricated by melt-spinning at 25μm and 200μm slit sizes. . . . 29
6.8. Relation between the slit size and the width and thickness of fibers. 30
6.9. The ratio of slit size over width of fibers at different slit sizes. . . . 30
6.10. Effect of slit size on size distribution of fibers width and thickness. . 31

6.11. Effect of slit size on cumulative counting of fibers widtha nd thickness size. . . . 32
6.12. Effect of slit size on aspect ratios of produced fibers. . . . 33
6.13. Different wheel material for melt–spinning fibers. . . . 34
6.14. Effect of wheel speed on size distribution of fibers width and thickness. 35
6.15. Effect of wheel speed of cumulative counting of fibers width and thickness. . . . 35
6.16. Effect of wheel speed on aspect ratios of produced fibers. . . . 36
6.17. Effect of applied pressure on size distribution of fibers width and thickness. . . . 37
6.18. Effect of applied pressure on cumulative counting of fibers width and thickness. . . . 38
6.19. Effect of applied pressure on aspect ratio of produced fibers. . . . 38
6.20. Effect of ejection temperature on the size distribution of fibers width and thickness. . . . 40
6.21. Effect of ejection temperature on cumulative counting of fibers width and thickness. . . . 40
6.22. Effect of ejection temperature on aspect ratio of produced fibers. . . 41
6.23. Effect of slit distance to the wheel (G) on size distribution of fibers width and thickness. . . . 42
6.24. Effect of slit distance to the wheel (G) on cumulative counting of fibers width and thickness. . . . 43
6.25. Effect of slit distance to the wheel on aspect ratio of produced fibers. 43
6.26. Effect of chamber pressure on size distribution of fibers width and thickness. . . . 44
6.27. Effect of chamber pressure on cumulative counting of fibers width and thickness. . . . 45
6.28. Effect of chamber pressure on aspect ratio of produced fibers. . . . 46
6.29. The relation between fibers width and their corresponding aspect ratio (AR=width/thickness). . . . 47
6.30. Correlation between fibers thickness and melt-spinning parameter. . 47
6.31. Sequential production of fibers by melt-spinning under same experimental conditions. . . . 48
6.32. SEM pictures of casted metals by melt-spinning. . . . 49
6.33. SEM pictures of casted intermetallic alloys by melt-spinning. . . . 50
6.34. SEM pictures of casted stainless steel alloys by melt-spinning. . . . 51
6.35. SEM pictures of casted amorphous alloys alloys by melt-spinning. . 51
6.36. SEM picture from a ribbon produced by melt-spinning partially broken to smaller width down to 1μm. . . . 52
6.37. images taken from high speed camera movies during melt ejection. . 53

7.1. Schematic drawing of applied pressures on melt inside the nozzle and slit opening . . . 62
7.2. Plausible fiber formation mechanism. . . . 66

8.1. Binary Fe-C phase diagram between 600°C and 1600°C for C content up to 7% atom[60]. . . . 70
8.2. TTT diagram for several commercial austenitic stainless steels with different molybdenum and nitrogen contents. . . . 72
8.3. Schaeffler diagram predicting the microstructure based on equivalent Cr% and Ni%. . . . 73

9.1. SS316-Ti heat treatment program . . . 75

10.1. SEM pictures from SS316-Ti micro-fibers from top and cross section view. . . . 79
10.2. Size distribution of SS316-Ti fibers (width and thickness). . . . 80
10.3. XRD from SS316-Ti before and after melt-spinning process. . . . 80
10.4. In-situ XRD of SS316-Ti at different temperatures. . . . 81
10.5. DTA pattern obtained from amorphous 316-Ti stainless steel. . . . 82
10.6. TEM bright field image from the cross section area of as-quenched SS316-Ti after melt-spinning and its diffraction pattern. . . . 82
10.7. TEM bright field image from SS316-Ti fibers after heat treatment and the difference pattern at different parts. . . . 83
10.8. Intensity profile of diffusive ring before and after heat-treatment in SS316-Ti fibers cross-section. . . . 84
10.9. Bright field TEM image, its diffraction pattern and dark field TEM images of heat-treated SS316-Ti. . . . 84
10.10TEM-bright field image from SS316-Ti light grain at higher magnification. . . . 85
10.11Hardness vs Elastic Modulus for different amorphous alloys, conventional SS316-Ti, and our amorphous and heat-treated SS316-Ti. 86
10.12Stainless steel hardness vs its grain size. . . . 86
10.13ICP-OES measurements of released ions (Fe,Ni,Cr) from as-quenched and heat-treated SS316-Ti fibers into SBF saline solution. . . . 87

14.1. Optical image of vitrovac fibers made by melt-spinning. . . . 101
14.2. SEM pictures of Vitrovac fibers at two different magnifications. . . 101
14.3. Vitrovac fibers width and thickness size distribution. . . . 102
14.4. Vitrovac fibers XRD. . . . 103
14.5. DTA pattern obtained from vitrovac fibers. . . . 103
14.6. Ultra low field SQUID measurement of vitrovac fibers. . . . 104
14.7. Comparison between the effect of fibers orientation toward external magnetic field direction. . . . 105

14.8. a) In-sit XRD of vitrovac fibers at different temperatures and their corresponding hysteresis measurements. 105
14.9. ICP-OES measurements of released ions (Co,Fe,Mo,Si) from as-quenched and heat-treated vitrovac fibers into BSF saline solution. . 106

20.1. XRD from different stainless steel fibers fabricated by melt-spinning. 123
20.2. XRD results of as-quenched SS316-Ti fibers after melt-spinning. . . 124

List of Tables

5.1. Standard melt-spinning experimental parameters 24

9.1. SS316-Ti fabrication experimental parameters 76

11.1. Experimentally obtained values for SS316-Ti fibers 90

13.1. Vitrovac fabrication experimental parameters 99

20.1. Melt-Spinning experiments and their parameters. 117
20.2. Stainless steel alloys atomic composition (atomic%) 122
20.3. Nanoindentation measurements of Elastic modulus and hardness for fabricated fibers 124
20.4. Elastic Modulus and Hardness values of different amorphous alloys used in Figure 10.11 125

Bibliography

[1] F.E. Luborsky, P.G. Frischmann, and L.A. Johnson. The role of amorphous materials in the magnetics industry. *Journal of Magnetism and Magnetic Materials*, 8(4):318 – 329, 1978.

[2] G.S. Cargill. Structure of metallic alloy glasses. volume 30 of *Solid State Physics*, pages 227 – 320. Academic Press, 1975.

[3] J.H. Perepezko and G. Wilde. Melt undercooling and nucleation kinetics. *Current Opinion in Solid State and Materials Science*, 20(1):3 – 12, 2016. Recent Advances in Solidification Microstructure- Experiments and Computational Analysis.

[4] Jitendra Gaur and R.K. Mishra. Estimation of thermodynamic parameters for au- and mg-based metallic glasses. *Chemical Physics Letters*, 685(Supplement C):244 – 250, 2017.

[5] D. Turnbull and M. H. Cohen. Free-volume model of the amorphous phase: Glass transition. *The Journal of Chemical Physics*, 34:120–125, jan 1961.

[6] Charles C. Hays and William L. Johnson. Undercooling of bulk metallic glasses processed by electrostatic levitation. *Journal of Non-Crystalline Solids*, 250-252(Part 2):596 – 600, 1999.

[7] S. Pogatscher, D. Leutenegger, A. Hagmann, P.J. Uggowitzer, and J.F. Loeffler. Reprint of: Characterization of bulk metallic glasses via fast differential scanning calorimetry. *Thermochimica Acta*, 603:46 – 52, 2015. Chip Calorimetry.

[8] R C Jones and G J Yates. Spin waves in a ferromagnet with randomly disordered bonds. *Journal of Physics C: Solid State Physics*, 8(11):1705.

[9] Satoru Fujime. Electron diffraction at low temperature v. on amorphous films of transition metals and alloys prepared by low temperature condensation. *Japanese Journal of Applied Physics*, 6(3):305, 1967.

[10] Peiyou LI, Fanying MENG, Yongshan WANG, Minmin DONG, Junting SHI, and Peiwei SONG. Glass forming ability and thermodynamic properties in novel la-al-cu-co bulk metallic glasses. *Journal of Rare Earths*, 33(9):972 – 976, 2015.

[11] Ping Zhang, Hongqing Wei, Xiaolin Wei, Zhilin Long, and Xuping Su. Evaluation of glass-forming ability for bulk metallic glasses based on characteristic temperatures. *Journal of Non-Crystalline Solids*, 355(43):2183 – 2189, 2009.

[12] Z.P. Lu and C.T. Liu. A new glass-forming ability criterion for bulk metallic glasses. *Acta Materialia*, 50(13):3501 – 3512, 2002.

[13] D. Turnbull. Under what conditions can a glass be formed? *Contemporary Physics*, 10:473, sep 1969.

[14] H.A. Davies and B.G. Lewis. A generalised kinetic approach to metallic glass formation. *Scripta Metallurgica*, 9(10):1107 – 1112, 1975.

[15] H.A. Davies. Chapter 2 - metallic glass formation. In F.E. LUBORSKY, editor, *Amorphous Metallic Alloys*, pages 8 – 25. Butterworth-Heinemann, 1983.

[16] H.A. Davies and J.B. Hull. Amorphous nickel produced by splat quenching. *Materials Science and Engineering*, 23(2):193 – 198, 1976. The Second International Conference on Rapidly Quenched Metals.

[17] W.H. Wang, C. Dong, and C.H. Shek. Bulk metallic glasses. *Materials Science and Engineering: R: Reports*, 44(2):45 – 89, 2004.

[18] Ying-Kun Xu, Han Ma, Jian Xu, and En Ma. Mg-based bulk metallic glass composites with plasticity and gigapascal strength. *Acta Materialia*, 53(6):1857 – 1866, 2005.

[19] Li Zhang, Yong-Qiang Cheng, A-Jing Cao, Jian Xu, and Evan Ma. Bulk metallic glasses with large plasticity: Composition design from the structural perspective. *Acta Materialia*, 57(4):1154 – 1164, 2009.

[20] S.J Pang, T Zhang, K Asami, and A Inoue. Synthesis of fe-cr-mo-c-b-p bulk metallic glasses with high corrosion resistance. *Acta Materialia*, 50(3):489 – 497, 2002.

[21] M.F. Ashby and A.L. Greer. Metallic glasses as structural materials. *Scripta Materialia*, 54(3):321 – 326, 2006. Viewpoint set no: 37. On mechanical behavior of metallic glasses.

[22] A.S. Argon and H.Y. Kuo. Plastic flow in a disordered bubble raft (an analog of a metallic glass). *Materials Science and Engineering*, 39(1):101 – 109, 1979.

[23] Eric R. Homer and Christopher A. Schuh. Mesoscale modeling of amorphous metals by shear transformation zone dynamics. *Acta Materialia*, 57(9):2823 – 2833, 2009.

[24] D. Srolovitz, V. Vitek, and T. Egami. An atomistic study of deformation of amorphous metals. *Acta Metallurgica*, 31(2):335 – 352, 1983.

[25] Mareike Zink, K. Samwer, W. L. Johnson, and S. G. Mayr. Plastic deformation of metallic glasses: Size of shear transformation zones from molecular dynamics simulations. *Phys. Rev. B*, 73:172203, May 2006.

[26] Christopher A. Schuh, Todd C. Hufnagel, and Upadrasta Ramamurty. Mechanical behavior of amorphous alloys. *Acta Materialia*, 55(12):4067 – 4109, 2007.

[27] D.E Polk and D Turnbull. Flow of melt and glass forms of metallic alloys. *Acta Metallurgica*, 20(4):493 – 498, 1972.

[28] Yongwei Wang, Mo Li, and Jinwu Xu. Free volume gradient effect on mechanical properties of metallic glasses. *Scripta Materialia*, 130(Supplement C):12 – 16, 2017.

[29] Marc Blétry, Minh Thanh Thai, Yannick Champion, and Lo˙ Consistency of the free-volume approach to the homogeneous deformation of metallic glasses. *Comptes Rendus Mécanique*, 342(5):311 – 314, 2014. Frontiers of micro and nanomechanics of materials: Soft or amorphous matter, surface effects.

[30] F.G. Shi, T.G. Nieh, and Y.T. Chou. A free volume approach for self-diffusion in metals. *Scripta Materialia*, 43(3):265 – 267, 2000.

[31] Frans Spaepen. A microscopic mechanism for steady state inhomogeneous flow in metallic glasses. *Acta Metallurgica*, 25(4):407 – 415, 1977.

[32] A.S Argon. Plastic deformation in metallic glasses. *Acta Metallurgica*, 27(1):47 – 58, 1979.

[33] A. L. Greer and E. Ma. Bulk metallic glasses: At the cutting edge of metals research. *MRS Bulletin*, 32(8):611–619, 2007.

[34] Wei Hua Wang. The elastic properties, elastic models and elastic perspectives of metallic glasses. *Progress in Materials Science*, 57(3):487 – 656, 2012.

[35] Morgana Martin Trexler and Naresh N. Thadhani. Mechanical properties of bulk metallic glasses. *Progress in Materials Science*, 55(8):759 – 839, 2010.

[36] M. Chen. Mechanical behavior of metallic glasses: Microscopic understanding of strength and ductility. *Annual Review of Materials Science*, 38:445–469, aug 2008.

[37] J. Lu, G. Ravichandran, and W.L. Johnson. Deformation behavior of the zr41.2ti13.8cu12.5ni10be22.5 bulk metallic glass over a wide range of strain-rates and temperatures. *Acta Materialia*, 51(12):3429 – 3443, 2003.

[38] Jinwoo Kim, Hyun Seok Oh, Wan Kim, Pyuck-Pa Choi, Dierk Raabe, and Eun Soo Park. Modulation of plastic flow in metallic glasses via nanoscale networks of chemical heterogeneities. *Acta Materialia*, 140(Supplement C):116 – 129, 2017.

[39] C. Liu, V. Roddatis, P. Kenesei, and R. Maass. Shear-band thickness and shear-band cavities in a zr-based metallic glass. *Acta Materialia*, 140(Supplement C):206 – 216, 2017.

[40] M. Pagnola, M. Malmoria, and M. Barone. Biot number behaviour in the chill block melt spinning (cbms) process. *Applied Thermal Engineering*, 103:807 – 811, 2016.

[41] Kosuke Nagashio and Kazuhiko Kuribayashi. Experimental verification of ribbon formation process in chill-block melt spinning. *Acta Materialia*, 54(9):2353 – 2360, 2006.

[42] H.H. Liebermann. Rapidly solidified alloys made by chill block melt-spinning processes. *Journal of Crystal Growth*, 70(1):497 – 506, 1984.

[43] M. Falkowski, V. Buturlim, M. Paukov, and L. Havela. Thermal transport and thermopower of bcc u-mo splat-cooled alloys. *Physica B: Condensed Matter*, 2017.

[44] L. Li, X.Y. Wang, G. Wei, A. Vaidya, H. Zhang, and S. Sampath. Substrate melting during thermal spray splat quenching. *Thin Solid Films*, 468(1):113 – 119, 2004.

[45] M. Sowjanya and T. Kishen Kumar Reddy. Obtaining stable puddle and thinner ribbons during planar flow melt spinning process. *Materials Today: Proceedings*, 4(2, Part A):890 – 897, 2017. 5th International Conference of Materials Processing and Characterization (ICMPC 2016).

[46] M. Sowjanya and T. Kishen Kumar Reddy. Flow dynamics in the melt puddle during planar flow melt spinning process. *Materials Today: Proceedings*, 4(2, Part A):3728 – 3735, 2017. 5th International Conference of Materials Processing and Characterization (ICMPC 2016).

[47] B.L. Cox and P.H. Steen. Herringbone defect formation in planar-flow melt spinning. *Journal of Materials Processing Technology*, 213(10):1743 – 1752, 2013.

[48] J.K. Carpenter and P.H. Steen. Heat transfer and solidification in planar-flow melt-spinning: high wheelspeeds. *International Journal of Heat and Mass Transfer*, 40(9):1993 – 2007, 1997.

[49] Ryu Seino and Yuichi Sato. Observation of melt puddle behavior in planar flow casting in air. *Journal of Alloys and Compounds*, 586(Supplement 1):S150 – S152, 2014. SI : ISMANAM 2012.

[50] A.B. Bichi, W.R. Smith, and J.G. Wissink. Solidification and downstream meniscus prediction in the planar-flow spin casting process. *Chemical Engineering Science*, 63(3):685 – 695, 2008.

[51] Cormac J. Byrne, Steven J. Weinstein, and Paul H. Steen. Capillary stability limits for liquid metal in melt spinning. *Chemical Engineering Science*, 61(24):8004 – 8009, 2006.

[52] Paul H. Steen and Christian Karcher. Fluid mechanics of spin casting of metals. *Annual Review of Fluid Mechanics*, 29(1):373–397, 1997.

[53] Yu-Guang Su, Falin Chen, Chung-Yung Wu, and Min-Hsing Chang. Effect of surface roughness of chill wheel on ribbon formation in the planar flow casting process. *Journal of Materials Processing Technology*, 229(Supplement C):609 – 613, 2016.

[54] Cormac J. Byrne, Aaron M. Kueck, Shefford P. Baker, and Paul H. Steen. In situ manipulation of cooling rates during planar-flow melt spinning processing. *Materials Science and Engineering: A*, 459(1):172 – 181, 2007.

[55] K. Russew and L. Stojanova. *Glassy Metals*. Springer Berlin Heidelberg, 2016.

[56] Victor I Tkatch, Alexander I Limanovskii, Sergey N Denisenko, and Sergey G Rassolov. The effect of the melt-spinning processing parameters on the rate of cooling. *Materials Science Engineering A*, 323(1-2):91–96, jan 2002.

[57] Copyright. In F.E. LUBORSKY, editor, *Amorphous Metallic Alloys*, pages iv –. Butterworth-Heinemann, 1983.

[58] M Sowjanya and T Kishen Kumar Reddy. Cooling wheel features and amorphous ribbon formation during planar flow melt spinning process. *Journal of Materials Processing Tech.*, 214(9):1861–1870, sep 2014.

[59] Chunbai Wang and Ambar K Mitra. Numerical and analytical modeling of free-jet melt spinning for fe 75-si 10-b 15(at. %) metallic glasses. *Journal of Heat Transfer*, 136(7):072101–11, jul 2014.

[60] Binary system c-fe: Datasheet from landolt-boernstein - group iv physical chemistry volume 19c1: Ternary steel systems: Phase diagrams and phase transition data in springermaterials. Copyright 2012 Springer-Verlag Berlin Heidelberg.

[61] H. Okamoto. The c-fe (carbon-iron) system. *Journal of Phase Equilibria*, 13(5):543–565, Oct 1992.

[62] Bradley D. Fahlman. *Metals*, pages 157–237. Springer Netherlands, Dordrecht, 2011.

[63] Takehisa Yamada, Yoichi Yamashita, and Sohei Kanna. A study on evaluation of ductile crack initiation using strain hardening exponent for steels. *Procedia Structural Integrity*, 2(Supplement C):2206 – 2213, 2016. 21st European Conference on Fracture, ECF21, 20-24 June 2016, Catania, Italy.

[64] R. Sri Rama devi, G. Poshal, K. Eshwara prasad, and R. Raman Goud. Strain hardening behaviour of hot rolled annealed nickel free nitrogen based austenitic stainess steel. *Materials Today: Proceedings*, 4(2, Part A):917 – 926, 2017. 5th International Conference of Materials Processing and Characterization (ICMPC 2016).

[65] Yoji Mine, Nobuaki Horita, Zenji Horita, and Kazuki Takashima. Effect of ultrafine grain refinement on hydrogen embrittlement of metastable austenitic stainless steel. *International Journal of Hydrogen Energy*, 42(22):15415 – 15425, 2017.

[66] Changsheng Li, Biao Ma, Yanlei Song, Jianjun Zheng, and Jikai Wang. Grain refinement of non-magnetic austenitic steels during asymmetrical hot rolling process. *Journal of Materials Science & Technology*, 2017.

[67] Huihui Yu, Yunchang Xin, Maoyin Wang, and Qing Liu. Hall-petch relationship in mg alloys: A review. *Journal of Materials Science & Technology*, 2017.

[68] E O Hall. The deformation and ageing of mild steel: Ii characteristics of the lueders deformation. *Proceedings of the Physical Society. Section B*, 64(9):742, 1951.

[69] Wenwu Xu and Lilian P. DÃ¡vila. Tensile nanomechanics and the hall-petch effect in nanocrystalline aluminium. *Materials Science and Engineering: A*, 2017.

[70] T.G. Nieh and J. Wadsworth. Hall-petch relation in nanocrystalline solids. *Scripta Metallurgica et Materialia*, 25(4):955 – 958, 1991.

[71] J. Eckert, J.C. Holzer, C.E. Krill, and W.L. Johnson. Structural and thermodynamic properties of nanocrystalline fcc metals prepared by mechanical attrition. *Journal of Materials Research*, 7(7):1751–1761, 1992.

[72] A.H. Chokshi, A. Rosen, J. Karch, and H. Gleiter. On the validity of the hall-petch relationship in nanocrystalline materials. *Scripta Metallurgica*, 23(10):1679 – 1683, 1989.

[73] Z.B. Qi, P. Sun, F.P. Zhu, Z.C. Wang, D.L. Peng, and C.H. Wu. The inverse hall-petch effect in nanocrystalline zrn coatings. *Surface and Coatings Technology*, 205(12):3692 – 3697, 2011.

[74] K.A. Padmanabhan, Sriharsha Sripathi, H. Hahn, and H. Gleiter. Inverse hall-petch effect in quasi- and nanocrystalline materials. *Materials Letters*, 133(Supplement C):151 – 154, 2014.

[75] M.J. Yao, E. Welsch, D. Ponge, S.M.H. Haghighat, and S. Sandl˙Strengthening and strain hardening mechanisms in a precipitation-hardened high-mn lightweight steel. *Acta Materialia*, 140(Supplement C):258 – 273, 2017.

[76] A. J. Ardell. Precipitation hardening. *Metallurgical Transactions A*, 16(12):2131–2165, Dec 1985.

[77] Anish Karmakar, Subrata Mukherjee, Saurabh Kundu, Dinesh Srivastava, Rahul Mitra, and Debalay Chakrabarti. Effect of composition and isothermal holding temperature on the precipitation hardening in vanadium-microalloyed steels. *Materials Characterization*, 132(Supplement C):31 – 40, 2017.

[78] Pedro Henrique Lamar ao Souza, Carlos Augusto Silva de Oliveira, and José Maria do Vale Quaresma. Precipitation hardening in dilute al-zr alloys. *Journal of Materials Research and Technology*, 2017.

[79] Curtis W. Kavosh. high-performance stainless steel.

[80] R.K. Gupta and N. Birbilis. The influence of nanocrystalline structure and processing route on corrosion of stainless steel: A review. *Corrosion Science*, 92(Supplement C):1 – 15, 2015.

[81] K.H. Lo, C.H. Shek, and J.K.L. Lai. Recent developments in stainless steels. *Materials Science and Engineering: R: Reports*, 65(4):39 – 104, 2009.

[82] R.O.Adams. A review of the stainless steel surface. *Journal of Vacuum Science & Technology A: Vacuum, Surfaces, and Films*, 1(1):12–18, 1983.

[83] Yinghui Zhou, Yongchang Liu, Xiaosheng Zhou, Chenxi Liu, Jianxin Yu, Yuan Huang, Huijun Li, and Wenya Li. Precipitation and hot deformation behavior of austenitic heat-resistant steels: A review. *Journal of Materials Science & Technology*, 2017.

[84] M. Nekouie Esfahani, J. Coupland, and S. Marimuthu. Microstructure and mechanical properties of a laser welded low carbon–stainless steel joint. *Journal of Materials Processing Technology*, 214(12):2941 – 2948, 2014.

[85] Qiang Wang, Song Zhang, ChunHua Zhang, Chenliang Wu, Jianqiang Wang, Jiang Chen, and Zulai Sun. Microstructure evolution and ebsd analysis of a graded steel fabricated by laser additive manufacturing. *Vacuum*, 141(Supplement C):68 – 81, 2017.

[86] M F McGuire. *Stainless Steels for Design Engineers*. ASM International, 2008.

[87] Dong Ye, Jun Li, Wen Jiang, Jie Su, and Kunyu Zhao. Effect of cu addition on microstructure and mechanical properties of 15%cr super martensitic stainless steel. *Materials & Design*, 41(Supplement C):16 – 22, 2012.

[88] B. Ravi Kumar, Sailaja Sharma, and B. Mahato. Formation of ultrafine grained microstructure in the austenitic stainless steel and its impact on tensile properties. *Materials Science and Engineering: A*, 528(6):2209 – 2216, 2011.

[89] Hua bing LI, Zhou hua JIANG, Zu rui ZHANG, and Yan YANG. Effect of grain size on mechanical properties of nickel-free high nitrogen austenitic stainless steel. *Journal of Iron and Steel Research, International*, 16(1):58 – 61, 2009.

[90] Y.M. Wang and E. Ma. Strain hardening, strain rate sensitivity, and ductility of nanostructured metals. *Materials Science and Engineering: A*, 375-377(Supplement C):46 – 52, 2004.

[91] D. Jia, Y. M. Wang, K. T. Ramesh, E. Ma, Y. T. Zhu, and R. Z. Valiev. Deformation behavior and plastic instabilities of ultrafine-grained titanium. *Applied Physics Letters*, 79(5):611–613, 2001.

[92] Yunqing Ma, Jae-Eun Jin, and Young-Kook Lee. A repetitive thermomechanical process to produce nano-crystalline in a metastable austenitic steel. *Scripta Materialia*, 52(12):1311 – 1315, 2005.

[93] C. X. Huang, W. P. Hu, Q. Y. Wang, C. Wang, G. Yang, and Y. T. Zhu. An ideal ultrafine-grained structure for high strength and high ductility. *Materials Research Letters*, 3(2):88–94, 2015.

[94] DY Li. Electron work function at grain boundary and the corrosion behavior of nanocrystalline metallic materials. In *Materials Research Society Symposium Proceedings*, volume 887, page 227. Warrendale, Pa.; Materials Research Society; 1999, 2006.

[95] R.M. Davison, T.R. Laurin, J.D. Redmond, H. Watanabe, and M. Semchyshen. A review of worldwide developments in stainless steels. *Materials & Design*, 7(3):111 – 119, 1986.

[96] Dae-Bum Park, Moo-Young Huh, Woo-Sang Jung, Jin-Yoo Suh, Jae-Hyeok Shim, and Seung-Cheol Lee. Effect of vanadium addition on the creep resistance of 18cr9ni3cunbn austenitic stainless heat resistant steel. *Journal of Alloys and Compounds*, 574(Supplement C):532 – 538, 2013.

[97] Shuping Tan, Zhenhua Wang, Shichang Cheng, Zhengdong Liu, Jiecai Han, and Wantang Fu. Processing maps and hot workability of super304h austenitic heat-resistant stainless steel. *Materials Science and Engineering: A*, 517(1):312 – 315, 2009.

[98] Joonoh Moon, Tae-Ho Lee, Jong-Ho Shin, and Jong-Wook Lee. Hot working behavior of a nitrogen-alloyed fe-18mn-18cr-n austenitic stainless steel. *Materials Science and Engineering: A*, 594(Supplement C):302 – 308, 2014.

[99] P. Marshall. *Microstructure and mechanical properties*. Springer Netherlands, 1984.

[100] T. Michler. Austenitic stainless steels. In *Reference Module in Materials Science and Materials Engineering*, pages –. Elsevier, 2016. Current as of 20 September 2016.

[101] F.K. Yan, B.B. Zhang, H.T. Wang, N.R. Tao, and K. Lu. Nanoindentation characterization of nano-twinned grains in an austenitic stainless steel. *Scripta Materialia*, 112(Supplement C):19 – 22, 2016.

[102] D Zois, A Lekatou, M Vardavoulias, T Vaimakis, and A E Karantzalis. Partially amorphous stainless steel coatings: Microstructure, annealing behavior and statistical optimization of spray parameters. *Surface and Coatings Technology*, 206(6):1469–1483, dec 2011.

[103] D M Follstaedt, F G Yost, L E Pope, S T Picraux, and J A Knapp. The amorphous phase and surface mechanical properties of 304 stainless steel implanted with ti and c. *Applied Physics Letters*, 43(4):358–360, aug 1983.

[104] John J. Gilman. Mechanical behavior of metallic glasses. *Journal of Applied Physics*, 46(4):1625–1633, 1975.

[105] G Knuyt, L De Schepper, and L M Stals. Calculation of elastic constants for an amorphous metal and the influence of relaxation. *Journal of Physics F: Metal Physics*, 16(12):1989, 1986.

[106] D Weaire, M.F Ashby, J Logan, and M.J Weins. On the use of pair potentials to calculate the properties of amorphous metals. *Acta Metallurgica*, 19(8):779 – 788, 1971.

[107] T A Stolarski. A probabilistic approach to wear prediction. *Journal of Physics D: Applied Physics*, 23(9):1143, 1990.

[108] Vitrovac magnetic properties.

[109] G AGUILARSAHAGUN, P QUINTANA, E AMANO, JTS IRVINE, R VALENZUELA, and John Thomas Sirr Irvine. Equation-of-motion of domain-walls and equivalent-circuits in soft ferromagnetic materials. *Journal of Applied Physics*, 75(10):7000–7002, 5 1994.

[110] I. Betancourt, M. Jimènez, S. Aburto, V. Marquina, R. Gómez, M.L. Marquina, R. Ridaura, M. Miki, and R. Valenzuela. Nanocrystallization studies in co-rich amorphous alloys. *Journal of Magnetism and Magnetic Materials*, 140-144(Part 1):459 – 460, 1995. International Conference on Magnetism.

[111] G Bordin, G Buttino, A Cecchetti, and M Poppi. Nanocrystallization of ferromagnetic co-rich amorphous alloys and magnetic softening. *Journal of Physics D: Applied Physics*, 30(15):2163, 1997.

[112] G. Buttino, A. Cecchetti, and M. Poppi. Magnetic softening and nanocrystallization in amorphous co-rich alloys. *Journal of Magnetism and Magnetic Materials*, 172(1):147 – 152, 1997.

[113] J. Świerczek, H. Lampa, Z. Nitkiewicz, and Z. Bałaga. Microstructure and some magnetic properties of annealed vitrovac 6025x amorphous ribbons. *Materials Science and Engineering: A*, 356(1):108 – 113, 2003.

[114] Hongwen Zhang, Ghatu Subhash, Laszlo J. Kecskes, and Robert J. Dowding. Mechanical behavior of bulk (zrhf)ticunial amorphous alloys. *Scripta Materialia*, 49(5):447 – 452, 2003.

[115] Hao Li, Ghatu Subhash, Xin-Lin Gao, Laszlo J. Kecskes, and Robert J. Dowding. Negative strain rate sensitivity and compositional dependence of fracture strength in zr/hf based bulk metallic glasses. *Scripta Materialia*, 49(11):1087 – 1092, 2003.

[116] H. W. Zhang, G. Subhash, X. N. Jing, L. J. Kecskes, and R. J. Dowding.

[117] Akihisa Inoue, Shintaro Sobu, Dmitri V. Louzguine, Hisamichi Kimura, and Kenichiro Sasamori. Ultrahigh strength al-based amorphous alloys containing sc. *Journal of Materials Research*, 19(5):1539–1543, 2004.

[118] Akihisa Inoue, Wei Zhang, Tao Zhang, and Kei Kurosaka. Formation and mechanical properties of cu–hf–ti bulk glassy alloys [article retracted]. *Journal of Materials Research*, 16(10):2836–2844, 2001.

[119] A. Inoue, B.L. Shen, and C.T. Chang. Super-high strength of over 4000 mpa for fe-based bulk glassy alloys in [(fe(1-x)cox)0.75b0.2si0.05]96nb4 system. *Acta Materialia*, 52(14):4093 – 4099, 2004.

[120] Donghua Xu, Gang Duan, William L Johnson, and Carol Garland. Formation and properties of new ni-based amorphous alloys with critical casting thickness up to 5 mm. *Acta Materialia*, 52(12):3493 – 3497, 2004.

[121] R.D. Conner, R.B. Dandliker, and W.L. Johnson. Mechanical properties of tungsten and steel fiber reinforced zr41.25ti13.75cu12.5ni10be22.5 metallic glass matrix composites. *Acta Materialia*, 46(17):6089 – 6102, 1998.

[122] P.E. Donovan and W.M. Stobbs. The structure of shear bands in metallic glasses. *Acta Metallurgica*, 29(8):1419 – 1436, 1981.